U.PORTO

MESTRADO
MEDICINE AND MOLECULAR ONCOLOGY

Three-Dimensional Triple Negative Breast Cancer Models: A Platform for Radiobiology Studies

Bárbara Nunes

M

2026

FACULDADE DE **MEDICINA**

Bárbara Nunes
Master Student in Medicine and Molecular Oncology
Supervisor: Doutora Flávia Castro, TMI, i3S
Co-Supervisors: Doutora Maria José Oliveira & Doutora Joana Carvalho, TMI, i3S

FINANCIAL SUPPORT

This work was financially supported by FEDER - Fundo Europeu de Desenvolvimento Regional funds through the COMPETE 2020 - Operacional Programme for Competitiveness and Internationalization (POCI), Portugal 2020, by Portuguese funds through FCT - Fundação para a Ciência e a Tecnologia in the framework of the project POCI-01-0145-FEDER-016390. This work was also partially supported by Programa Operacional Regional do Norte and co-funded by the European Regional Development Fund under the project "The Porto Comprehensive Cancer Center" with the reference NORTE-01-0145-FEDER-072678 - Consórcio Porto. Comprehensive Cancer Center Raquel Seruca, by RESISTANCE: dissect the role of immune cells on rectal cancer radioresistance",with the reference COMPETE2030-FEDER-00707100, Operation No. 15942, funded by COMPETE2030 and national funds (FCT) under Notice no. MPr-2023-12 and by the BEACON Flagship projects supported by INEB- National Institute of Bioengineering and by Ipatimup- Institute of Pathology and Immunology of the University of Porto. This work was supported by the Portuguese Science and Technology Foundation (FCT), in the framework of the project "RADIORESISTANCE-Dissect the tumor microenvironment to battle cancer radioresistance and immune escape" (PTDC/MED-ONC/4165/2021), by operation nº15852 - COMPETE2030-FEDER-00696500 supported by Innovation and Digital Transition Program (PITD), Portugal 2030 and European Union, by Programa Gilead GENESE 2023 in the framework of the project "E- MAGIC: ExosoMes-derived rAdioresistance siGnature In breast Cancer" and by Programa PESSOA Cooperação Bilateral Portugal-França (2023.09861.CBM).



SCIENTIFIC OUTPUTS

Publications

Original research articles in peer-reviewed journals:

Canha-Borges A*, **Nunes B***, Estêvão D, Fernandes R, Mondini M, Cruz T, Jerónimo C, Lencart J, Paredes J, Deutsch E, Oliveira MJ, Castro F – "Radiotherapy induces layer-specific molecular and ultrastructural alterations in triple-negative breast cancer spheroids" Radiotherapy and Oncology 2026, DOI: 10.1016/j.radonc.2026.111518. *, equally contributing first authors

Review article in peer-reviewed journals:

Canha-Borges A, **Nunes B**, Quintas S, Paredes J, Meziani L, Mondini M, Oliveira MJ, Deutsch E, Castro F, "Emerging mechanisms of triple-negative breast cancer radioresistance: Interplay between cancer cell mechanisms and the tumor immune microenvironment" Cancer Treatment Reviews 2025. DOI: 10.1016/j.ctrv.2025.103026

Other publications that are not part of this Master thesis, but were co-authored during the time of its development:

Original research articles in peer-reviewed journals:

Canha-Borges A; **Nunes B**, Silva M, Cardoso AP, Costa B; Matos M; Fontes M; Lencart J; Coutinho R; Silva E; Nascimento D; Estêvão D; Jerónimo C; Paredes J; Mondini M; Deutsch E; Fior R; Castro F; Oliveira MJ. "Establishing a comprehensive preclinical platform to study radioresistance in triple-negative breast cancer", under major revisions at Frontiers in Immunology

Canha-Borges A, Ferreira MM, **Nunes B**, Leal F; Sousa BM; Naulin F; Liu W Estêvão D, Jerónimo C, Lencart J, Paredes J, Mondini M, Castro F, Deutsch E, Oliveira MJ. "Macrophages mediate cancer cells survival mechanisms after radiotherapy in triple negative breast cancer" (Manuscript in preparation)

Review articles in peer-reviewed journals:

Ferreira MM, Nunes B, Canha-Borges A, Sousa BM, Oliveira MJ, Castro F "Scaffold based 3D *in vitro* models as promising models for radiobiology studies" (Manuscript in preparation)

Congresses

Nacional

I3S Annual Meeting

- Participation and presentation of a Speed Talk on “Unravelling Radioresistance in Triple-Negative Breast Cancer Spheroids”, November 2024

- Participation and presentation of a Speed Talk on “Unraveling Layer-Specific Response to Radiotherapy in Triple Negative Breast Cancer Spheroids”, November 2025

IJUP

- Participation and oral presentation on the topic “Advanced 3D Models for Breast Cancer: A New Frontier in Radiobiology Research”**,** May 2025

- Participation and oral presentation on the topic “Unravelling Layer-Specific Response to Radiotherapy in Triple Negative Breast Cancer Spheroids”, May 2026

Symposium on Immunomodulation in Cancer & Regeneration

- Participation and poster presentation at the 6th Symposium on Immunomodulation in Cancer & Regeneration on the topic “Unravelling Layer-Specific Response to Radiotherapy in Triple Negative Breast Cancer Spheroids”, June 2026

International

EUGLOH (European University Alliance for Global Health)

- Participation and poster presentation at EUGLOH 6th Annual Student Research Conference on the topic “Revolutionizing Radiobiology: 3D Models for Breast Cancer Research”, November 2025

ASEICA-ASPIC

- Participation and poster presentation at the IV ASEICA-ASPIC International Meeting on the topic “Unveiling Layer-Specific Response to Radiotherapy in Breast Tumor Spheroids”, November 2025

ASPIC

- Participation and poster presentation at the 7th ASPIC – International Congress on the topic “Unveiling Layer-Specific Response to Radiotherapy in Breast Tumor Spheroids”, June 2026

Competitions

iMED – Innovate Competition

Participation and poster presentation at iMED Innovation competition on the topic “Advanced 3D Models for Breast Cancer: A New Frontier in Radiobiology Research”, highlighting the work I carried out during my first year within the TMI group, October 2025

Awards

Best oral presentation award by IJUP (Young research at the University of Porto) on the topic “Advanced 3D Models for Breast Cancer: A New Frontier in Radiobiology Research”, May 2025

Best Poster presentation award by EUGLOH on the topic “Revolutionizing Radiobiology: 3D Models for Breast Cancer Research”, Granted a travel grant for the next Annual Student Research Conference 2026 in Hamburg, November 2025

Courses

Radioncology Professional Course by LPCC (Liga Portuguesa Contra o Cancro), 21 hours, March 2025

10th Annual International Course on Immunotherapy by International School of Immunotherapy, March 2025

Table of contents

FIGURE AND TABLE INDEX 13

ABBREVIATIONS 17

ACKNOWLEDGEMENTS 21

ABSTRACT 27

RESUMO 31

1. INTRODUCTION 35

1.1 Breast cancer as the leading cause of cancer in women: the global impact and risk factors **36**

1.1.1 Epidemiology 36

1.1.2 Demographic influence 37

1.1.3 Risk factors 37

1.2 Understanding breast cancer screening and treatment approaches **38**

1.2.1 Screening and diagnosis 38

1.2.2 Breast cancer classification 40

1.3 Triple negative breast cancer: the global burden **42**

1.3.1 Epidemiology 42

1.3.2 TNBC subtypes 42

1.3.3 Treatments 43

1.4 Understanding radiotherapy in TNBC: mechanisms and clinical implications **44**

1.4.1 Molecular mechanisms underlying irradiation 44

1.4.2 RT clinical history 45

1.4.3 Radioresistance in TNBC 45

1.5 Extracellular vesicles in radioresistance: emerging players **47**

1.5.1 EVs composition and structure 47

1.5.2 EVs and TNBC interplay 47

1.6 3D models in radiobiology: insights and roles **48**

1.6.1 Benefits and structure of 3D models 49
1.6.2 Relevance of 3D models in radiobiology 49

2. AIM OF THE PROJECT 51

3. METHODS AND MATERIALS 53

3.1 Cell culture 54

3.2 Development of radioresistant cell lines 54

3.3 Clonogenic assay 54

3.4 Proliferation assay 54

3.5 2D *in vitro* seeding and irradiation 55

3.6 Tumor spheroids formation 55

3.7 Tumor spheroid and 2D *in vitro* morphological characterization 56

3.8 Tumor spheroids irradiation 56

3.9 Tumor spheroids metabolic activity 56

3.10 Histological analysis 57

3.11 Transmission electron microscopy (TEM) 57

3.12 Flow cytometry 58

3.13 Reactive oxidative species (ROS) analysis 58

3.14 EVs-depleted Media and EVs isolation 58

3.15 Western Blot 60

3.16 Proteomic analysis 61

3.17 Statistical analysis 63

4. RESULTS 65

4.1 Establishment and characterization of human and mouse syngeneic radioresistant TNBC models 66

4.1.1 – Radioresistant cell lines show significant morphological and phenotypical changes 67

4.1.2 – Establishment of 4T1 Tumor spheroids for radiobiology studies 71

4.1.3 – Irradiation elicits distinct morphological and phenotypic responses in 2D versus 3D tumor models 73

4.1.4 – Irradiation differently impacts cell cycle and ROS production in 3D models 82

4.2 Model Transition induces significant phenotypical and molecular changes in TNBC cells 86

4.3 Establishment and Characterization of 3D Tumor Spheroids after Irradiation 89

4.3.1 – Radiosensitive MDA-MB-231 Spheroids suffer significant molecular and phenotypical changes after a clinical relevant radiotherapy scheme 90

4.3.2 - Hypofractionated radiotherapy increases 3D breast cancer spheroids mitochondrial content 94

4.3.3 - Hypofractionated radiotherapy increases lipid droplets accumulation in the periphery of 3D breast cancer spheroids 96

4.3.4 - Hypofractionated radiotherapy increases rough endoplasmic reticulum and autophagic vesicles content in 3D breast cancer spheroids 98

4.4 Unveiling the Proteomic Landscape of TNBC Spheroids-Derived Extracellular Vesicles 100

4.4.1 – Extracellular vesicles isolation techniques: ultracentrifugation, size exclusion chromatography and ultrafiltration 102

4.4.2 – Radiotherapy significantly increases extracellular vesicle secretion and particle size in MDA-MB-231 breast tumor spheroids 104

4.4.3 – Extracellular vesicles proteomic profile is significantly altered after irradiation 107

5. DISCUSSION 109

5.1 Unveiling the RR signature of TNBC through 3D models 110

5.2 Establishment and Characterization of 3D Tumor Spheroids after Irradiation 112

5.3 The Proteomic Landscape of TNBC Spheroids-Derived Extracellular Vesicles 115

6. CONCLUSIONS 119

7. REFERENCIES 123

8. SUPPLEMENTARY DATA **135**

8.1 Figures **136**

8.2 Tables **141**

Figure and Table Index

Figure 1 - Demographic impact of Breast cancer in 2022 36
Table 1 - Breast Cancer risk factors 38
Figure 2– From screening to diagnose in Breast Cancer. 39
Figure 3 – Breast cancer molecular subtypes. 41
Figure 4 – Triple negative breast cancer molecular subtypes. 43
Figure 5 – Cellular mechanisms underlying the effects of radiotherapy in Triple negative breast cancer. 44
Figure 6 – Hallmarks of Radioresistance in Triple negative breast cancer 46
Figure 7 - Extracellular Vesicles-mediated radioresistance mechanisms in triple negative breast cancer. 48
Figure 8 – Characteristics of 2D and 3D models in in vitro studies. 49
Figure 9 – Tumor Spheroids formation illustrative scheme. 55
Figure 10 – Tumor spheroid irradiation scheme. 56
Figure 11 – Extracellular vesicles (EVs) isolation and characterization. 60
Table 2 – Antigen-specific and secondary antibodies used for western blot (WB). 61
Figure 12 - Establishment of radioresistant cell lines from two triple negative breast cancer subtypes. 67
Figure 13 – MDA-MB-231 radioresistant cell line shows smaller size and increased elongation in comparison with the parental MDA-MB-231 cell line. 68
Figure 14 – MDA-MB-468 radioresistant cell line shows significant increase size and roundness in comparison with the parental MDA-MB-468 cell line. 69
Figure 15 – 4T1 radioresistant cell line shows significant elongation in comparison with the parental 4T1 cell line. 70
Figure 16 – Characterization of culture media impact on 4T1 tumor spheroids, seeded with three different cell densities, over ten days of culture. 72
Figure 17 - Hypofractionated radiotherapy differently impacts cell survival and γ-H2AX expression in parental and radioresistant MDA-MB-231 cells. 74
Figure 18 - Hypofractionated radiotherapy has a distinct impact on parental and radioresistant MDA-MB-231 breast tumor spheroids. 75
Figure 19 - Hypofractionated radiotherapy differently impacts cell survival and γ-H2AX expression in parental and resistant MDA-MB-468 cells. 77
Figure 20 - Hypofractionated radiotherapy induces different survival and DNA damage repair between 4T1 and 4T1 RR cells. 78
Figure 21 - Hypofractionated radiotherapy induces differently impacts cell survival and γ-H2AX expression in parental and resistant MDA-MB-468 breast tumor spheroids. 80
Figure 22 - Hypofractionated radiotherapy induces differently impacts in cell survival and metabolic activity in parental and resistant 4T1 breast tumor spheroids. 81

Figure 23 - Hypofractionated radiotherapy induces distinct cell cycle arrest and reactive oxidative species (ROS) production between parental and radioresistant breast tumor spheroids. 85
Figure 24 - Proteomic analysis reveals significant cell signature alterations in 3D models. 88
Figure 25 – Radiotherapy impact study on TNBC spheroids. 90
Figure 26 - Hypofractionated radiotherapy induces distinct cellular effects across MDA-MB-231 breast tumor spheroids layers 93
Figure 27 - Hypofractionated radiotherapy impacts mitochondrial content and function in MDA-MB-231 breast tumor spheroids. 95
Figure 28 - Hypofractionated radiotherapy increases lipid droplets at the periphery of MDA-MB-231 breast tumor spheroids. 97
Figure 29 - Hypofractionated radiotherapy increases rough endoplasmic reticulum across all layers of the MDA-MB-231 breast tumor spheroids. 99
Figure 30 – Extracellular vesicles (EVs) isolated from triple negative breast cancer spheroids exposed to a clinical relevant radiotherapy scheme study. 102
Figure 31 – Ultracentrifugation combined with Ultrafiltration technique results in a high yield of extracellular vesicles from MDA-MB-231 breast tumor spheroids exposed to an hypofractionated radiotherapy. 103
Figure 32 – Hypofractionated radiotherapy increases extracellular vesicles production and size in MDA-MB-231 breast tumor spheroids. 106
Figure 33 - Ionizing radiation impacts the extracellular vesicles proteomic profile in MDA-MB-231 3D models. 108
Supplementary Figure 1 – Tumor spheroid Cell area and Cell-cell contact delimitation 137
Supplementary Figure 2 - Hypofractionated radiotherapy alters the proteomic signature of MDA-MB-231 breast tumor spheroids. 139
Supplementary Figure 3 - Tumor spheroid cells' endoplasmic reticulum location changes after irradiation. 139
Supplementary Figure 4 - Proteomic analysis of radiotherapy on tumor spheroids' organelle content. 140
Supplementary Table 1 – Top 3 ontology terms for biological process, molecular functions and cellular components for differentially expressed proteins between 2D and 3D model. 142
Supplementary Table 2 – Exclusive proteins identified for control or irradiated spheroids exposed to 5 fractions of 5.2 Gy (RT). 146
Supplementary Table 3 – Top 3 ontology terms for biological processes, molecular functions and cellular components for differentially expressed proteins after Irradiation. 146
Supplementary Table 4 – Exclusive proteins related with different organelles identified in control or irradiated spheroids, exposed to 5 fractions of 5.2 Gy. 148
Supplementary Table 5 - Top 3 ontology terms for biological process for differentially expressed proteins organelle identified in control or irradiated spheroids, exposed to 5 fractions of 5.2 Gy. 149

Supplementary Table 6 – Exclusive proteins related with EVs identified in control (CTR) or irradiated spheroids (RT), exposed to 5 fractions of 5.2 Gy (RT). 150

ABBREVIATIONS

2D	Two dimensional
3D	Three dimensional
ALIX	ALG-2-interacting protein X
AR	Androgen receptor / Aspect ratio
ASIR	Age-standardized incidence rate
ATM	Ataxia-Telangiectasia Mutated
ATP	Adenosine triphosphate
BC	Breast cancer
BCSCs	Breast cancer stem cells
BL1	Basal like 1
BL2	Basal like 2
BRCA1	Breast cancer 1
BRCA2	Breast cancer 2
BRIP1	BRCA1 Interacting Protein C-Terminal Helicase 1
BSA	Bovine serum albumin
CD44v3	Cluster of Differentiation 44 exon variant 3
CD63	Cluster of Differentiation 63
CD81	Cluster of Differentiation 81
CEM	Contrast enhanced mammography
CHEK1	Checkpoint kinase 1
CHEK2	Checkpoint kinase 2
CM	Conditioned media
DBT	Digital breast tomosynthesis
DCF DA	2′,7′-Dichlorodihydrofluorescein diacetate
DDR	DNA damage response
DNA	Deoxyribonucleic acid
DSB	Double strand break
ECM	Extracellular matrix
EGF	Epidermal growth factor
EGFR	Epidermal Growth Factor Receptor
ER	Estrogen receptor
ERBB2	Receptor tyrosine-protein kinase erbB-2
EVs	Extracellular vesicles
FDR	False discovery rate
GPCR	G protein-coupled receptor
H2AX	Histone H2A.X
HER2	Human epidermal growth factor receptor 2
HOX	Homeobox

IGF-1R	Insulin-like growth factor 1 receptor
IHC	Immunohistochemistry
IL-6	Interleukin-6
IM	Immunomodulatory
IR	Irradiation
IRDS	Interferon-related DNA damage resistance signature
JAG1	Jagged canonical Notch ligand 1
Ki-67	Antigen Kiel 67
LAR	Luminal androgen receptor
LINEs	Long Interspersed Nuclear Elements
LTRs	Long terminal repeat
M	Mesenchymal
MET	Hepatocyte growth factor receptor
miR/miRNA	MicroRNA
MRI	Magnetic resonance imaging
mRNA	Messenger RNA
MRN	MRE11, RAD50, and NBN (NBS1)
MRE11	Meiotic recombination 11 homolog A
MSL	Mesenchymal stem like
MVBs	Multivesicular bodies
NBN	Nibrin (Nijmegen breakage syndrome protein 1)
NCCN	National Comprehensive Cancer Network
ncRNAs	Non-coding RNAs
NF-κB	Nuclear factor kappa-light-chain-enhancer
NOTCH	Neurogenic locus notch homolog protein
OS	Overall survival
PALB2	Partner and Localizer of BRCA2
PARP	Poly (ADP-ribose) polymerase
PBS	Phosphate buffered saline
pCR	Pathological complete response
PD-1	Programmed cell death protein 1
PD-L1	Programmed death-ligand 1
PI	Propidium iodide
PR	Progesterone receptor
PTEN	Phosphatase and tensin homolog
P53	Cellular tumor antigen p53
RAB27	Ras-associated binding protein 27
RAD50	DNA repair protein RAD50
RHO	Ras homolog
RIBE	Radiation-induced bystander effect

RIG-I	Retinoic acid-inducible gene I
RNA	Ribonucleic acid
ROS	Reactive oxygen species
RR	Radioresistance
RS	Radiosensitive
RT	Radiotherapy
SDI	Social demographic index
SINEs	Short Interspersed Nuclear Elements
Slug	Zinc Finger Protein SNAI2
SNAIL	Zinc Finger Protein SNAI1
STAT1	Signal transducer and activator of transcription 1
STING	Stimulator of interferon genes
TCR	T Cell receptor
TGF-β	Transforming Growth Factor Beta
TME	Tumor microenvironment
TNBC	Triple negative breast cancer
TNF-α	Tumor necrosis factor alpha
TP53	Tumor protein p53
TWIST	Twist-Related Protein 1
Wnt/β-catenin	Wingless-related integration site and beta-catenin

Acknowledgements

"(…) Eh-lá o interesse por tudo na vida,

Porque tudo é a vida, desde os brilhantes nas montras

Até à noite ponte misteriosa entre os astros (...)"

Ode Triunfal, Álvaro de Campos, Fernando Pessoa

Gostaria de começar esta tese por agradecer a todos os que tornaram este objetivo de vida uma realidade. Mais do que uma conquista, este foi um percurso de dois anos que nunca esquecerei, pelo quão bonito, desafiante e revelador foi.

Assim, gostaria de começar por uma das pessoas que mais contribuiu para o meu gosto por esta área: a Doutora Flávia Castro. Há muitas palavras que me vêm à cabeça quando penso em ti, mas há uma que sobressai: gratidão. Gratidão pela pessoa que és e pelo apoio constante que me deste ao longo destes dois anos. Posso afirmar, sem hesitação, que foste uma das pessoas que mais me moldou e que me fez apaixonar por esta área, que hoje sinto como casa. Foi o teu entusiasmo pela ciência e pelo ensino que, há dois anos, me levou a escolher o Porto para realizar o meu mestrado. A tua atitude positiva e o teu inesquecível "Força, Guerreira!", levou-me nesta caminhada, um passo de cada vez, até chegarmos ao agora. Obrigada por acreditares sempre em mim foi uma honra aprender e crescer sob a tua orientação.

Outra pessoa que tornou este projeto possível foi a Doutora Maria José Oliveira. Haveria muito a dizer sobre si, mas gostaria de começar pelo mais importante: muito obrigada por me ter recebido no seu grupo de investigação e por todo o conhecimento, críticas construtivas e sugestões que tanto contribuíram para o desenvolvimento deste projeto. Nunca conheci uma pessoa como a Doutora Maria José Oliveira. A sua generosidade, bondade e imenso altruísmo tornaram esta experiência verdadeiramente especial. Foi um enorme orgulho poder dizer que fiz parte do seu grupo de investigação.

À Doutora Joana Carvalho, deixo também um agradecimento muito especial. Sempre que precisei de ajuda, de discutir ciência ou simplesmente de esclarecer alguma dúvida, estiveste sempre presente. Muito obrigada por toda a disponibilidade e apoio ao longo deste percurso.

Não poderia também deixar de agradecer ao meu querido TMI. Posso dizer, com toda a convicção, que não poderia ter escolhido melhor grupo para realizar este mestrado. Estiveram presentes não apenas nos momentos bons, mas também em todos os momentos mais difíceis. Neste grupo, que verdadeiramente considero uma família, ninguém fica para trás. Foi este espírito de entreajuda, confiança e união que tornou esta experiência tão especial. Gostaria de agradecer, em primeiro lugar, à Sara Silva, à Sofia Quintas e à Ana Borges, as minhas queridas doutoras (e quase doutoras), que estiveram sempre presentes ao longo deste processo. Muito obrigada por tudo: pelos fins de semana de ajuda, pelas conversas divertidas nas escadas e pelos abraços, tanto os físicos como aqueles que se sentem no coração. À Beatriz Sousa, a minha querida colega, só consigo dizer: muito obrigada por seres exatamente quem és! Foi durante o teu estágio no i3S que nos conhecemos e sinto que criámos uma ligação desde o primeiro momento. Desde então, tornaste-te uma das pessoas mais importantes deste percurso. Obrigada por todas as conversas, pelas palavras de motivação, pelos desabafos e por estares sempre presente durante este último ano. À querida Ângela Castro, Andrea Giestinhas, Sara

Moura, Bárbara Ferreira, Inês Vieira, Joana Almeida, Rui Marques, Diogo Estêvão e Miguel Mendes, obrigada por fazerem do TMI um lugar tão especial. Sem vocês, o TMI não seria o mesmo, e a minha jornada também não. Obrigada por todo o apoio, pela amizade e por todos os risos partilhados naquele instituto, que tornaram cada dia mais leve e mais feliz.

Gostaria também de agradecer à Catarina Meireles e à Emília Cardoso, da Unidade de Citometria de Fluxo, pela ajuda na utilização do citómetro e na análise dos resultados. À Sofia Pacheco e ao Rui Fernandes, agradeço o apoio na visualização das amostras por TEM. Às meninas do CDR, o meu agradecimento pelo fornecimento de anticorpos, mas também pela constante disponibilidade e vontade de ajudar.

Gostaria ainda de expressar o meu agradecimento à Professora Cármen Jerónimo pelo apoio prestado na realização deste projeto, bem como à Vera Gonçalves e à Íris pelo apoio constante na realização das irradiações.

À minha querida família, em especial ao meu pai e à minha mãe, nunca irei encontrar palavras suficientes para vos agradecer. Pelo apoio durante os dias de longas horas de trabalho, pelo amor incondicional e pela constante disponibilidade para me ajudarem em todos os momentos em que tudo parecia mais incerto: obrigada, do fundo do coração. Se não fossem vocês, tenho a certeza de que este caminho teria sido muito mais difícil e, quem sabe, talvez nem o tivesse percorrido. Por isso, aquilo que vos posso prometer é que serei eternamente grata por ter o privilégio de ser vossa filha. Escrevo estas palavras de coração cheio, a transbordar de amor e gratidão. Aos meus queridos avós, deixo também um profundo agradecimento. O vosso apoio incondicional às minhas decisões e os constantes lembretes sobre aquilo que realmente importa foram essenciais para me trazerem até aqui. Obrigada por serem um porto seguro e uma inspiração constante.

Aos meus amigos, aqueles que terão sempre um lugar muito especial no meu coração, só posso dizer: muito obrigada. Não apenas pelas inúmeras conversas, mas sobretudo por serem o ombro amigo que nunca falha, por estarem sempre presentes para me apoiar, levantar e acreditar em mim, mesmo quando eu própria duvidava. À Maria Macedo, à Ana Baixinha, à Daniela Luz, à Marta Seabra, ao Hélder Lobo e à Alessia Tirone, serei eternamente grata por vos ter na minha vida (I will always be eternally grateful to have you in my life).

Por último, gostaria de me agradecer a mim própria. Este percurso foi, sem dúvida, um dos mais bonitos que já vivi, mas também um dos mais desafiantes. Foi um caminho de crescimento, marcado por momentos de grande satisfação, mas também por dificuldades que me obrigaram a superar os meus próprios limites. Acima de tudo, permitiu-me confirmar o quanto gosto genuinamente daquilo que faço. Sempre me considerei uma pessoa motivada, dedicada e trabalhadora. No entanto, ao integrar este ambiente e ao enfrentar os inúmeros desafios que fui

ultrapassando — e outros que continuo, dia após dia, a vencer — percebi que ainda tenho muito para aprender, crescer e evoluir. E isso, longe de me desmotivar, faz-me sentir ainda mais entusiasmada e determinada para o futuro.

Se me perguntassem hoje o que diria a alguém prestes a viver esta experiência, responderia sem hesitar que vale verdadeiramente a pena. Para além de representar uma etapa fundamental para o crescimento profissional, é também uma experiência profundamente transformadora a nível pessoal. É uma aprendizagem que levamos para a vida, que nos desafia a sair da nossa zona de conforto, fortalece o nosso espírito crítico, desenvolve a nossa capacidade de adaptação, resiliência e autonomia, e nos faz crescer não só enquanto profissionais, mas, acima de tudo, enquanto pessoas.

Abstract

Triple negative breast cancer (TNBC) accounts for 10-15% of newly diagnosed breast cancer (BC) cases and is associated with a low 5-year survival rate, poor prognosis, and a high risk of local recurrence. Due to the lack of targeted therapeutic options, the standard treatment for TNBC consists of chemotherapy, surgery, radiotherapy (RT), and immunotherapy. RT, one of the main conventional treatment modalities, induces direct and indirect DNA damage, leading to cell death. However, a significant proportion of patients develop local recurrence, which is frequently associated with the acquisition of radioresistance.

Recently, extracellular vesicles (EVs), key mediators of intercellular communication, have emerged as important contributors of tumor progression and treatment resistance, including resistance to RT. By transferring a wide range of bioactive molecules, including proteins, lipids, DNA, mRNAs, and small miRNAs, to recipient cells, EVs can modulate cellular behaviour and promote the acquisition of a radioresistant phenotype in initially radiosensitive (RS) cells. Consequently, EVs represent promising sources of radioresistance-associated signatures and predictive biomarkers of RT response. Therefore, understanding the molecular mechanisms underlying cancer radioresistance, while considering EV-mediated communication within the tumor microenvironment (TME), is essential for the development of more effective therapeutic strategies.

Despite the clinical importance of RT, reliable preclinical models that faithfully recapitulate the heterogeneous response of TNBC to irradiation remain limited. Given the marked molecular heterogeneity of TNBC, this thesis aimed to develop biomimetic three-dimensional (3D) tumor spheroid (TS) models representing distinct TNBC subtypes and their corresponding radiosensitive (RS) and radioresistant (RR) phenotypes. These physiologically relevant models were used to characterize radiation-induced molecular alterations, investigate the mechanisms underlying RR, and evaluate how RT remodels the proteomic cargo of tumor spheroid-derived EVs.

To assess the suitability of these models for radiobiology studies, we evaluated the response of RS spheroids to a clinically relevant RT scheme. Our results demonstrated that MDA-MB-231 3D TSs undergo significant molecular and phenotypic alterations following RT, including increased metabolic activity, cell cycle arrest, and the accumulation of intracellular organelles, such as mitochondria, lipid droplets, and endoplasmic reticulum, particularly at the spheroid periphery. In addition, RT induced changes in EV production and phenotype, which were associated with the upregulation of pathways involved in DNA repair and nucleosome/chromatin binding. Further, these models reproduced well-established radioresistance-associated mechanisms, namely G2/M cell cycle arrest and reduced reactive oxygen species (ROS) levels, demonstrating their biological relevance. Furthermore, these biomimetic models provide a valuable platform for identifying molecules involved in RR, offering a particular advantage since TNBC patients

frequently receive neoadjuvant chemotherapy, making it difficult to distinguish the effects of chemotherapy from those induced by RT.

Overall, these breast tumor spheroids represent a robust and physiologically relevant model for radiobiology studies, providing a promising platform for identifying molecular signatures of radioresistance and for future investigations into the mechanisms underlying this phenotype.

Keywords: Triple negative breast cancer, radiotherapy, radioresistance, 3D models, extracellular vesicles

Resumo

O cancro da mama triplo negativo (TNBC) representa 10–15% dos casos de cancro da mama (BC) recentemente diagnosticados e está associado a uma baixa taxa de sobrevivência aos 5 anos, mau prognóstico e elevado risco de recorrência local. Devido à ausência de opções terapêuticas direcionadas, o tratamento padrão para o TNBC consiste em quimioterapia, cirurgia, radioterapia (RT) e imunoterapia. A RT, uma das principais modalidades de tratamento convencional, induz danos no DNA de forma direta e indireta, conduzindo à morte celular. No entanto, uma proporção significativa de doentes desenvolve recorrência local, que está frequentemente associada à aquisição de radioresistência.

Recentemente, as vesículas extracelulares (EVs), mediadores-chave da comunicação intercelular, emergiram como importantes mediadores para a progressão tumoral e para a resistência ao tratamento, incluindo a resistência à RT. Ao transferirem uma ampla variedade de moléculas bioativas, incluindo proteínas, lípidos, DNA, mRNAs e miRNAs, para células recetoras, as EVs podem modular o comportamento celular e promover a aquisição de um fenótipo radioresistente em células inicialmente radiossensíveis (RS). Consequentemente, as EVs representam fontes promissoras de assinaturas associadas à radioresistência e de biomarcadores preditivos da resposta à RT. Assim, compreender os mecanismos moleculares subjacentes à radioresistência no cancro, considerando simultaneamente a comunicação mediada por EVs no microambiente tumoral (TME), é essencial para o desenvolvimento de estratégias terapêuticas mais eficazes.

Apesar da importância clínica da RT, continuam a existir limitações em modelos pré-clínicos fiáveis que reproduzam de forma fiel a resposta heterogénea do TNBC à irradiação. Tendo em conta a acentuada heterogeneidade molecular do TNBC, esta tese teve como objetivo desenvolver modelos biomiméticos tridimensionais (3D) de esferoides tumorais (TS) representativos de diferentes subtipos de TNBC e dos seus correspondentes fenótipos RS e radioresistente (RR). Estes modelos fisiologicamente relevantes foram utilizados para caracterizar alterações moleculares induzidas pela radiação, investigar os mecanismos subjacentes à RR e avaliar de que forma a RT remodela a carga proteómica das EVs derivadas de esferoides tumorais.

Para avaliar a adequação destes modelos para estudos de radiobiologia, avaliámos a resposta de esferoides RS a um esquema de RT clinicamente relevante. Os nossos resultados demonstraram que os TSs 3D de MDA-MB-231 sofrem alterações moleculares e fenotípicas significativas após a RT, incluindo aumento da atividade metabólica, paragem do ciclo celular e acumulação de organelos intracelulares, como mitocôndrias, *lipid droplets* e retículo endoplasmático, particularmente na periferia do esferoide. Além disso, a RT induziu alterações na produção e no fenótipo das EVs, que foram associadas à regulação positiva de vias envolvidas na reparação do DNA e no *binding* a nucleossomas/cromatina. Adicionalmente, estes modelos reproduziram mecanismos de radioresistência bem estabelecidos, nomeadamente a

paragem do ciclo celular em G2/M e níveis reduzidos de espécies reativas de oxigénio (ROS), demonstrando a sua relevância biológica. Além disso, estes modelos biomiméticos constituem uma plataforma valiosa para identificar moléculas envolvidas na RR, oferecendo uma vantagem particular, uma vez que os doentes com TNBC recebem frequentemente quimioterapia neoadjuvante, tornando difícil distinguir os efeitos da quimioterapia daqueles induzidos pela RT.

Globalmente, estes esferoides tumorais da mama representam um modelo robusto e fisiologicamente relevante para estudos de radiobiologia, proporcionando uma plataforma promissora para a identificação de assinaturas moleculares de radioresistência e para futuras investigações dos mecanismos subjacentes a este fenótipo.

Palavras-chave: Cancro da mama triplo negativo, radioterapia, radioresistência, modelos 3D, vesículas extracelulares.

1. Introduction

1.1 Breast cancer as the leading cause of cancer in women: the global impact and risk factors

1.1.1 Epidemiology

Breast cancer (BC) is currently the leading cause of cancer related death in women worldwide. In 2022, BC had the highest proportion of diagnoses, accounting for 23,8% in women, and ranked first in mortality, representing 15,4% of all cancer-related deaths (**Figure 1A, B**). [1] Of all oncological patients as much as 36% are BC patients (**Figure 1C**). This disease has shown an upward trend in both incidence and mortality since 1990, with age-standardized incidence rate (ASIR) increasing from 16.42 cases per 100 000 individuals to 26.88 per 100 000 in 2021 over the past three decades.[2] Recent studies predict that this upward trend will continue, with incidence expected to increase by approximately 54% until 2050 in comparison to 2022.[2,3]

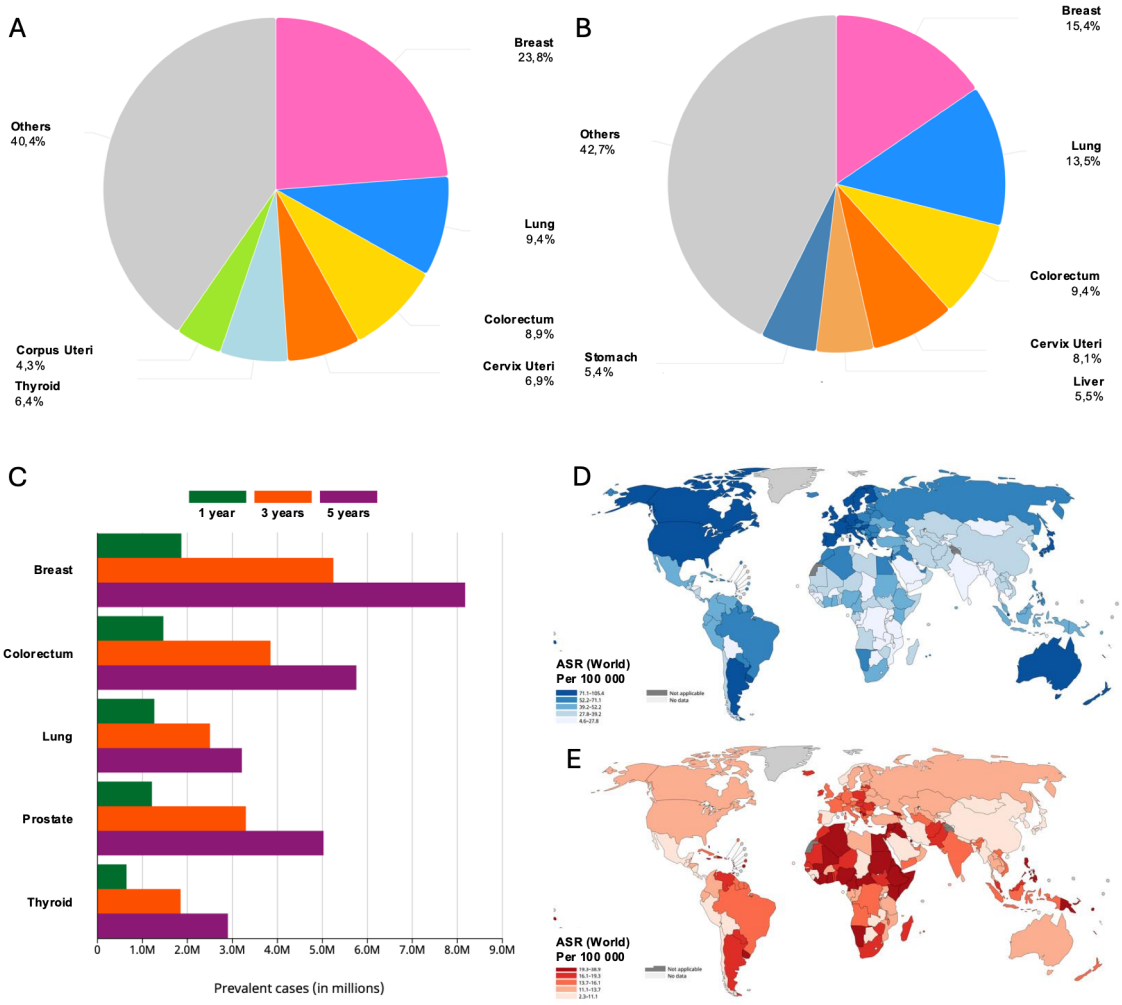


Figure 1 - Demographic impact of Breast cancer in 2022

(**A**) Incidence of all cancers (absolute number) and (**B**) mortality of all cancer (absolute number) in females. (**C**) Estimated number of prevalent cases for both sexes. (**D**) Incidence of breast cancer (BC) worldwide, age standardized incidence rates (ASIR) per 100 000 individuals, (**E**) mortality of BC, age standardized mortality rates (ASMR) per 100 000 individuals (world), in females.[4]

1.1.2 Demographic influence

The ASIR is globally raising, nevertheless, the most industrialized countries have the highest tendencies.[5] Currently, the overall burden of BC is positively associated with the social demographic index (SDI) which quantifies countries/regions development using fertility rates, education level and *per capita* income data.[5] The highest ASIR rates are found in high SDI areas whereas lower SDI regions have lower reported incidence rates, likely reflecting differences in risk factors, screening practices, and healthcare access (**Figure 1D**). Despite the lower incidence rates observed in developing countries, mortality remains disproportionately high and continues to increase (**Figure 1E**). This trend is likely associated with limited access to healthcare resources, including breast cancer screening, early diagnosis, and effective treatment. These findings highlight the urgent need to strengthen screening programs, improve healthcare infrastructure, and expand access to conventional therapeutic strategies in low-SDI regions.[2,5]

1.1.3 Risk factors

BC development extends beyond socioeconomic status and has been associated with a diverse range of risk factors, including both non-modifiable and modifiable factors (**Table 1**).[6] According to epidemiological evidence, gender, age and lifestyle-related factors are the major determinants of BC incidence and progression.[5]

Breast tumors appear predominantly in women, accounting for approximately 99% of all cases, whereas male BC is rare, with fewer than 100 new cases reported worldwide yearly.[5] Although BC is more commonly diagnosed in postmenopausal women, recent epidemiological data indicate a global increase in incidence among women within 30 years of age, with the incidence in premenopausal women doubling.[5] As mentioned above, the highest prevalence rates of BC are observed in high-income and highly developed countries. This pattern has been attributed to the adoption of a Western lifestyle, characterized by unhealthy dietary habits (e.g., high consumption of saturated fats and processed and red meats), tobacco use, chronic stress, physical inactivity combined with reproductive and demographic changes, including population ageing.[5]

In addition to these variables, factors as late first births, low parity, hormone replacement therapy, early menarches (under 12 years old), late menopauses (after 50 years old) and obesity are recognized as major risk factors of BC. These conditions contribute to prolonged lifetime exposure to hormone levels such as estrogens which raises the risk of breast carcinogenesis, by promoting tumor initiation and progression.[5] Interestingly, recent studies revealed that specific risk factors may be preferentially associated with distinct BC molecular subtypes. For example, high

mammographic breast density and ethnicity have been linked to an increased risk of triple negative breast cancer (TNBC), highlighting the heterogeneous etiologic of the disease.[7]

Intrinsic factors, including genetic predisposition, family history and benign breast changes, can also enable the increase of BC risk. Around 5 to 10% of the BC cases are hereditary and are mainly attributable to pathogenic germline variants in high-penetrance susceptibility genes.[8] Among these, mutations in *BRCA1* and *BRCA2,* which encode proteins essential for DNA damage repair and maintenance of genomic stability, respectively, are the underlying cause of BC in 3 and 5% of patients.[8] Additionally, genetic mutations in *TP53*, *PTEN*, *ATM*, *BRIP1*, *CHEK2* and *PALB2* have also been associated with an increased risk of BC development.[8] Nonetheless a positive family history of BC is another major determinant of BC risk. Women with one first-degree relative (e.g., a mother, sister) diagnosed with BC have an approximately two-fold higher risk of developing the disease, whereas the presence of two affected first-degree relatives increases this risk by three- to six-fold.[5,8]

Table 1 - Breast Cancer risk factors

Non-modifiable and modifiable risk factors mainly associated with increasing risk of breast cancer (BC) development. [6]

Breast Cancer Main Risk Factors	
Non-modifiable	**Modifiable**
Gender (Female)	Hormonal replacement therapy
Older age	Diethylstilbestrol
Family history	Low physical activity (sedentarism)
Genetic mutations	Obesity (Overweight)
Ethnicity	High alcohol intake
Early menarche / Older menopause	Smoking
Breast tissue density	Excessive exposure to artificial light
Previous history of breast cancer	High intake of processed food

1.2 Understanding breast cancer screening and treatment approaches

1.2.1 Screening and diagnosis

Early detection through screening programs is essential to reduce the incidence of late-stage BC, which is associated with poorer overall survival (OS).[9,10] Among the available screening modalities, mammography remains the gold standard screening modality in average-risk females and is recommended by most international guidelines.[9,10] Current recommendations generally advise annual or biennial screening between ages 40 to 74 years of age, resulting in an estimated 30% reduction in BC mortality compared with women who do not undergo routine screening.[10,11] Mammography consists in a low dose X-ray technique used for breast imaging.[10] This procedure encompasses some limitations due to the lack of sensitivity when tissue overlaps, normally

associated with breast density, or the presence of undetected small masses. To overcome these limitations, new techniques have been explored as digital breast tomosynthesis (DBT), contrast enhanced mammography (CEM) and more recently artificial intelligence which, in recent studies, showed higher BC detection rate.[9,10] For women at high-risk of developing BC annual mammography or magnetic resonance imaging (MRI) is advised starting at an earlier age in comparison with average-risk females (**Figure 2**). [9,12,13] Current guidelines from different regions worldwide show inconsistencies in the recommended age which screening should be initiated for the various high-risk groups. As such, there is a need to harmonize and improve protocols across the different guidelines.

In case of a suspicious lesion is identified, additional screening imaging is typically performed. If imaging findings remain highly suggestive of malignancy, histopathological confirmation is obtained by biopsy, which enables the collection of tissue sample for definitive diagnosis.[8,9]

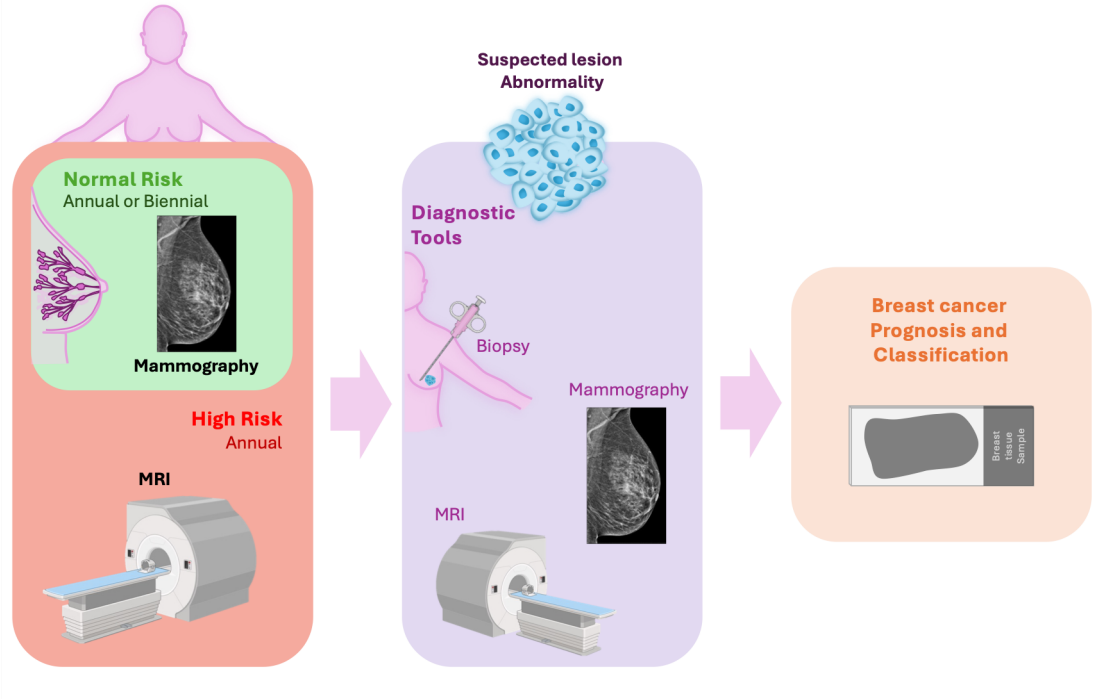


Figure 2– From screening to diagnose in Breast Cancer.

Overview of breast cancer (BC) screening approaches for normal- and high-risk populations, the subsequent diagnostic pathway and associated imaging techniques, and the molecular classification of BC with its corresponding prognosis. (Created with BioRender.com)

Following diagnose, the treatment of breast tumors involves a multidisciplinary process regarding local and systemic treatments. These encompass surgery, chemotherapy, radiotherapy, target therapy, immunotherapy and hormonotherapy. To select the most suitable option, stage and BC subtypes are taken in consideration. In case of non-metastatic disease, which represents more than 90% of cases, the primary treatment objective, is tumor removal and the reduction of tumor recurrence probability. However, in case of metastatic disease, the main treatment objective is to prolong survival and maintain quality of life, with treatment depending mainly on BC subtype.[14]

1.2.2 Breast cancer classification

Breast tumors are currently classified according to their histopathological subtype and molecular characteristics.[9] This classification system provides valuable prognostic information, prediction of treatment response and guided personalized therapeutic management.[15–17] In most cases, tumors originate from the epithelial tissue of the breast, known as carcinomas, which can appear in the lobular zone (lobular carcinoma) or ductal zone (ductal carcinoma) of the breast (**Figure 3**). Depending on the presence of cancer cells on the surrounding tissues or in other organs, BC can further be classified as *in situ*, invasive or metastatic.[9] Carcinoma *in situ* is confined to the ducts or lobules without breaching the basement membrane, whereas invasive carcinoma is characterized by the infiltration of malignant cells into the surrounding breast stroma, enabling local progression and dissemination to regional lymph nodes and distant organs. Metastatic BC (stage IV) represents the most advanced stage of the disease and is defined by the presence of tumor cells in distant organs. Despite this classification providing valuable diagnostic and prognostic information, it does not fully capture the biological heterogeneity of BC. Tumors with similar histological features may exhibit markedly different proliferative capacities, metastatic potential, therapeutic responses, and clinical outcomes. Due to its heterogeneous nature, BC is further classified into distinct molecular subtypes based on the expression of clinically relevant biomarkers, including estrogen receptor (ER), progesterone receptor (PR) and human epidermal growth factor receptor 2 (HER2), and, in routine clinical practice, the proliferation marker Ki-67.[9,18]

The BC molecular characterization has evolved considerably over the past decades and has transformed both prognosis assessment and therapeutic decision-making. Starting around 1960s, the first clinically relevant biomarker was identified, the ER.[19] Initially, ER expression was recognized as a predictor of response to endocrine therapy and was subsequently established as an important prognostic marker associated with disease recurrence and patient outcome. Further studies demonstrated a close relation between ER and PR expression, as PR is a downstream target gene of ER signaling. Moreover, the lack of PR in an ER+ tumor was associated with an aggressive phenotype, poorer prognosis, and reduced sensitivity to endocrine therapies, including tamoxifen. Later, the subsequent identification of HER2, encoded by the *ERBB2*, further refined BC classification. In 1967, HER2 overexpression was associated with increased tumor proliferation, aggressiveness, and historically poor clinical outcomes.[19]

Therefore, the assessment of these biomarkers allowed the definition of four major BC subtypes that are routinely used in clinical practice: Luminal A-like, Luminal B-like, HER2+ and TNBC. These subtypes differ substantially in their molecular characteristics, biological behaviour, prognosis, and therapeutic response, forming the basis of personalized treatment strategies. Luminal tumors represent 60-70% of all BC cases and comprise Luminal A-like and Luminal B-like subtypes. Luminal A-like tumors are typically characterized by the high expression of ER and PR and absence of HER2 overexpression (ER+, PR+, HER2-), as well as by a low proliferation index. Accounting for nearly 50% of all BC cases, they are associated with the most favourable

prognosis and respond well to endocrine therapies.[9,20] Luminal B-like tumors also express ER but generally exhibit lower or absent PR expression, higher proliferative activity, and may be either HER2-negative or HER2-positive (ER+, PR-, HER2+/-). Compared with Luminal A-like tumors, they display a more aggressive clinical behaviour, higher risk of recurrence, and reduced responsiveness to endocrine therapies, often requiring chemotherapy in addition to hormonal treatment.[9,21] HER2+ BC is characterized by HER2 overexpression, irrespective of hormone receptor status, although the HER2-enriched subtype is classically hormone receptor-negative (ER-, PR-, HER2+). These tumors are highly proliferative and exhibited poor clinical outcomes. However, the development of HER2-targeted therapies (trastuzumab) followed by other anti-HER2 agents, has dramatically improved survival and transformed the prognosis of patients with HER2-positive disease.[9,22]. Lastly, the most aggressive subtype, known as TNBC represents around 10-15% of all BC patients. TNBC is defined by the absence of ER, PR, and HER2 expression and is characterized by high proliferative capacity, marked genomic instability, and an increased propensity for early recurrence and distant metastasis. Although recent advances, including immune checkpoint inhibitors, PARP inhibitors, and antibody–drug conjugates, have expanded treatment options for selected patient populations, TNBC remains the subtype with the poorest prognosis and the highest unmet clinical need.[23]

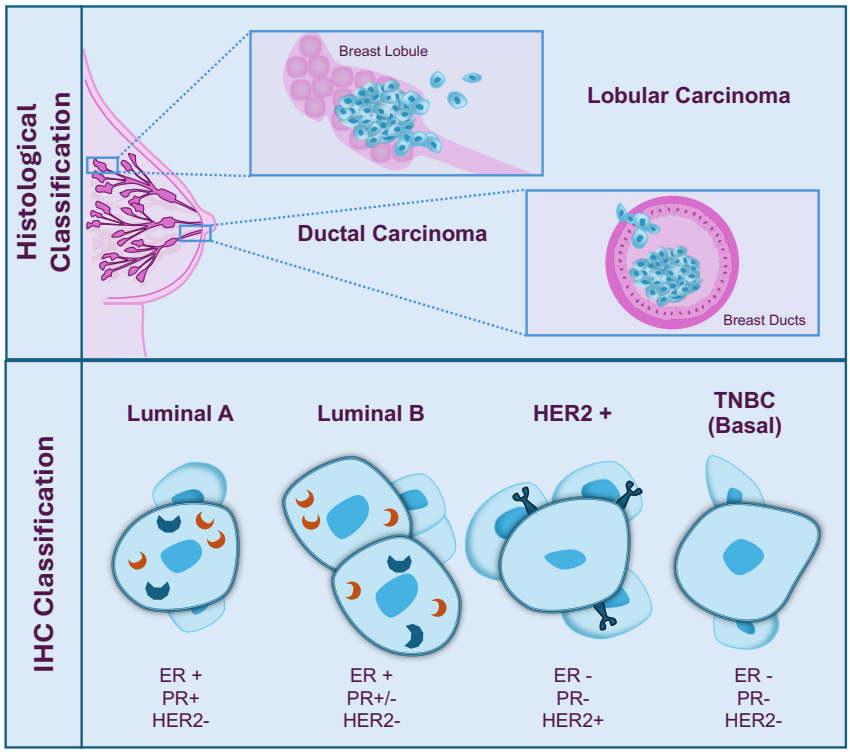


Figure 3 – Breast cancer molecular subtypes.

Breast cancer (BC) is classified, clinically, based on different systems: histological and Immunohistochemistry (IHC) classification. Histopathological classification allows the determination of initial growth area (ductal or lobular carcinoma, in most cases). IHC classification leads to the discovery of the presence or absence of BC markers (estrogen receptor (ER), progesterone receptor (PR) and human epidermal growth factor receptor 2 (HER2)) and proliferative markers (ki67), further dividing BC into Luminal A-like, Luminal B-like, HER2+ and TNBC.

1.3 Triple negative breast cancer: the global burden

1.3.1 Epidemiology

TNBC is a highly aggressive BC subtype that occurs more frequently in younger, premenopausal women, particularly those under 40 years of age, although it can affect women of any age. These tumors correspond to 10-15% of all BC cases and are characterized by an aggressive clinical course, high histological grade, rapid proliferation, an increased risk of early recurrence, distant metastasis, and an overall poorer prognosis compared with other BC subtypes.[18,24,25] Patients with TNBC have the lowest survival rates of all BC subtypes. While the 5-year OS rate of early-stage TNBC patients reaches over 75-85%, it dramatically declines to 10-15% once the disease progresses to a metastatic stage. Among patients who develop metastatic recurrence, the prognosis is particularly poor, with rapid disease progression and substantially reduced post-recurrence survival rates of 12 to 18 months.[26]

1.3.2 TNBC subtypes

At a molecular level, TNBC is a very heterogenous disease, which contributes to its variable clinical behaviour and treatment response. Through a molecular analysis, in 2011, Lehmann *et al.* stratified TNBC into six subtypes: Basal like 1 (BL1), basal like 2 (BL2), immunomodulatory (IM), mesenchymal (M), mesenchymal stem-like (MSL) and luminal androgen receptor (LAR). These subtypes differ in their gene expression profiles, activated signalling pathways and sensitivity to therapeutic agents.[26–28]

The basal-like TNBC subgroup encompasses the BL1 and BL2 subtypes; however, each present distinct molecular characteristic. BL1 is enriched in genes involved in cell cycle regulation and DNA damage repair genes signatures while BL2 is characterized by the activation of encloses pathways as EGFR, MET, Wnt/β-catenin and IGF-1R promoting tumor cell proliferation, stemness and survival. The IM subtype is enriched in immune-associated genes and signal pathways, suggesting potential responsiveness to immune therapies, including PD-1/PD-L1 immune checkpoint inhibitors. The M subtype exhibits activation of signalling pathways associated with cell migration, extracellular matrix (ECM) interactions, and cellular differentiation. In contrast, the MSL subtype is characterized by high expression of stemness related genes, HOX genes and mesenchymal stem cell specific markers. Lastly, the LAR subtype displays the most distinct molecular profile, characterized by the abnormal activation of hormone-related signalling pathways and high expression of androgen receptor (AR). Among the different TNBC subtypes, LAR is associated with higher metastasis free and OS while M and BL2 subtypes exhibit the poorest prognosis.[26] These diverse characteristics highlight the need for subtype-specific therapeutic strategies and predictive biomarkers, reinforcing TNBC as a heterogeneous disease rather than a single clinical entity (**Figure 4**).

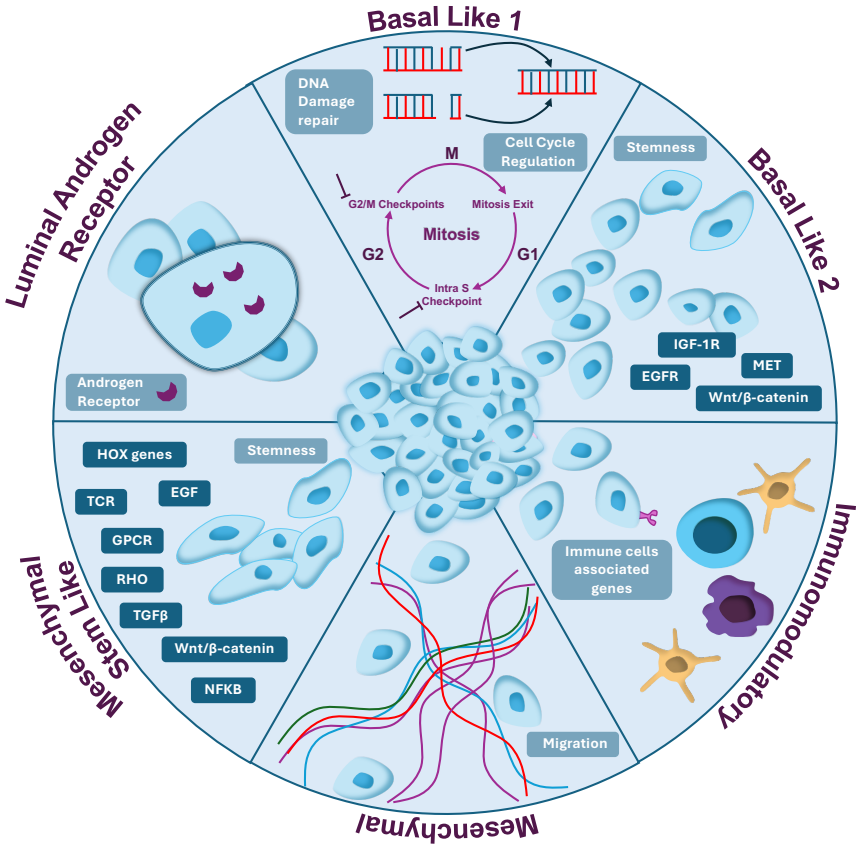


Figure 4 – Triple negative breast cancer molecular subtypes.

Triple negative breast cancer (TNBC) is currently divided into six different subtypes based on the molecular profile of tumor cells. Basal like 1 (BL1) is associated mainly with gene signature involving DNA damage repair and cell cycle functions. Basal like 2 (BL2) is associated with high proliferation and stemness. Immunomodulatory (IM) subtype is related with gene signature linked with immune cells. Mesenchymal (M) displays high activation of pathways associated with migration, differentiation and extracellular matrix (ECM) interaction. Mesenchymal stem like (MSL) subtype is associated with stemness and HOX genes. Lastly, luminal androgen receptor (LAR) expresses high levels of androgen receptors (AR).

1.3.3 Treatments

Insensitive to targeted therapies, TNBC standard treatment involves neoadjuvant chemotherapy, surgery, adjuvant radiotherapy (RT) and, more recently, immunotherapy.[29] Neoadjuvant chemotherapy aims to reduce tumor burden and size before surgery, facilitating breast-conserving procedures and improving pathological complete response (pCR) rates and long-term clinical outcomes.[30] According to the National Comprehensive Cancer Network (NCCN) 2022 Breast Cancer Guidelines, the recommended neoadjuvant regimens are primarily based on anthracyclines and taxanes, with the addition of platinum agents in selected patients due to their demonstrated clinical benefit.[30] Although this treatment exhibits pCR rates of approximately 35-45%, a significant part of patients still develops drug resistance, ultimately leading to disease recurrence and poor prognosis.[30] Despite recent advances, systemic therapy remains the conventional approach for most TNBC patients, highlighting the urgent need for more effective personalized treatments.[31] Following neoadjuvant chemotherapy, patients undergo surgical resection, either by the removal of the whole breast (mastectomy) or breast-conserving surgery

(lumpectomy). Adjuvant RT is frequently applied afterwards to eliminate residual tumor cells, thus reducing local recurrence and improving OS of TNBC patients.[32]

1.4 Understanding radiotherapy in TNBC: mechanisms and clinical implications

1.4.1 Molecular mechanisms underlying irradiation

RT, a key treatment modality in TNBC, exerts its therapeutic effects by inducing direct and indirect DNA damage, ultimately promoting tumor cell death while minimizing damage to the healthy tissues.[33] Direct irradiation (IR) effects involve the induction of DNA damage, particularly double-strand breaks (DSBs), which are considered the most cytotoxic form of DNA damage. Indirectly, ionizing IR interacts with intracellular water molecules generating free radical species, as reactive oxygen species (ROS), that further damage DNA, proteins and lipids, disrupting essential cellular processes, such as proliferation, cell cycle progression, and survival. Collectively, these effects lead to the elimination of residual tumor cells and contribute to local tumor control (**Figure 5**).[25,33]

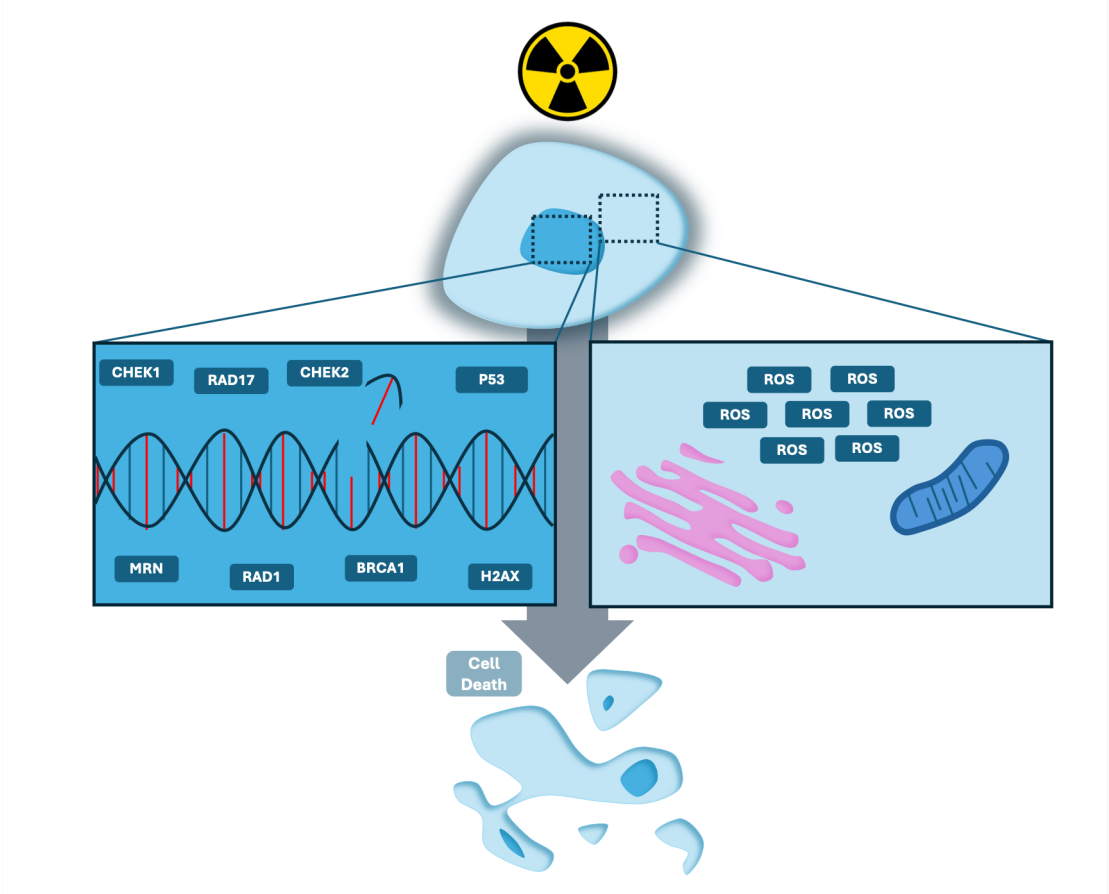


Figure 5 – Cellular mechanisms underlying the effects of radiotherapy in Triple negative breast cancer.

Ionizing radiation induces direct DNA damage and indirect oxidative damage through the generation of reactive oxygen species (ROS), disrupting essential cellular processes. When DNA repair mechanisms fail (e.g. *CHEK1/2*, *RAD1*, *RAD17*, *MRN* complex, *BRCA1*, *P53*, *H2AX*) these effects culminate in tumor cell death.

1.4.2 RT clinical history

To obtain the most efficient treatment response, IR dosage and fractionation schemes are modulated based on tumor type, size, stage and anatomical location.[33] In TNBC prior RT schemes focused on the delivery of a total of 50 Gy which were equally distributed over 25 fractions throughout 5 weeks of treatment. The inclusion of this treatment decreased local reoccurrence rates by more than 20%.[33] However previous studies observed a correlation between the number of fractions and healthy tissue injury. Accordingly, increasing the number of radiation fractions results in a higher damage of healthy tissue, paving a way towards the exploration of shorter RT schemes. Multiple studies explored hypofractionated plans which involved the delivery of more than 2 Gy per fraction. Hypofractionated schemes, involving the delivery of more than 2 Gy per fraction, have been shown to be as safe and effective as conventional RT schemes in the treatment of BC.[34]

More recently, ultra hypofractionated schemes, which involve the delivery of more than 5 Gy per fraction, have emerged. These IR schemes demonstrated local reoccurrence control, as conventional and hypofractionated schemes, and low toxicity levels in healthy tissue. Indeed, this approach has already been integrated into the clinical practice in multiple centres across Europe due to its economic benefits and improvements on both the quality of life of patients and health care instituitions.[34,35]

Despite the clinical benefits of RT, approximately 15–20% of TNBC patients still develop local recurrence following treatment, which is frequently associated with the acquisition of radioresistance (RR). [25,36]

1.4.3 Radioresistance in TNBC

RR, first described in 1904, is defined as the ability of tumor cells to survive and proliferate upon RT exposure, thereby decreasing RT effectiveness or even inducing treatment failure.[36] In TNBC, RR remains a major clinical challenge and represents one of the principal causes of local recurrence and poor patient outcomes. Over the past years, extensive research has identified several molecular and cellular mechanisms that contribute to the development of RR in TNBC (reviewed by our team in Canha-Borges A. et al 2025 [25]).

Current evidence indicates that RR results from the interplay between tumor cell-intrinsic mechanisms and the tumor microenvironment (TME).[36] Intrinsic mechanisms include DNA damage repair, activation of cell cycle checkpoints, particularly at the G2/M phase, evasion of apoptosis, and dysregulation of non-coding RNAs (ncRNAs) all of which promote tumor cell survival after IR.[36,37] Among ncRNAs, microRNAs (miRNAs) have emerged as important regulators of RT response through the modulation of DNA repair pathways, cell cycle progression, apoptosis, and stemness. Moreover, breast cancer stem cells (BCSCs), which exhibit increased

DNA repair capacity, self-renewal potential, and resistance to cell death, have been implicated in RR acquisition (**Figure 7**).[25,36]

The TME also plays a pivotal role in modulating the response to RT. Radiation-induced remodelling of the TME can alter the recruitment and activation of immune cells, promoting either anti-tumor immune responses or an immunosuppressive environment that favours tumor progression and RR.[25] Consequently, the dynamic interactions between tumor cells and stromal and immune components are increasingly recognized as critical determinants of RT response.[25,38,39]

Beyond these mechanisms, intercellular communication has emerged as a key contributor to RR.[25] Communication between tumor cells and the surrounding microenvironment occurs through cell-cell contact (e.g., gap junctions), secreted small molecules, and extracellular vesicles (EVs). In fact, several studies have reported that RT enhances EVs secretion, while EVs released by RR TNBC cells can transfer bioactive cargo, including proteins, lipids, and nucleic acids, to radiosensitive (RS) cells.[25] This horizontal transfer promotes the acquisition of radioresistant traits, resulting in enhanced survival following IR and suggesting that EVs are important mediators for the propagation of the RR phenotype (**Figure 6**).[25,40]

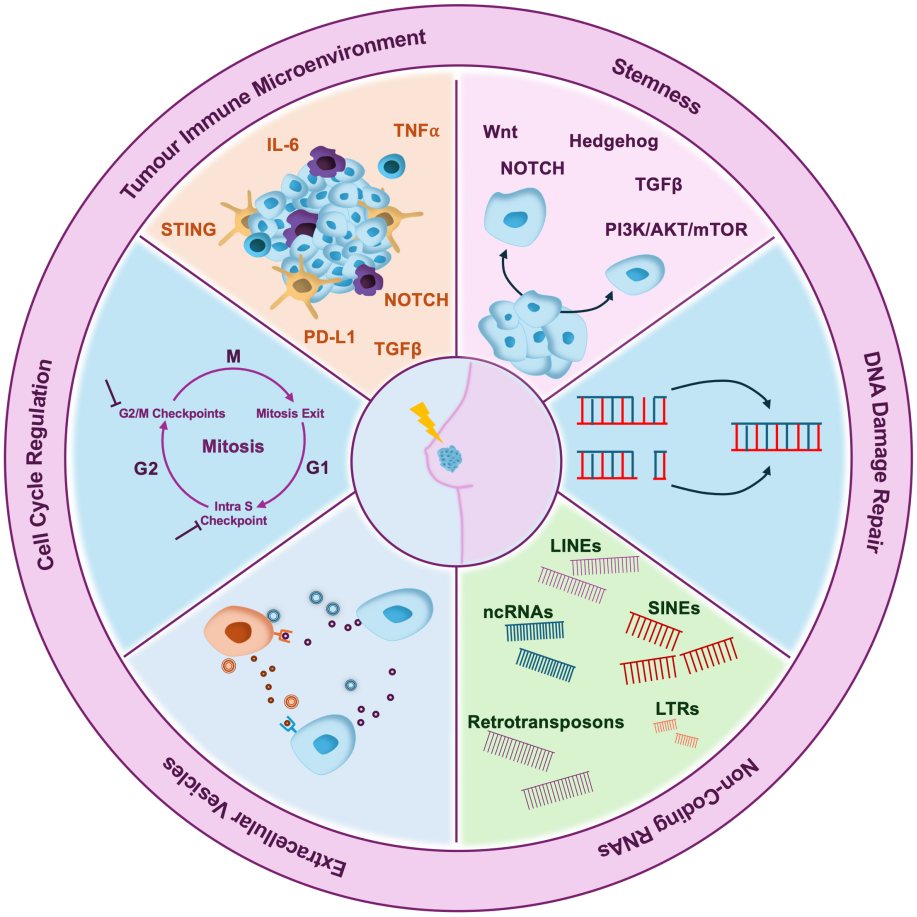


Figure 6 – Hallmarks of Radioresistance in Triple negative breast cancer

(Reprinted from A. Canha-Borges, B. Nunes et al, Cancer and Treatment Reviews (2025))[25]

1.5 Extracellular vesicles in radioresistance: emerging players

1.5.1 EVs composition and structure

Extracellular vesicles (EVs) key mediators of intercellular communication have emerged as potential contributors to TNBC progression and RR.[40,41] EVs were first described in 1964 and are membrane-enclosed heterogeneous nanoparticles released by virtually all cell types. Depending on the size, they can be further categorized into exomeres (<50nm), exosomes (30-150nm), microparticles (100-1000nm), migrasomes (500-3000nm), apoptotic bodies (50nm – 5μm) and oncosomes (1000 – 10 000nm).[42] The biogenesis of these vesicles involves different processes. Exomeres are secreted from the cells through the cleavage of large cytoplasmatic extensions of the cellular body.[42] Microparticles are produced through outward budding and shedding of the plasma membrane driven by actin and cytoskeletal rearrangement, a process that can be regulated via EGFR signalling. In contrast, exosomes originate from the endosomal pathway through the formation of multivesicular bodies (MVBs).[43] Migrasomes another subtype of EVs originated via fibers retraction that occurs during cellular migration. Lastly, the apoptotic bodies are formed during apoptosis through membrane blebbing and fragmentation of dying cells.[44] After release, the EVs can be internalized by recipient cells through three main mechanisms: endocytosis, receptor mediated interactions and direct fusion with the cell membrane.[45]

EVs transport a wide variety of bioactive molecules, including proteins, lipids, DNA, mRNAs, and small miRNAs, thereby modulating the phenotype and function of recipient cells. Through this cargo transfer, EVs may influence several cellular processes involved in the acquisition of RR in RS cells.[40,46] These findings highlight the potential of EVs as a source of radioresistance-associated molecular signatures and possible predictive biomarkers of RT response.

1.5.2 EVs and TNBC interplay

Previous studies have demonstrated that cancer cells can reprogram surrounding cells, disrupting tissue homeostasis to create a microenvironment that favours cancer progression and therapeutic resistance.[47,48] In TNBC, accumulating evidence suggests that EVs play a central role in this process. In fact, by mediating intercellular communication, EVs influence several hallmarks of cancer, including tumor growth, invasion, metastasis, immune regulation and drug resistance, thereby contributing to treatment failure and poor patient outcomes.[45]

EVs derived from breast cancer cells, as well as from immune and stromal cells, have been shown to promote a radioresistant phenotype in TNBC by transferring bioactive cargo that reprograms recipient cells behaviour and function (reviewed by our team in Canha-Borges A. et al 2025 [25]) (**Figure 7**).[45]

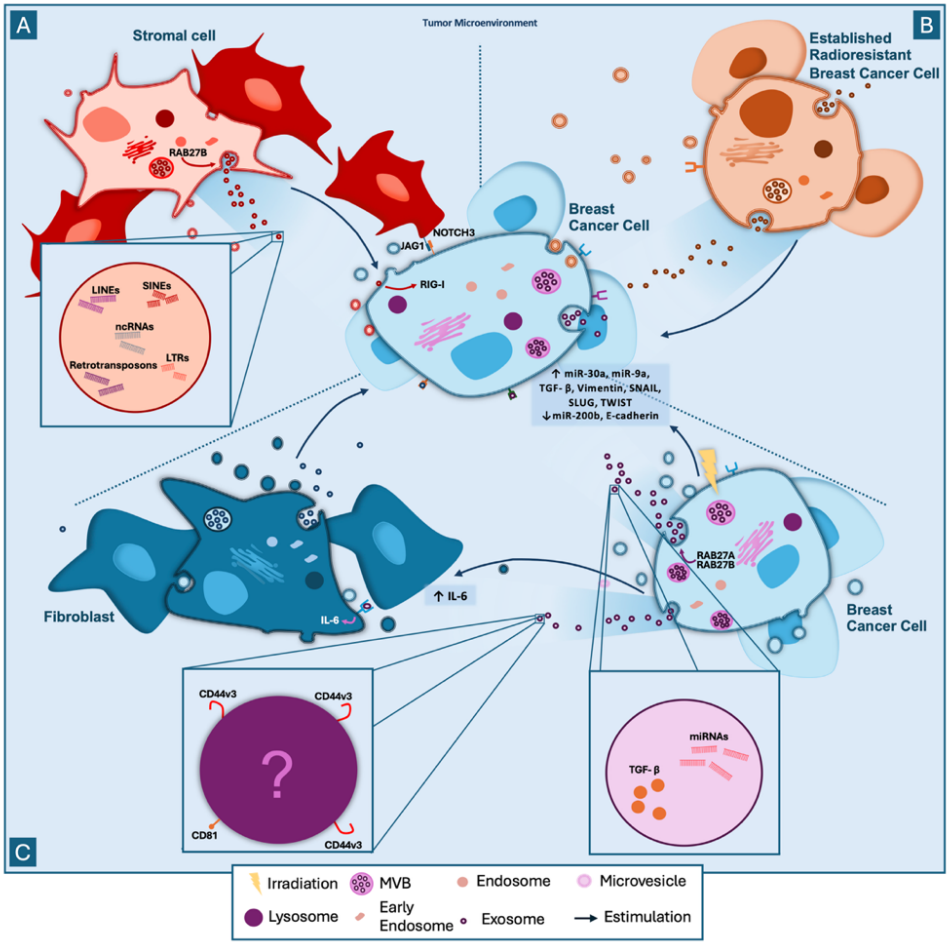


Figure 7 - Extracellular Vesicles-mediated radioresistance mechanisms in triple negative breast cancer.

A. Stromal cells interact with TNBC cells through juxtacrine communication which involves JAG1 and NOTCH3 as well as paracrine communication which leads to the activation of RIG-I pathway. The exosomes released during this process have a high content of multiple RNAs, such as LINEs (Long interspersed nuclear elements), SINEs (Short interspersed nuclear elements), ncRNAs (noncoding RNAs), retrotransposons and LTRs (Long terminal repeats) which stimulate the pattern recognition receptor RIG-I, activating STAT1-dependent antiviral signaling. The involvement of both processes leads to the increased expression of IRDS (interferon-related DNA damage resistance signature) genes and RT resistance in a STAT1-dependent manner.
B. Exposure of radiosensitive (RS) TNBC cells to exosomes of radioresistant (RR) TNBC cells leads to significant increase of RS TNBC cells survival, metastases and stemness potential.
C. TNBC cells, upon irradiation (IR), release a significant amount of EVs due to the increased expression of Rab27A/B. These contain miRNAs and TGF- β which, when partaken by other TNBC cells, leads to the increase expression of miR-30a, miR-9a, TGF-β, Vimentin, SNAIL, SLUG and TWIST, while miR-200b and E-cadherin are inhibited. However, when fibroblasts are present, TNBC cells can release exosomes, which show in the surface CD44v3 and CD81, thus impacting the production of IL-6 and favoring the tumor microenvironment.
(Reprinted from A. Canha-Borges, B. Nunes et al, Cancer and Treatment Reviews (2025))[25]

1.6 3D models in radiobiology: insights and roles

To develop more effective therapies that address the current clinical needs in TNBC, it is crucial to understand the molecular signatures and cellular mechanisms underlying RR. To address this challenge, there is a critical need for more physiologically relevant preclinical models that faithfully recapitulate the TME and its complex intercellular communication networks. Three-dimensional

(3D) tumor spheroid models provide a valuable platform to investigate the molecular and cellular mechanisms driving RR under conditions that better mimic the *in vivo* tumor architecture.[49]

1.6.1 Benefits and structure of 3D models

3D tumor models have been widely studied due to the increasing need to develop a higher accuracy of the complexity of tumor biology.[50] These models reproduce key features of the TME, including cell-cell and cell-ECM interactions, as well as physiologically relevant nutrients, oxygen, and metabolite gradients.[50–52] Moreover, the formation of different cell layers - proliferative, quiescent and necrotic - within spheroid structure, resulting from spatial heterogeneity in nutrient and oxygen availability, closely resembles the architecture of *in vivo* tumors. Consequently, 3D spheroid models provide a more physiologically relevant platform than traditional 2D cultures, which are limited to simplified cell interactions and homogeneous growth conditions (**Figure 8**).[53]

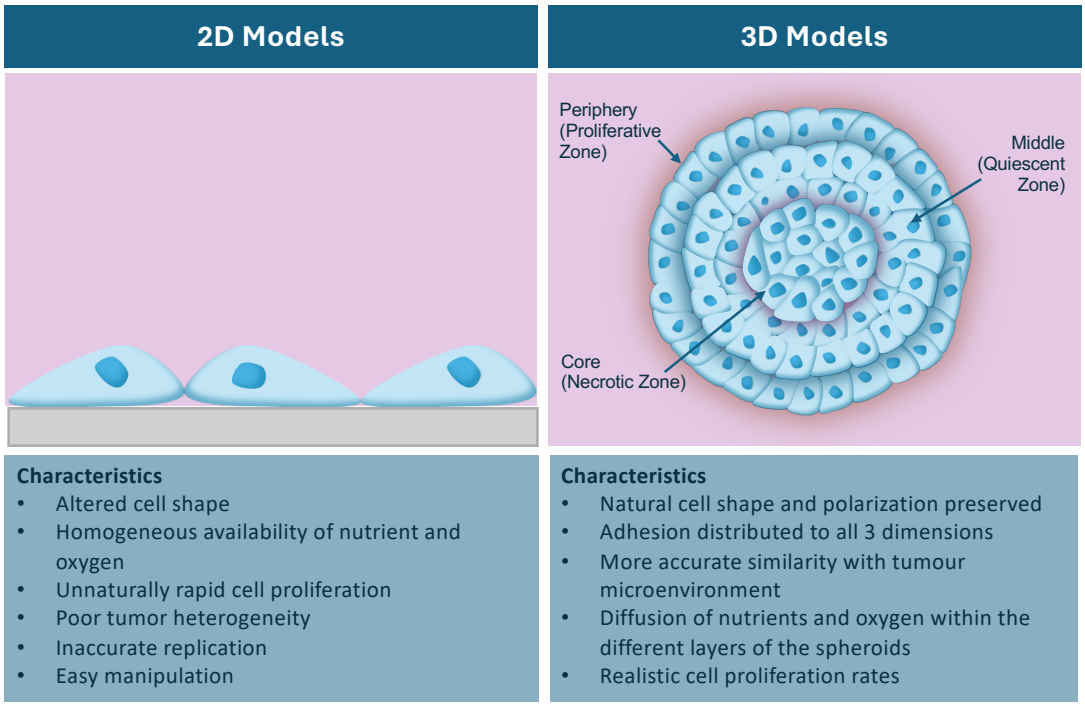


Figure 8 – Characteristics of 2D and 3D models in *in vitro* studies.

1.6.2 Relevance of 3D models in radiobiology

In the field of radiobiology, 3D spheroids have not yet been fully established as the gold-standard *in vitro* model for investigating RR. However, they present significant advantages over conventional 2D cultures due to their heterogenous behavioural nature and diffusion of nutrients and oxygen. These characteristics promote the development of microenvironmental conditions associated with RR, particularly hypoxia, which is normally present within the spheroid core and contributes to a more aggressive tumor phenotype.[54] Additionally, several studies have

demonstrated that cells grown in 3D models exhibit lower radiosensitivity than their 2D counterparts across multiple cancer cell lines.[55]

Collectively, these features make 3D tumor spheroids a promising preclinical platform for investigating the molecular mechanisms underlying RR, evaluating clinically relevant fractionated RT regimens, and screening novel radiosensitizing agents under conditions that more faithfully recapitulate the in *vivo* tumor microenvironment.

2. Aim of the project

TNBC is an aggressive subtype of BC characterized by the absence of ER, PR, and HER2 expression. The lack of these therapeutic targets, together with its high malignancy, contributes to a poor prognosis. Although adjuvant RT is the standard treatment to reduce the risk of local recurrence, a significant proportion of patients still develop RR. Therefore, understanding the molecular signatures and mechanisms underlying cancer RR is essential for the development of more effective therapeutic strategies.

Increasing evidence indicates that the TME actively contributes to the acquisition of RR through a dynamic intercellular communication. Among the mediators of this communication, EVs have emerged as critical regulators of tumor progression and therapeutic resistance by transferring bioactive cargo capable of reprogramming recipient cells. However, the contribution of EV-mediated signalling to RR in TNBC remains poorly understood. The advances in deciphering these mechanisms have been hindered by the limited availability of physiologically relevant experimental models. While conventional 2D cultures fail to reproduce the complex architecture and heterogeneity of solid tumors, 3D spheroids more accurately recapitulate key features of the tumor microenvironment, including cell-cell interactions and gradients of oxygen, nutrients, and metabolites as well as spatially distinct proliferative, quiescent and necrotic regions. These characteristics make 3D spheroids an attractive platform for investigating both cellular adaptations to IR and the role of EV-mediated communication in the development of RR.

Based on this, we hypothesize that biomimetic 3D TNBC models can faithfully reproduce key features of the TME and provide a robust platform to identify cellular and molecular mechanisms driving RR, including those mediated by EVs. Here, we established syngeneic RS and RR TNBC spheroids that enable the spatial characterization of tumor cell responses to a clinically relevant RT regimen. Furthermore, this platform provides a valuable tool to investigate EV-mediated intercellular communication and identify the molecular signatures associated with RR.

To address these questions, we established biomimetic 3D TNBC RS and RR spheroids and analysed EV secretion in RS TNBC spheroids. The specific objectives of this thesis are:

1. Establishment and characterization of syngeneic radioresistant human and mouse TNBC cell lines;

2. Establishment and spatial characterization of 3D tumor spheroids after irradiation;

3. Unveiling the proteomic landscape of TNBC spheroids-derived extracellular vesicles

3. Methods and Materials

3.1 Cell culture

The MDA-MB-231 and MDA-MB-468 human breast cancer cell lines as well as 4T1 mouse breast cancer cell line, kindly provided by Dr. Joana Paredes (i3S, Porto Portugal), were authenticated through short tandem repeat profile analysis and tested for mycoplasma monthly. These cells were cultured and expanded to 70-80% confluence in Dulbecco's Modified Eagle Medium (DMEM) High Glucose (Gibco) supplemented with 10% Fetal Bovine Serum (FBS) (Biowest) and 1% Penicillin-Streptomycin (P/S) (10,000 U.mL-1) (Capricorn Scientific). Cells were cultured in a humidified atmosphere containing 5% CO_2 at 37 ºC.

3.2 Development of radioresistant cell lines

Radioresistant cell lines, MDA-MB-231 RR, MDA-MB-468 RR and 4T1 RR cells, were established from their respective parental cell lines, MDA-MB-231, MDA-MB-468 and 4T1 respectively, using a 7-week protocol from [56]. Briefly, cells were irradiated by a PRIMUS (Siemens, Malvern, PA, USA) linear particle accelerator, used for human radiotherapy, and was operated by a member of the Radiotherapy Service of IPO-Porto. To guarantee the uniformed dosage, a water plate was placed between the cell flask and the radiation source. Radioresistant cell lines were developed by weekly exposure to single fractions of radiation. An initial dose of 2 Gy was followed by weekly incremental doses of 2 Gy, followed by 3 doses of 10 Gy, totalizing a radiation dose of 50 Gy. Cells were then allowed to rest and expand and were further cultured in the same conditions as their parental cell lines.

3.3 Clonogenic assay

Clonogenic assay was developed using 6-well treated plates. Briefly, cells were harvested and counted to prepare cell suspensions, according to the desired number of cells (50 cells/well for 4T1, 100 cells/well for MDA-MB-231, 1000 cells/well for MDA-MB-231 RR, MDA-MB-468 and MDA-MB-468 RR and 2000 cells/well for 4T1 RR). After 2mL of each cell suspension was seeded into the 6-well plates (one plate for each dose of IR - 0, 2, 4, 6, 8 Gy) and incubated for 24 hours at 37ºC with 5% CO_2. In the next day, the cells were exposed to the corresponding IR dose and left for 7-10 day until around 50 cells were observed, by light microscopy imaging, per colony in CTR (0 Gy) conditions.

3.4 Proliferation assay

Proliferation assay was developed using 48-well treated plates. Briefly, cells were harvested and counted to prepare cell suspensions, according to the desire number of cells ($2.5x10^3$ cells/well). After 500µL of each cell suspension was seeded into 48-well plates and incubated at 37ºC with 5% CO_2. At day 1, 2, 3, 4 and 7 the number of cells per well was determined. The well was washed

with PBS (phosphate buffered saline) and 0.2mL of accutase was placed for 20 minutes at 37ºC. Then, the cells were suspended in 50µL of PBS and stained with trypan blue to determine the number of viable and dead cells.

3.5 2D *in vitro* seeding and irradiation

2D *in vitro* assay was developed using 12-well treated plates. Briefly, cells were harvested and counted to prepare cell suspensions, according to the desired number of cells ($5x10^4$ cells/well). After, 1mL of each cell suspension was seeded in the 12-well treated plate and incubated at 37ºC with 5% CO_2. Medium was changed at day 3 after seeding and cells were exposed to an external X-Ray scheme of 5.2 Gy per fraction for five consecutive days (5x5.2 Gy), totalizing 26 Gy, simulating patients' short scheme (hypofractionated) treatment and analysed after 24 hours or 72 hours after.

3.6 Tumor spheroids formation

Tumor spheroids (TS) were developed using 81-wells agarose micromolds (3D Petri Dish®, by MicroTissues, Inc). Briefly, 2% (w/v) agarose (SeaKEM® LE Agarose, Lonza) in 0.9% (w/v) of sodium chloride solution was inserted in the micromolds and once solidified, transferred to 12-well non-treated plates, and hydrated with complete DMEM F12 for at least 2 hours. Simultaneous, cells were harvested and counted to prepare cell suspensions, according to the desired number of cells ($5x10^3$ cells/spheroid for MDA-MB-231, $2.5x10^3$ cells/spheroid for 4T1 and $1x10^3$ cells/spheroids for MDA-MB-468). After removing the medium from the molds, 190µL of each cell suspension was seeded in the mold and allowed to settle for 30 minutes at 37 ºC with 5% CO_2. Finally, 2mL of complete DMEM F12 medium was added to each plate well and incubated at 37 ºC with 5% CO_2. Medium was changed at day 3 after spheroids formation, before the first IR. (**Figure 9**)

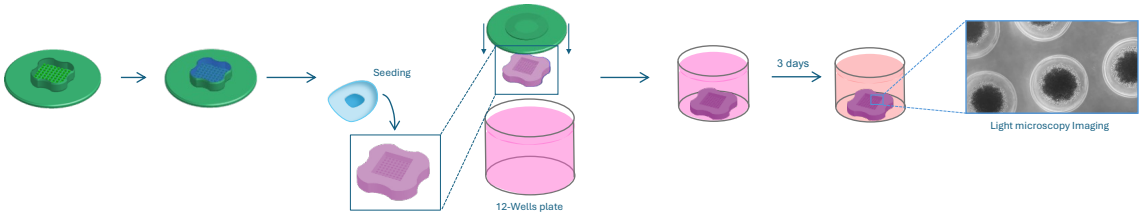


Figure 9 – Tumor Spheroids formation illustrative scheme.

Agarose molds were developed using 81-wells agarose micromolds (3D Petri Dish®, by MicroTissues, Inc). Cells of triple negative breast cancer (TNBC) cell lines were seeded within the molds and after 3 days assessed by light microscopy imaging.

3.7 Tumor spheroid and 2D *in vitro* morphological characterization

For 2D *in vitro* assay the cells were seeded in a T25 flask and when reached 80 of confluence morphometric analysis was performed. For 3D *in vitro* assay at specific time-points − 1, 3, 5, 7 and 10 days post-cell seeding − TS were monitored using brightfield microscopy (Leica Microsystems). Morphometric parameters, including area, diameter, circularity, aspect ratio (AR), roundness and solidity, were measured by manual segmentation using the ImageJ software.

3.8 Tumor spheroids irradiation

After 3 days of seeding, MDA-MB-231, MDA-MB-468 and 4T1 parental and RR spheroids were exposed to an external X-Ray scheme of 5.2 Gy per fraction for five consecutive days (5x5.2 Gy), totalizing 26 Gy, simulating patients' short scheme (hypofractionated) treatment and analysed 24 hours or 72 hours after (**Figure 10**). Both irradiated and control spheroids were transported and kept in culture at the Radiotherapy Service of IPO at 37ºC and 5% CO2. Photon beam was produced by a PRIMUS (Siemens, Malvern, PA, USA) linear particle accelerator. To guarantee a uniformed dosage and to avoid the build-up region of the 18 MV photon beam, 3 water plates were placed between the cell plate and the radiation source, while irradiating.

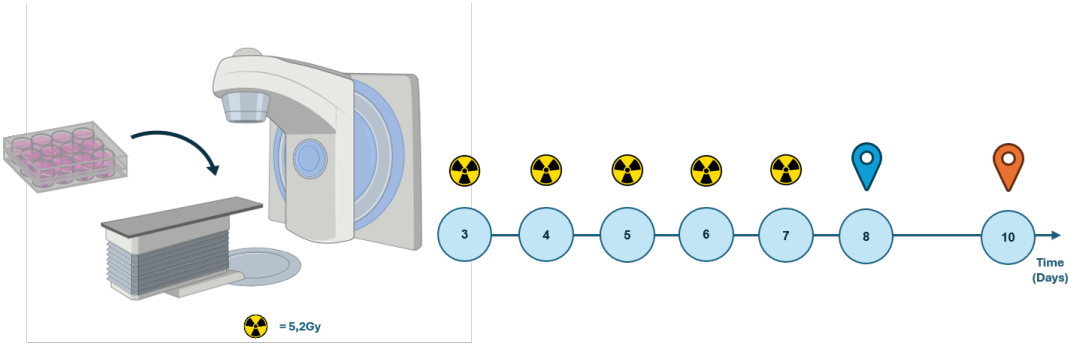


Figure 10 – Tumor spheroid irradiation scheme.

Tumor spheroids (TS) were irradiated 3 days after formation in a linear particle accelerator for 5 consecutive days (5x5.2 Gy) totalising 26 Gy of IR, a clinically relevant scheme for TNBC patients. (Created with BioRender.com)

3.9 Tumor spheroids metabolic activity

Briefly, culture medium was removed from the micro-molds, and spheroids were washed twice with PBS to remove remain residual extracellular ATP. Then, three spheroids were collected per condition and transferred into an opaque 96-well plate (SPL Life sciences). CellTiterGlo® 3D Reagent was added to each well in a proportion 1:1. Plates were shaken (200 rpm) for 5 minutes and then incubated for 25 minutes at room temperature, in the dark. Luminescence was immediately measured using a SynergyMXTM MultiMode Microplate Reader (BioTekTM). Analysis was performed using the mean luminescence values from three technical replicates for

each biological replicate, with a minimum of three independent experiments. To normalize ATP content to viable cell number, we collected 81 spheroids from an agarose mold and centrifugate at 1500rpm, 5 minutes, room temperature. Then, we washed the spheroids with PBS and after a centrifugation, we resuspended the spheroids in 0.3mL of accutase for 10 minutes at 37ºC. Then, we resuspend the cellular suspension, add 2mL of FACS buffer. After centrifugation, cells were resuspended and stained with trypan blue, and the number of viable and dead cells was quantified. These values were then used to normalize ATP levels per viable cell per spheroid.

3.10 Histological analysis

For hematoxylin and eosin staining, cell culture medium was removed, and molds were washed with PBS and kept in formol (Fisher Scientific) overnight at room temperature. After fixation, molds were washed with PBS and covered with 1.5% agarose solution. Once dried, samples were processed, embedded in paraffin using an automated embedding system (Thermo Scientific™ STP 120 Spin Tissue Processor) and sectioned into 3µm slices. The sections were deparaffinized in xylene, rehydrated through decreasing ethanol solutions, and stained with H&E: hematoxylin (Hematoxylin Gill 2) for 5 minutes, followed by eosin (Eosin-Y Alcoholic) for 4 minutes. The images were acquired using a brightfield microscope Leica DM2000 LED.

3.11 Transmission electron microscopy (TEM)

For ultrastructural analysis, spheroids were fixed overnight at 4 °C in a solution containing 2% formaldehyde and 2.5% glutaraldehyde in 0.1 M sodium cacodylate buffer. Spheroids were then washed with 0.1 M sodium cacodylate buffer, embedded in Histogel™, and post-fixed for 1 hour in 1% osmium tetroxide and 1.5% potassium ferrocyanide in 0.1 M sodium cacodylate buffer. Afterwards, samples were stained with aqueous 1% uranyl acetate for 30 minutes, dehydrated, and embedded in Embed-812 resin. Ultra-thin sections (70 nm thick) were cut using an RMC Ultramicrotome with Diatome diamond knives, mounted on 200 mesh copper grids, and stained with uranyless and 3% lead citrate for 5 minutes each. Imaging was done using a JEOL JEM 1400 transmission electron microscope, and digital images were captured with a PHURONA CCD camera. Transmission electron microscopy was performed at the HEMS core facility at i3S, University of Porto, Portugal. For each spheroid, three different layers were identified – periphery, middle and core – and five cells per each layer were imaged, at magnification 6000x and 8000x, for an overall overview, in a minimum of three independent experiments. Further images were acquired in different magnifications to allow the determination of cell area. Cancer cell organelles, including nucleus, mitochondria, lipid droplets, endoplasmic reticulum and autophagic vesicles, were manually quantified in higher magnifications (20000x) using ImageJ Software, and average values were calculated using GraphPad Prism.

3.12 Flow cytometry

MDA-MB-231, MDA-MB-468 and 4T1 parental and RR spheroids were collected 24 hours or 72 hours after the last IR fraction, washed with PBS and dissociated with accutase, for 10 to 60 minutes at 37 ºC, to allow the dissociation into single-cell suspensions. Cells were washed again with cold PBS, resuspended in FACS Buffer (PBS, 2% BSA, 0.01% sodium azide) containing appropriate conjugated antibodies, and stained in the dark for 30 minutes at 4°C. To evaluate viability, cells were incubated with Live/Dead (APC-Cy7) (eBioscienceTM) Fixable Viability Dye eFluorTM. Cells were then washed with FACS Buffer and fixed with paraformaldehyde 2% for 15 minutes at room temperature. Propidium iodide (PI) was added 5 minutes before acquisition in the cytometer. For lipid droplets staining, cells were previously washed with FACS buffer and incubated with the lipid droplets dye (PhenoVue 493 Lipid stain) for 20 minutes at 600 rpm, at 4℃, in the dark. For H2AX histone staining (BD Pharmingen™ PE Mouse Anti-H2AX (pS139)), cells were previously incubated with permeabilization/fixation buffer (BD Pharmingen™) for 20 minutes in the dark, at room temperature. Then, cells were washed with the permeabilization buffer and incubated with the anti-human H2AX (1:500) for 30 minutes in the dark, at room temperature. After additional washing steps, cells were acquired in a BD FACSCanto™ II cytometer and analyzed using FlowJo software v10.10.0.

3.13 Reactive oxidative species (ROS) analysis

To analyze reactive oxygen species (ROS) levels (OZ Biosciences ROS Detection Assay Kit), cells were previously washed with PBS and incubated with 2',7' –dichlorofluorescein diacetate (DCF) DA for 30 minutes in the dark, at room temperature. After washing steps, cells were acquired in a BD FACSCanto™ II cytometer and analyzed using FlowJo software v10.10.0.

3.14 EVs-depleted Media and EVs isolation

EVs were harvested from conditioned media (CM) of 30 molds of MDA-MB-231 spheroids cultured in EVs-depleted medium with 10% FBS and 1% P/S for 72 hours after the end of the RT scheme as mentioned in the Tumor Spheroids IR section. The EVs-depleted medium was developed by ultracentrifugation at 100 000g for 22 hours at 4ºC in an Optima™ XPN-100 ultracentrifuge (Beckman Coulter Life Sciences, Brea, CA, USA) with a 70Ti rotor.

In brief, for SEC isolation the CM was cleared of cell debris and large vesicles through centrifugation at 300g for 10 minutes at 4ºC followed by filtration using a 0.45µm filter. The medium collect was then concentrated using Centricon® Plus-70 centrifugal filter units (100 kDa molecular weight cutoff, MilliporeSigma/Merck, Burlington, MA, USA) by ultracentrifugation at

3500g for 45 minutes at 4ºC. Afterwards the samples obtained were passed through a sepharose column previously washed in 20mL of PBS and separated into eluates. The eluates fraction containing the EVs were after sequentially ultrafiltrated using Amicon® Ultra centrifugal filter units (10 kDa molecular weight cutoff (MWCO), MilliporeSigma/Merck, Burlington, MA, USA) at 3000g for 15minutes at 4ºC reaching 200µL of final volume (**Figure 11**).

For the differential ultracentrifugation (UC) the CM was cleared of cell debris and large vesicles through centrifugation at 300g for 10 minutes at 4ºC following by centrifugation at 2 000g for 20 minutes at 4ºC. Subsequently, the CM was filtered using a 0.45µm filter and ultracentrifuged at 100 000g for 4 hours at 4ºC in an Optima™ XPN-100 ultracentrifuge (Beckman Coulter Life Sciences, Brea, CA, USA) with a 70Ti rotor. The supernatant was discarded and the pellet obtained was washed with 25mL of PBS through UC at 100 000g for 2 hours at 4ºC in an Optima™ XPN-100 ultracentrifuge (Beckman Coulter Life Sciences, Brea, CA, USA) with a 70Ti rotor. Finally, the pellet was resuspended in 200µL of NaCl solution as previously reported (**Figure 11**).

Lastly for UC + Ultrafiltration (UF) the CM was initially cleared of cell debris and large vesicles through ultracentrifugation as abovementioned. The pellet obtained was resuspended in 1mL of NaCl. UF was then performed as said in the SEC technique using using Amicon® Ultra centrifugal filter units (10 kDa molecular weight cutoff (MWCO), MilliporeSigma/Merck, Burlington, MA, USA) at 3000g for 15 minutes at 4ºC until 200µL (**Figure 11**).

The protein content of the isolated EVs was determined using a Qubit™ (Thermo Fisher Scientific, MA, USA). To assess the concentration and size of EVs a dilution of 4uL of sample to 996uL of H2O (1:250) was performed and assessed in a Zetasizer Advance Ultra Red Label (Malvern Panalytical Ltd., Malvern, UK) operated using ZS Xplorer software, according to the manufacturer's instructions. For TEM analysis a drop of isolated EVs fraction diluted 1:5 in a HEPES Sucrose solution was placed on Formvar®-coated copper grid (150 mesh, Ted Pella Inc., Redding, CA). The dried grid containing EVs were stained with uranyless and 3% lead citrate for 5 minutes each. Imaging was done using a JEOL JEM 1400 transmission electron microscope, and digital images were captured with a PHURONA CCD camera. Transmission electron microscopy was performed at the HEMS core facility at i3S, University of Porto, Portugal. EVs were stored at -80ºC before use.

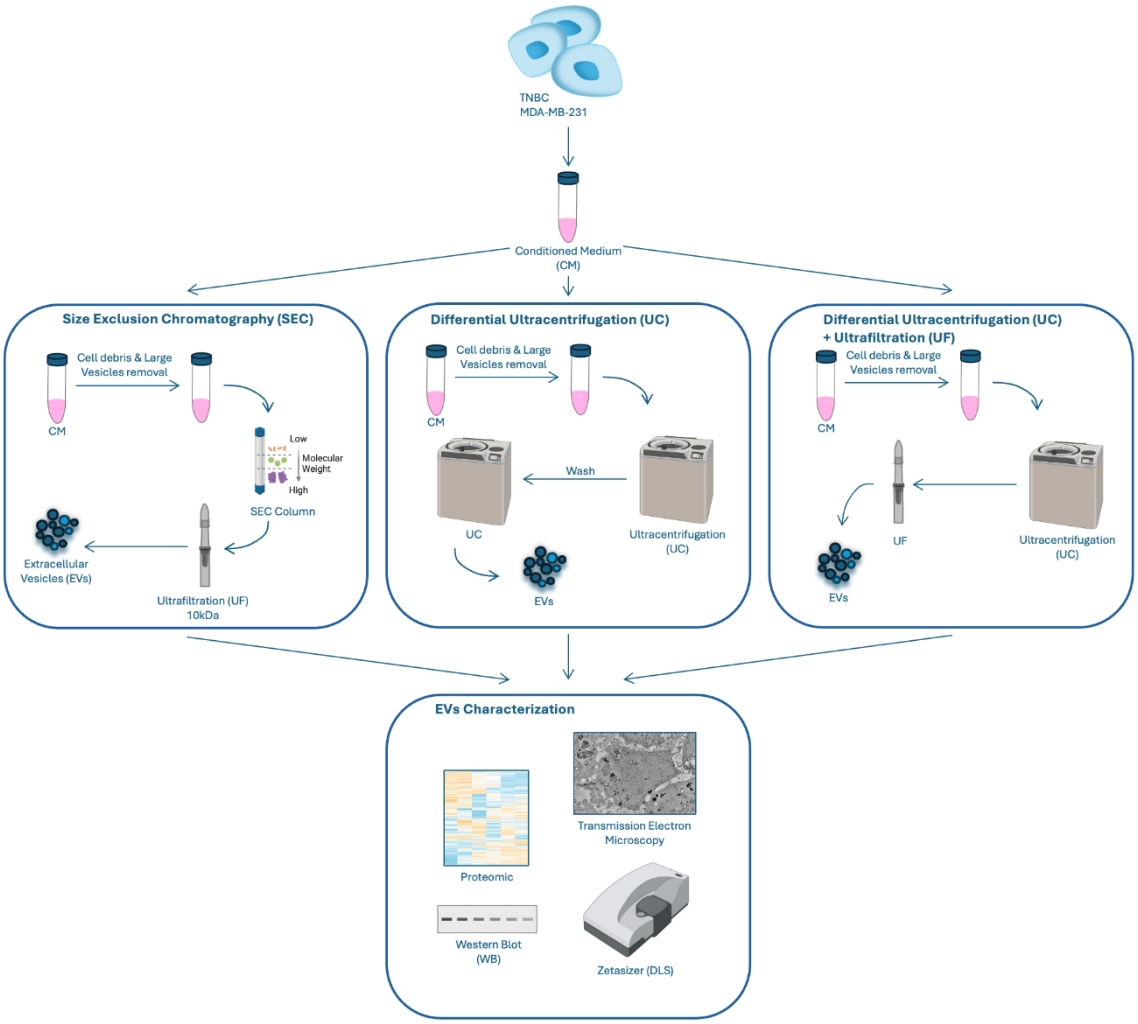


Figure 11 – Extracellular vesicles (EVs) isolation and characterization.

MDA-MB-231 tumor spheroids (TS) were exposed to 5 fractions of 5.2 Gy over 5 consecutive days (RT) or left without treatment (CTR), and after conditioned medium (CM) was collect 72 hours after the last irradiation (IR). EVs were isolated by three distinct methods: size exclusion chromatography (SEC), differential ultracentrifugation (UC) and UC + ultrafiltration (UC+UF) and characterized by transmission electron microscopy (TEM), zetasizer (Dynamic light scatter (DLS)), Western blot (WB) and proteomics. (Created with BioRender.com)

3.15 Western Blot

For western blot (WB) in a 10 or 15% SDS-PAGE gel a total of 20µg of protein was placed of EVs or cell lysates samples previously incubated for 10 minutes at 95ºC with laemmli buffer (1:4) (0.5 M Tris-HCL pH 6.8, 9.2g SDS, 40mL glycerol, 5% of β-mercaptoethanol, 5% bromophenol blue). Following electrophoresis, gels were transfer to Amersham™ Protran® Premium Western blotting membranes, nitrocellulose for western blotting. Membranes were blocked in 5% dry milk dissolved in PBS Tween 20 (0.1%) for 1 hour at room temperature, probed with antigen-specific antibodies overnight at 4ºC (**Table 2**) and washed with PBS Tween 20 (0.1%) five times. Afterwards, membranes were incubated with corresponding secondary antibodies for 1 hour at room temperature (**Table 2**) and washed with PBS Tween 20 (0.1%) five times. Blots were developed

with the clarity western ECL substrate (BioRAD) and protein band chemiluminescence was determined with autoradiographic films.

Table 2 – Antigen-specific and secondary antibodies used for western blot (WB).

Primary Antibody	REF	Dilution	Secondary Antibody	REF	Dilution
CD63	ExoAb	1:100	SBI goat Anti-Rabbit	ExoAb	1:2000
CD81	ExoAb	1:100	Anti-Rabbit	ExoAb	1:2000
FLOT1	sc-25506	1:200	Anti-Rabbit	NA934V	1:2000
ALIX	sc-53540	1:200	Anti-Mouse	NA931V	1:2000
Cytochrome C	sc-13560	1:200	Anti-Mouse	NA931V	1:2000
ANNEXIN V	sc-74438	1:200	Anti-Mouse	NA931V	1:2000
GRP78	sc-13539	1:200	Anti-Rat	sc-2006	1:2000

3.16 Proteomic analysis

RT and CTR TS were collected and washed seven times with cold PBS. Cell protein-extracts were obtained using a lysis buffer [50 mM Tris-HCl (pH 7.5), 150 mM NaCl, 2 mM EDTA and 1% Igepal], supplemented with a cocktail of proteases / phosphatases inhibitors, as previously described. Cells from 2D cultures were washed four times with cold PBS and lysed through incubation, along 20 minutes on ice, in lysis buffer. After, cell lysates were transferred to an Eppendorf with low binding protein properties. Protein extracts were obtained collecting the supernatant after centrifugation at 13 300 rpm for 10 minutes, at 4 °C. The protein concentration was determined with the Protein Assay Dye Reagent Concentrate (Bio-Rad. Hercules, CA, USA), following manufactures instructions. Protein lysates for cell lysates or EVs were stored at -80ºC until further use.

Proteomic analysis was performed at Proteomics core facility at i3S, University of Porto, Portugal.10mg of each sample was processed for proteomic analysis following the solid-phase-enhanced sample-preparation (SP3) protocol and enzymatically digested with trypsin/LysC as previously described. Protein identification and quantitation was performed by nanoLC-MS/MS equipped with a Field Asymmetric Ion Mobility Spectrometry - FAIMS interface. This equipment is composed of a Vanquish Neo liquid chromatography system coupled to an Eclipse Tribrid Quadrupole, Orbitrap, Ion Trap mass spectrometer (Thermo Scientific, San Jose, CA). 250 nanograms of peptides of each sample were loaded onto a trapping cartridge (PepMap Neo C18, 300 µm x 5 mm i.d., 174500, Thermo Scientific, Bremen, Germany). Next, the trap column was switched in-line to an Aurora Frontier XT 60 cm, 75µm (AUR3-60075C18-XT) chromatographic separation column. A 116 minutes separation was achieved by mixing A: 0.1% FA and B: 100%

ACN, 0.1% FA with the following gradient at a flow of 250nL/minute: 2 minutes (0% B to 4% B), 20 minutes (4% B to 12% B), 65 minutes (12% B to 28% B), 11 minutes (28% B to 45% B), 2 minutes (45% B to 85 % B) and 16 minutes at 99% B. Subsequently, the column was equilibrated with 0% B. Data acquisition was controlled by Xcalibur 4.7 and Tune 4.1.4244 software (Thermo Scientific, Bremen, Germany).

MS results were obtained following a Data Dependent Acquisition - DDA procedure. MS acquisition was performed with the Orbitrap detector at 120, 000 resolution in positive mode, quadrupole isolation, scan range (*m/z*) 375-1500, RF Lens 30%, standard AGC target, maximum injection time was set to auto, 1 microscan, data type profile and without source fragmentation. FAIMS mode: standard resolution, total carrier gas flow: static 4L/minutes, FAIMS CV: -45, -60 and -75 (cycle time, 1 s). Internal Mass calibration: Run-Start Easy-IC. Filters: MIPS, monoisotopic peak determination: peptide, charge state: 2-7, dynamic exclusion 30s, intensity threshold, $5.0e^3$. MS/MS data acquisition parameters: quadrupole isolation window 1.8 (m/z), activation type: HCD (30% CE), detector: ion trap, IT scan rate: rapid, mass range: normal, scan range mode: auto, normalized AGC target 100%, maximum injection time: 35 ms, data type centroid.

The raw data was processed using the Proteome Discoverer 3.1.1.93 software (Thermo Scientific) and searched against the UniProt database for the *Homo sapiens* reviewed proteome (2024_01 with 20,418 entries). A common protein contaminant list from MaxQuant was also included in the analysis. The MSPepSearch and Sequest HT and the search engines were used to identify tryptic peptides. The ion mass tolerance was 10 ppm for precursor ions and 0.5 Da for-fragment ions. The maximum allowed missing cleavage sites was set to two. Cysteine carbamidomethylation was defined as constant modification. Methionine oxidation, deamidation of glutamine and asparagine, peptide terminus glutamine to pyroglutamate, and protein N-terminus acetylation, Met-loss, and Met-loss+acetyl were defined as variable modifications. Peptide confidence was set to high. The processing node Percolator was enabled with the following settings: maximum delta Cn 0.05; target FDR (strict) was set to 0.01 and target FDR (relaxed) was set to 0.05, validation based on *q*-value. Protein label-free quantitation was performed with the Minora feature detector node at the processing step. Precursor ions quantification was performed at the consensus step with the following parameters: inclusion of unique plus razor peptides, precursor abundance based on intensity, and normalization based on total peptide amount. For hypothesis testing, protein ratio calculation was pairwise ratio-based and an t-test (background based) hypothesis test was performed. To increase the confidence level of quantified proteins, only those with at least 2 peptides used for quantification were considered for further comparative analysis. For differentially expressed proteins determination it was performed an analysis using the values provided for adjusted P-values and FC (fold change) determined by the Proteome Discoverer Software. Proteins were considered significantly different between samples when fold-change was equal to or greater than 1.5, at a significance level of 0.05.

Data were analysed with different bioinformatics tools. Enrichment analysis for the gene ontology categories was performed using Cluster profiler package[57] on R Statistical Software (v4.4.1; R Core Team 2024), using the whole human genome as a reference.

3.17 Statistical analysis

Statistical analysis and graphical representation of the data were performed using GraphPad Prism 9.0.1 software (GraphPad Software Inc.). At least three independent experiments were conducted for each experiment. All data sets were challenged by a normality test (Shapiro-Wilk test or D'Agostino Pearson omnibus, depending on the sample data size). Comparisons between CTR and RT groups for the same cell line were analysed with paired *Student's t*-tests when Gaussian distribution was assumed and unpaired t-test for parental and RR cell lines comparison. Datasets that did not pass the normality test were analysed by Wilcoxon matched-pairs signed rank test or by Mann-Whitney. Comparisons between two independent variables were analysed with two-way ANOVA, followed by Sidak's multiple comparisons test. The level of significance was set at $*p < 0.05$, $**p < 0.01$, $***p < 0.001$ and $****p < 0.0001$. All data are presented as mean ± standard deviation (SD).

4. Results

4.1 Establishment and characterization of human and mouse syngeneic radioresistant TNBC models

RT exerts its antitumor effects by inducing DNA damage, including single- and double-strand breaks, which can trigger genomic instability, mitotic catastrophe, senescence, or apoptosis if left unrepaired.[25,36] However, cancer cells can adapt to radiation-induced stress by activating DNA damage response (DDR) pathways, enhancing DNA repair mechanisms or inhibiting DNA damage sensitivity, thereby promoting survival following irradiation.[25] Indeed, the upregulation of DNA damage repair mechanisms is widely recognized as one of the principal mechanisms underlying acquired radioresistance. Although advanced and metastatic TNBC are particularly prone to develop resistance to RT compared with other breast cancer subtypes, the molecular mechanisms behind this phenotype remain poorly understood.

4.1.1 – Radioresistant cell lines show significant morphological and phenotypical changes

To tackle the mechanisms behind TNBC radioresistance, we developed RR cell lines from different molecular subtypes of TNBC.[58] Parental cell lines (MDA-MB-231, MDA-MB-468 and 4T1) were consecutively exposed to weekly increasing doses of RT totalising 50 Gy over the course of a month and a half (**Figure 12**).

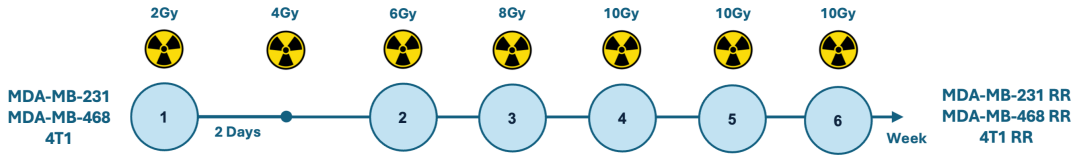


Figure 12 - Establishment of radioresistant cell lines from two triple negative breast cancer subtypes.

MDA-MB-231, MDA-MB-468 and 4T1 cell lines were exposed to a total of 50 Gy over the course of a month and a half to develop radioresistant (RR) cell lines from the respective parental ones. An initial dose of 2 Gy was followed by weekly incremental doses of 2 Gy, followed by 3 doses of 10 Gy, totalizing a radiation dose of 50 Gy.

MDA-MB-231 RR cell line showed a smaller area and an increase elongation profile associated with lower solidity, circularity, roundness and increased aspect ratio (AR) in comparison with the parental cell line (**Figure 13A-G**). In contrast, MDA-MB-468 RR cell line showed increase size, solidity, circularity and roundness while the AR was decreased (**Figure 14A-G**). Interestingly, the mouse 4T1 RR cell line showed a similar profile to the MDA-MB-231 RR with decreased solidity, circularity and roundness and increased AR (**Figure 15A-G**). The elongated profile evidenced in the MDA-MB-231 and 4T1 RR cells is associated with evident protrusions observed by brightfield imaging, suggesting a more mesenchymal and aggressive profile.

Next, we assessed the proliferative capacity of the RR cell lines by determining their doubling time. All RR cell lines exhibited a significantly reduced proliferation rate compared with their respective parental cell lines. Among them, the MDA-MB-468 RR and 4T1 RR cell lines displayed the longest doubling times, indicating the lowest proliferative capacity (**Figure 13H, Figure 14H and Figure 15H**).

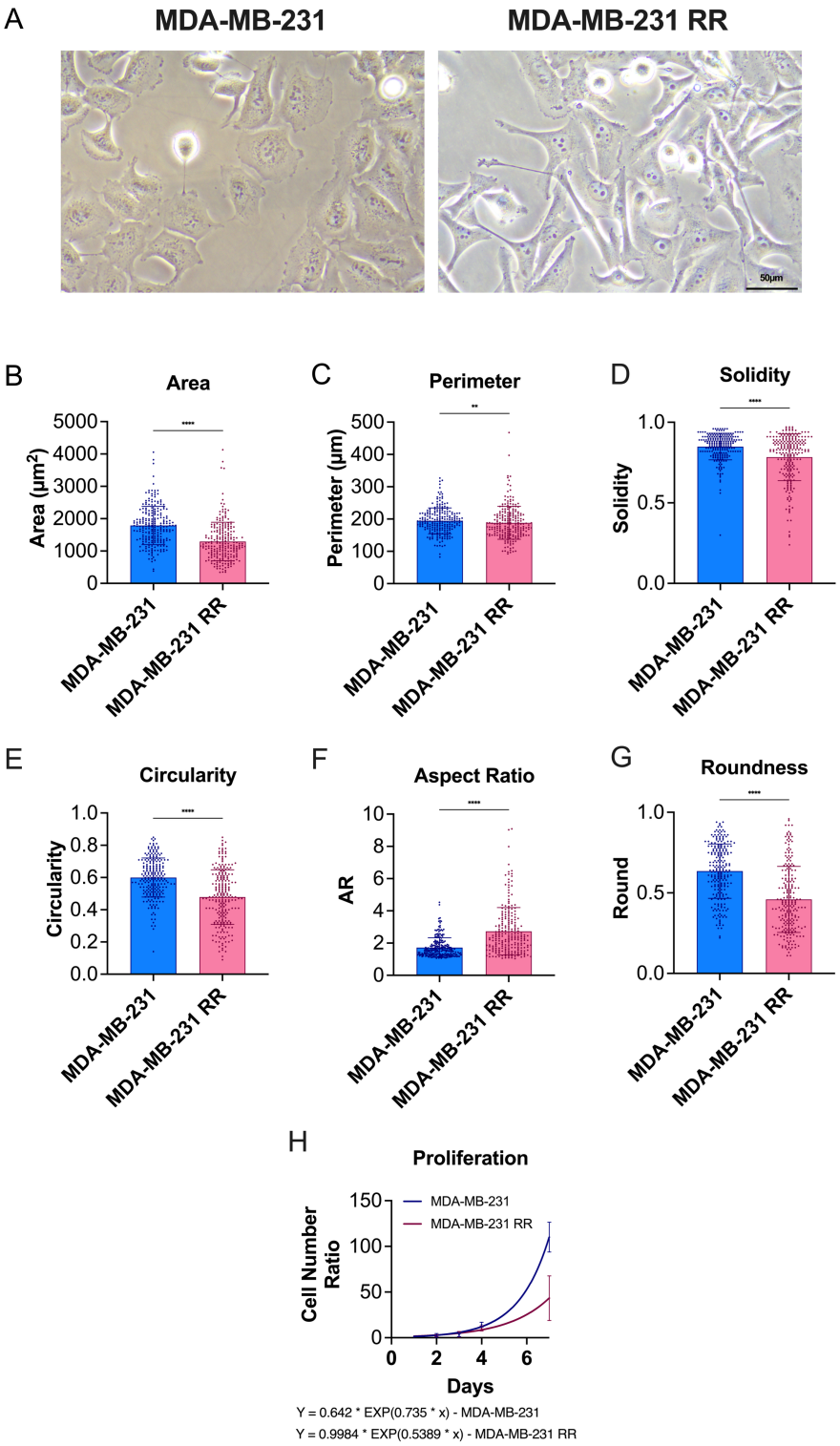


Figure 13 – MDA-MB-231 radioresistant cell line shows smaller size and increased elongation in comparison with the parental MDA-MB-231 cell line.

MDA-MB-231 and MDA-MB-231 radioresistant (RR) cell lines were cultured until reaching a confluence around 80 and analysed after. (**A**) Brightfield images obtained for MDA-MB-231 and MDA-MB-231 RR cell lines. Scale represents 50µm. (B) Cell Area (µm^2), (**C**) perimeter (µm), (**D**) solidity, (**E**) circularity. (**F**) aspect ratio (AR) and (**G**) roundness of MDA-MB-231 and MDA-MB-231 RR cell lines. (**H**) Ratio of number of cells assessment for a full week to determine proliferation rate. Data are representative of at least 3 independent experiments. All comparisons were performed using unpaired t-test (B-G) and exponential (Malthusian) growth (H) (*p < 0.05, **p < 0.01, ***p > 0.001, ****p < 0.0001).

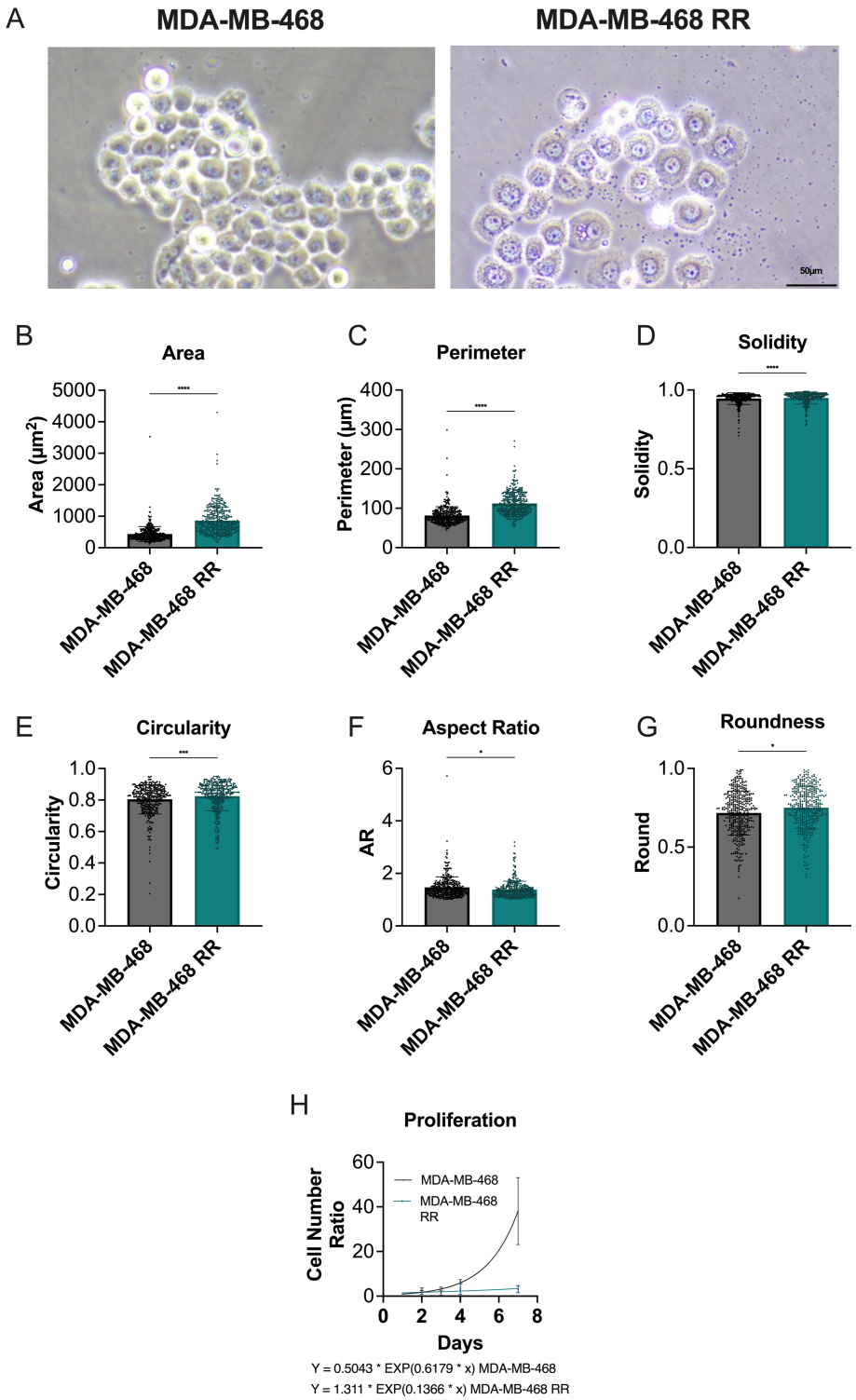


Figure 14 – MDA-MB-468 radioresistant cell line shows significant increase size and roundness in comparison with the parental MDA-MB-468 cell line.

MDA-MB-468 and MDA-MB-468 radioresistant (RR) cell lines were cultured until reaching a confluence around 80 and analysed after. (**A**) Brightfield images obtained for MDA-MB-468 and MDA-MB-468 RR cell lines. Scale represents 50µm. (**B**) Cell Area (µm2), (**C**) perimeter (µm), (**D**) solidity, (**E**) circularity. (**F**) aspect ratio (AR) and (**G**) roundness of MDA-MB-468 and MDA-MB-468 RR cell lines. (**H**) Ratio of number of cells assessment for a full week to determine proliferation rate. Data are representative of at least 3 independent experiments. All comparisons were performed using unpaired t-test (B-G) and exponential (Malthusian) growth (H) (*p < 0.05, **p < 0.01, ***p > 0.001, ****p < 0.0001).

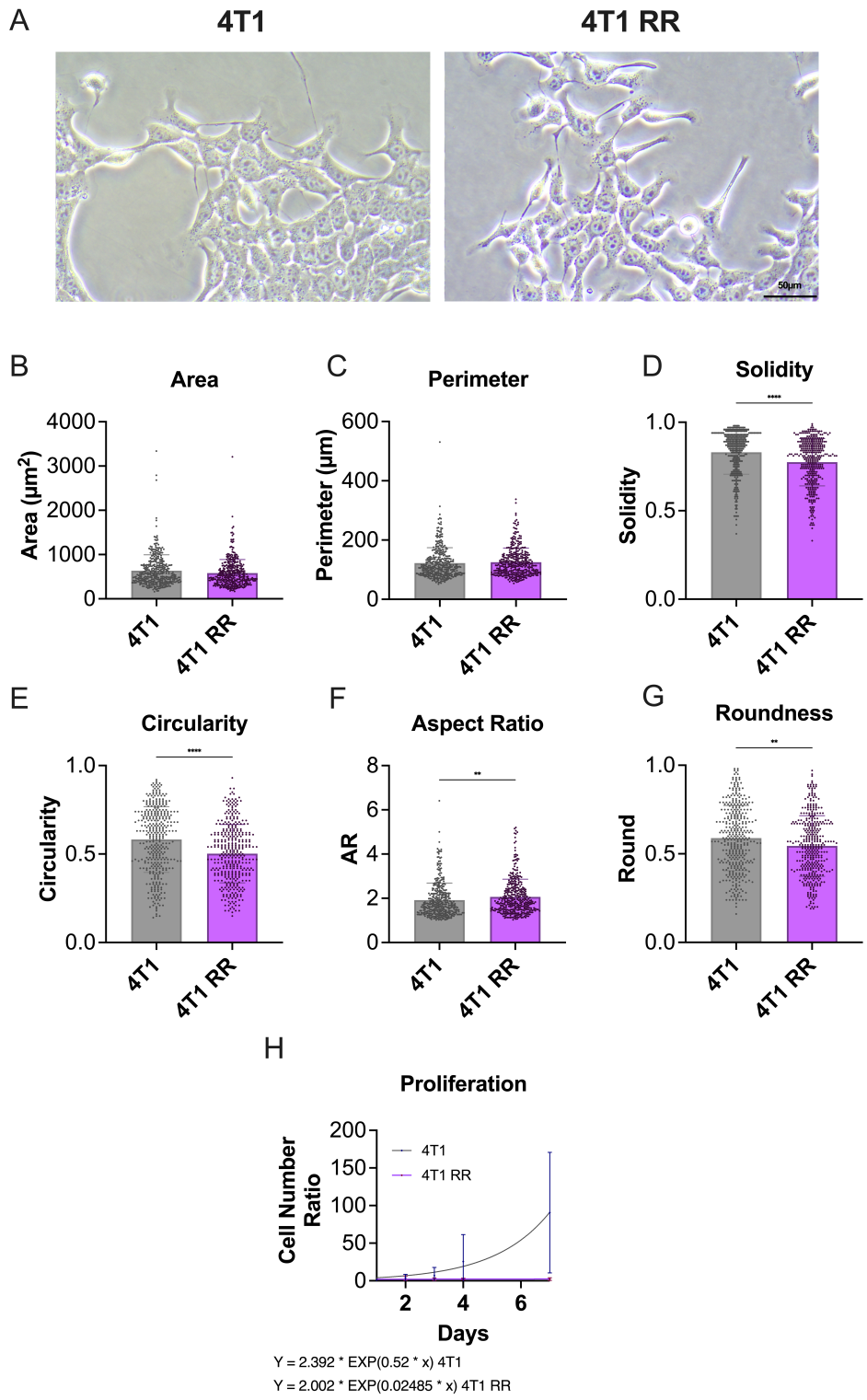


Figure 15 – 4T1 radioresistant cell line shows significant elongation in comparison with the parental 4T1 cell line.

4T1 and 4T1 radioresistant (RR) cell lines were cultured until reaching a confluence around 80 and analysed after. (**A**) Brightfield images obtained for 4T1 and 4T1 RR cell lines. Scale represents 50µm. (**B**) Cell Area (µm2), (**C**) perimeter (µm), (**D**) solidity, (**E**) circularity. (**F**) aspect ratio (AR) and (**G**) roundness of 4T1 and 4T1 RR cell lines. (**H**) Ratio of number of cells assessment for a full week to determine proliferation rate. Data are representative of at least 3 independent experiments. All comparisons were performed using unpaired t-test (B-G) and exponential (Malthusian) growth (H) (*p < 0.05, **p < 0.01, ***p > 0.001, ****p < 0.0001).

4.1.2 – Establishment of 4T1 Tumor spheroids for radiobiology studies

Given the value of 3D models for radiobiology research, our lab has previously developed tumor spheroid (TS) models using the human MDA-MB-231[49] and MDA-MB-468 cell lines. However, a corresponding mouse model suitable for studying RT response in *in vivo* immunocompetent setting was still lacking. To address this gap, we established a TS model using the murine TNBC cell line 4T1. This model expands our portfolio of biomimetic TS models and provides a valuable platform for investigating RT response in a preclinical context, facilitating future studies in immunocompetent mouse models.

To develop the 4T1 TS model, we started by testing different culture media, namely, RPMI, DMEM F12, DMEM Low and DMEM High as well as different cell-seeding numbers, 2500, 5000 and 10 000 cells per spheroid. Brightfield microscopy and H&E, as well as morphometric analysis, revealed that the different media had a distinct impact on spheroids morphology and morphometric parameters (**Figure 16A, B**). We observed that 4T1 TS cultured in DMEM Low displayed large necrotic cores, particularly when seeded with 10 000 cells. In contrast, 4T1 TS, cultured in DMEM F12 formed the smallest spheroids with the lowest circularity and solidity (**Figure 16A, B**). No differences were observed in the number and percentage of viable cells however, 4T1 TS cultured either with DMEM High or DMEM Low seemed to have the higher metabolic activity, especially with 10 000 cells/spheroid. (**Figure 16C-F**). Based on these results, 2500 cells/spheroid cultured in DMEM/F12 medium conditions were selected for the subsequent experiments due to their increased compactness, high viability and intermediate ATP levels.

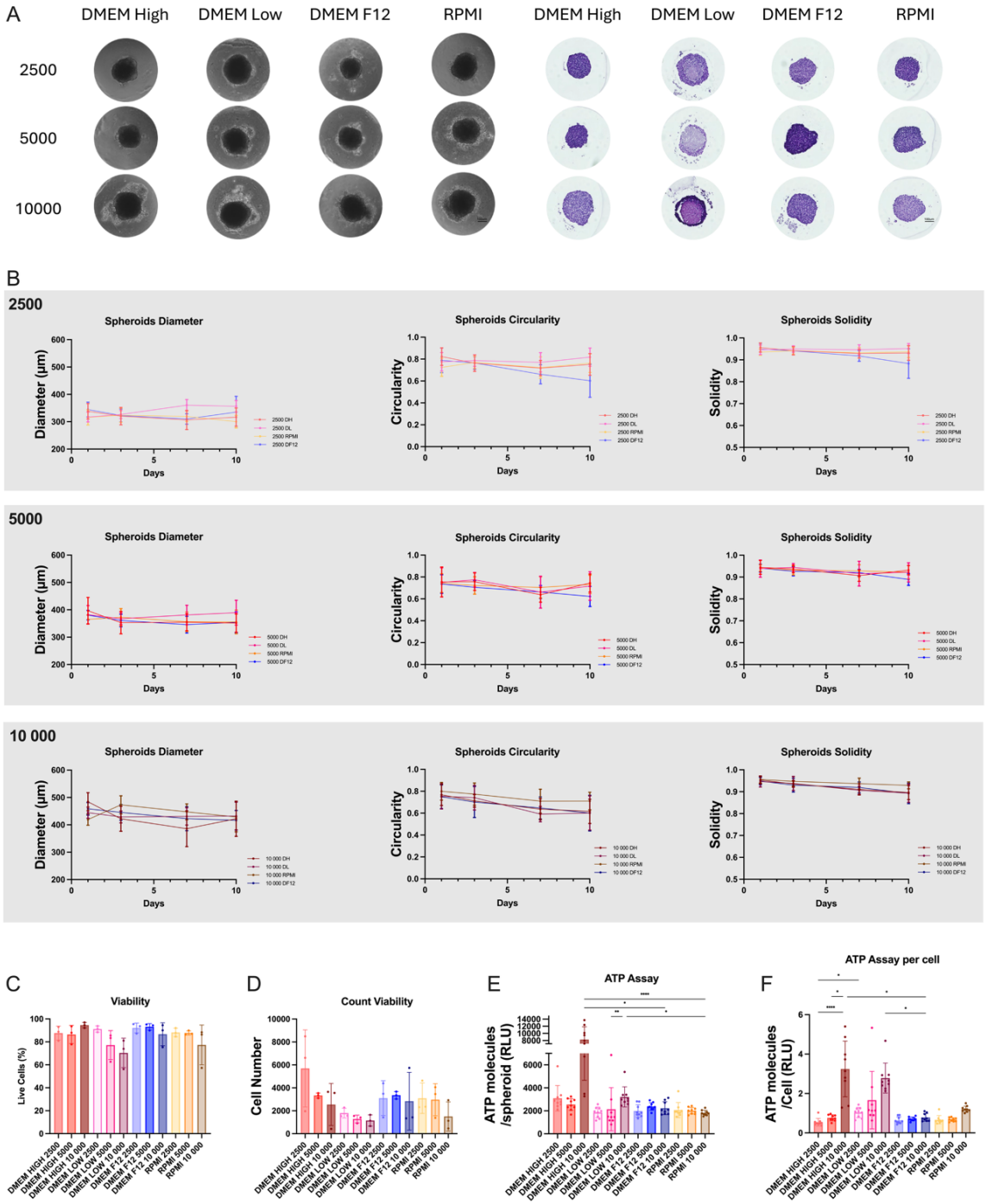


Figure 16 – Characterization of culture media impact on 4T1 tumor spheroids, seeded with three different cell densities, over ten days of culture.

(**A**) Images of brightfield microscopy and H&E staining of tumor spheroids (TS) established with different media (RPMI, DMEM F12, DMEM Low Glucose (Low) and DMEM High Glucose (High)) and densities (2500, 5000 and 10 000) after 10 days post-seeding. Scale represents 100µm. (**B**) Spheroids diameter, circularity and solidity were determined in the different media and densities (2500 cells, 5000 cells and 10000 cells) along time (day 1, 3, 5, 7 and 10), through the analysis of five brightfield microscopy images per experiment, using the ImageJ software. (**C**) Viability (% of live cells), (**D**) count of viable cell number per spheroid were determined through Flow cytometry after 10 days of culture. Metabolic activity was determined through quantification of intracellular ATP molecules (**E**) per spheroid and (**F**) per cell after 10 days of culture. Data are representative of at least 3 independent experiments. All comparisons were performed using the two-way ANOVA (*p<0.05, **p<0.01, ***p>0.001, ****p<0.0001).

4.1.3 – Irradiation elicits distinct morphological and phenotypic responses in 2D versus 3D tumor models

We next evaluated the RR phenotype acquisition and characterized the response to RT of all established cell lines by exposing both 2D cultures and 3D spheroids to a clinically relevant hypofractionated RT scheme (5x5.2 Gy). Non-irradiated conditions (CTR) were used as experimental controls. Cellular responses were assessed at an early (24 hours) and a late (72 hours) time-point following completion of irradiation.

To confirm the acquisition of a RR phenotype, a colony formation assay was performed for MDA-MB-231 cell lines. MDA-MB-231 RR cells demonstrated a higher capacity to survive and proliferate under cumulative IR doses in comparison with their parental counterparts, specially under 6 and 8Gy, confirming their enhanced resistance to ionizing radiation (**Figure 17A-C**). To further characterize the mechanisms underlying the enhanced survival of the MDA-MB-231 RR cell line, we exposed these cells to a RT regimen consisting of five fractions of 5.2 Gy delivered over one week in a 2D culture system. Interestingly, at 24 hours post-irradiation, MDA-MB-231 RR cells showed a significant decrease in cell viability upon RT (**Figure 17D, E**). However, by 72 hours, no apparent impact in viability was observed suggesting a possibly recover from the RT-induced damage. Additionally, a progressive increase in γ-H2AX associated with loss of viability in the parental cells suggests persistent activation of the DNA damage response following irradiation. In contrast, the absence of further γ-H2AX accumulation upon RT in the RR cells is consistent with a reduced accumulation of DNA damage or a more efficient resolution of radiation-induced damage (**Figure 17D-I**).

In a 3D *in vitro* setting, brightfield microscopy together with morphometric analysis revealed distinct responses to RT between parental and RR spheroids. MDA-MB-231 RR spheroids were consistently smaller than their parental counterparts under CTR conditions. Following IR, MDA-MB-231 spheroids exhibited an increase in diameter, circularity and compactness at 72 hours post-RT. In contrast, MDA-MB-231 RR spheroids largely preserved their morphology, maintaining their circularity and solidity, while an increase in spheroid diameter was only observed at 72 hours after RT (**Figure 18A, B**). At 24 hours after RT, no significant reduction in the viability of MDA-MB-231 RR spheroids was detected, while parental MDA-MB-231 spheroids exhibited a significant decrease in viability (**Figure 18C, D)**, accompanied by an increase in γ-H2AX expression (**Figure 18E, F).** By 72 hours post-irradiation, the effects of RT became more pronounced in the parental MDA-MB-231 spheroids, which showed a reduction in viable cells together with an increased expression of the γ-H2AX and ATP molecules/per cell. In contrast, although MDA-MB-231 RR spheroids exhibited a modest reduction in viability at 72 hours compared with 24 hours, they remained significantly more viable than the parental spheroids and showing no evident increase in γH2AX+ cells following irradiation, between both time-points.

Notably, RT also induced an increase in metabolic activity per viable cell in the RR spheroids (**Figure 18C - J**).

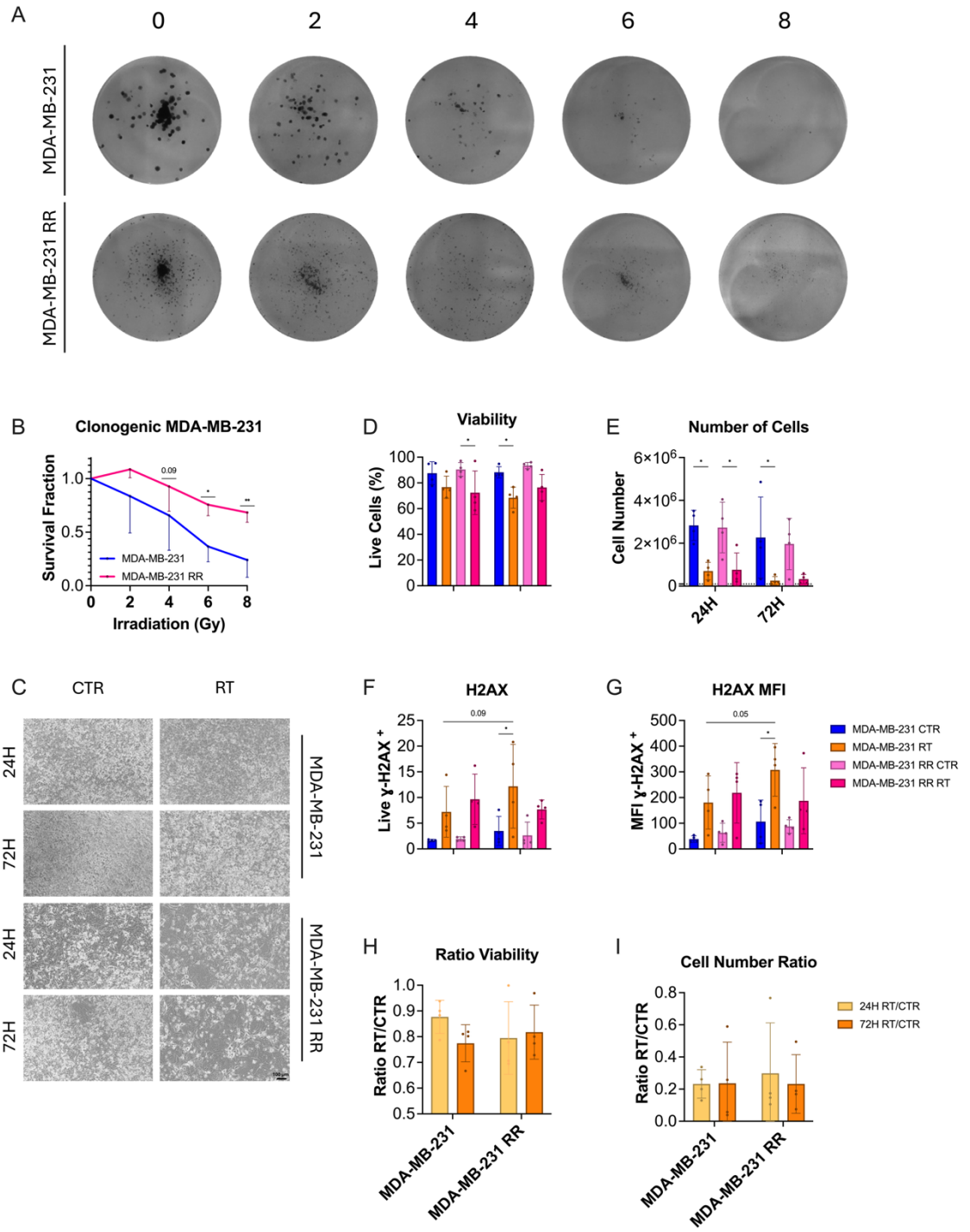


Figure 17 - Hypofractionated radiotherapy differently impacts cell survival and γ-H2AX expression in parental and radioresistant MDA-MB-231 cells.

MDA-MB-231 and MDA-MB-231 radioresistant (RR) cell lines were exposed to 5 fractions of 5.2 Gy over 5 consecutive days (RT) or left without treatment (CTR) and analysed 24 hours and 72 hours after the last irradiation (IR). (**A**) Clonogenic assay images and (**B**) colony formation performed along increasing doses of IR (0, 2, 4, 6, 8Gy). (**C**) Brightfield images of MDA-MB-231 and MDA-MB-231 RR cells 24 hours and 72 hours after IR in CTR and RT conditions. Scale represents

100µm. (**D**) Viability (% viable cells) and (**E**) number of viable cells determined through flow cytometry by live/dead staining. (**F**) Live cells $^{+}$ γ-H2AX histone (pS139) and (**G**) Median fluorescence intensity (MFI) of γ-H2AX histone (pS139), determined through flow cytometry. (**H**) Ratio of viability (% RT/CTR) and (**I**) ratio of number of cells (RT/CTR) after 24 hours or 72 hours post-IR. Data are representative of at least 3 independent experiments. All comparisons were performed using two-way ANOVA (A, C-H) (*p < 0.05, **p < 0.01, ***p > 0.001, ****p < 0.0001).

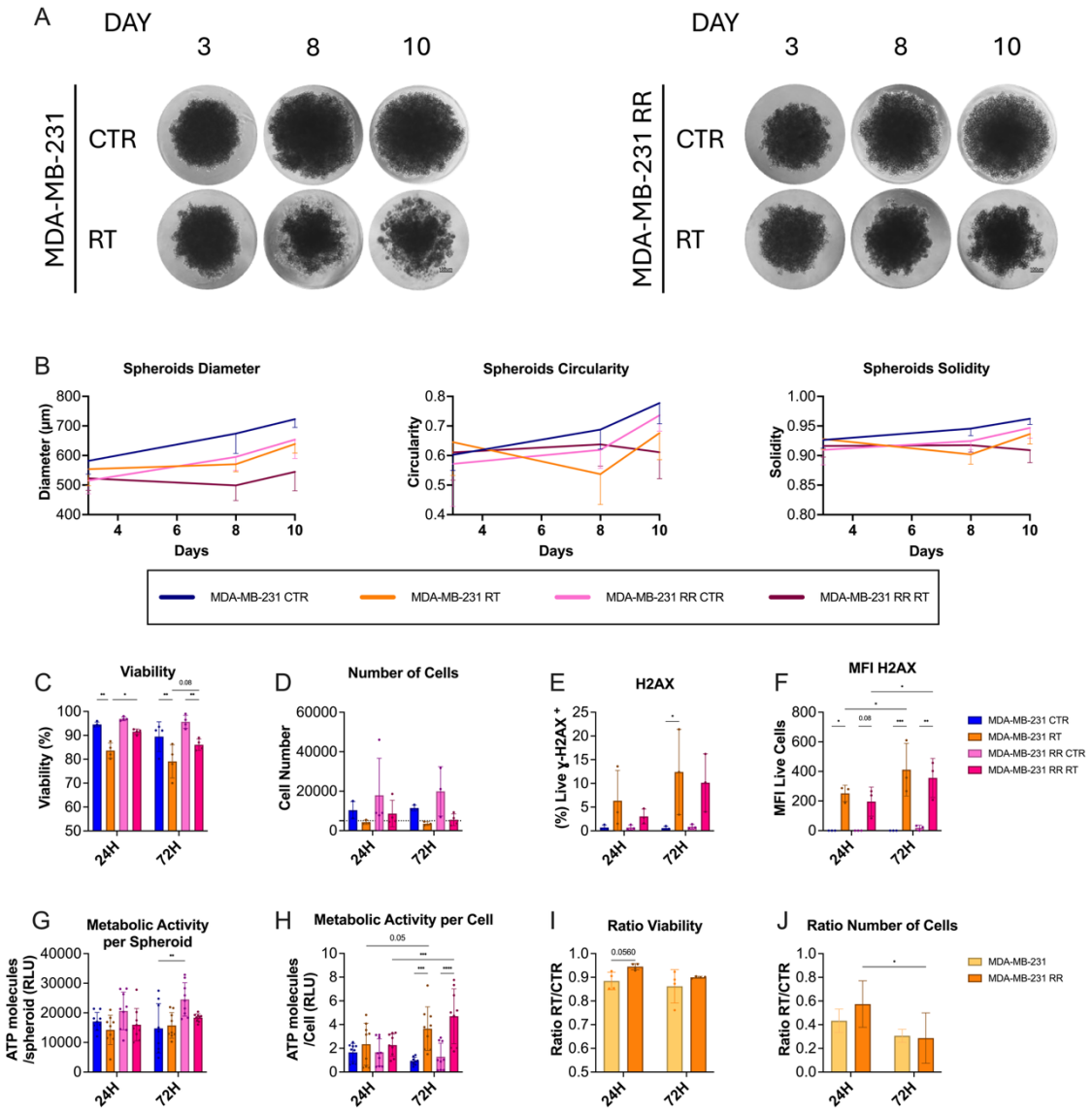


Figure 18 - Hypofractionated radiotherapy has a distinct impact on parental and radioresistant MDA-MB-231 breast tumor spheroids.

Tumor spheroids (TS) were exposed to 5 fractions of 5.2 Gy over 5 consecutive days (RT) or left without treatment (CTR) and analysed 24 hours and 72 hours after the last irradiation (IR). (**A**) Brightfield images of MDA-MB-231 and MDA-MB-231 RR TS (Day 3, 7 and 10) in CTR and RT conditions. Scale represents 100µm. (**B**) Spheroids diameter, circularity and solidity were determined along time (day 3, 8 and 10) in CTR and RT conditions, through the analysis of five brightfield microscopy images per experiment, using the ImageJ software. (**C**) TS viability (% viable cells) and (**D**) number of viable cells per spheroid determined through flow cytometry by live/dead staining. (**E**) Live cells $^{+}$ γ-H2AX histone (pS139) and (**F**) Median fluorescence intensity (MFI) of γ-H2AX histone (pS139), determined through flow cytometry. Intracellular ATP molecules analysis (**G**) per spheroid and (**H**) per live cell of TS through CellTiter-Glo assay (relative light unit (RLU)) (**I**) Ratio of TS viability (% RT/CTR) and (**J**) ratio of number of cells per spheroid (RT/CTR). Data are representative of at least 3 independent experiments. All comparisons were performed using two-way ANOVA (B-J) (*p < 0.05, **p < 0.01, ***p > 0.001, ****p < 0.0001).

Considering the molecular heterogeneity of TNBC, we next evaluated the effects of hypofractionated RT in an additional human (MDA-MB-468) and murine (4T1) TNBC models using both 2D cultures and 3D spheroids. Clonogenic assays revealed that both the MDA-MB-468 RR and 4T1 RR cell lines exhibited a greater capacity to survive and proliferate following cumulative doses of ionizing radiation compared with their respective parental cell lines. Specifically, MDA-MB-468 RR cells showed increased clonogenic survival at 6 and 8 Gy (**Figure 19A)** and 4T1 RR cells displayed enhanced survival at 2, 4, and 6 Gy (**Figure 20A**).

Unlike the MDA-MB-231 RR cells, neither MDA-MB-468 RR nor 4T1 RR cell lines exhibited a significant reduction in viability 24 hours after irradiation (**Figure 19 B and Figure 20B**). As previously observed for the MDA-MB-231 model, the effects of irradiation were more pronounced 72 hours after RT. At this time-point, both MDA-MB-468 and 4T1 RR cells demonstrated a significant decrease in the viability. As expected, parental cell lines of both RR cell lines showed a significantly greater decrease in survival, confirming the acquisition of a radioresistant phenotype in both models. Interestingly, despite their higher survival rates, MDA-MB-468 RR and 4T1 RR cell lines displayed higher γ-H2AX expression following RT than their parental counterparts, indicating a sustained activation of the DNA damage response despite their increased resistance to irradiation (**Figure 19B-G, Figure 20B-G**).

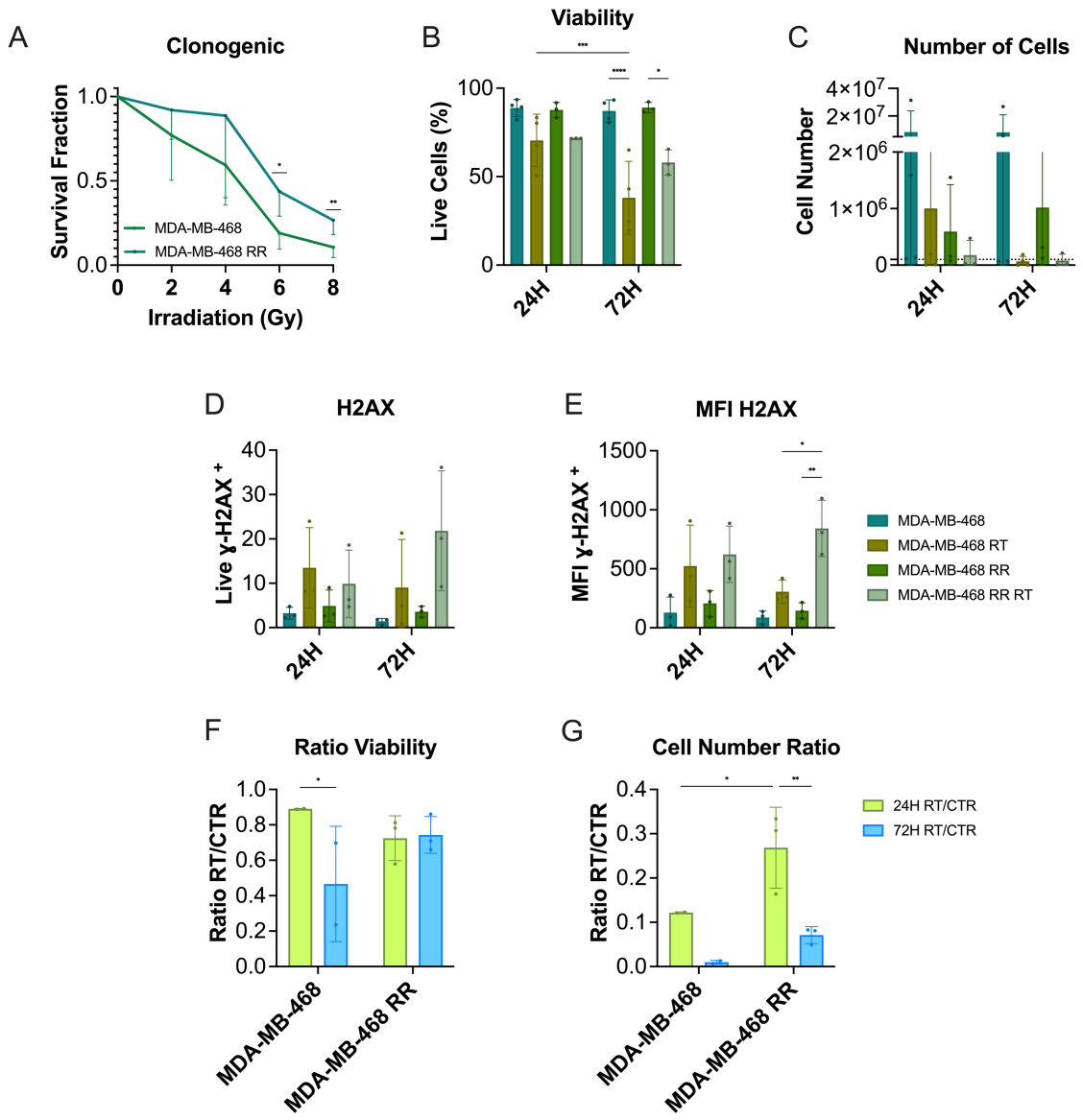


Figure 19 - Hypofractionated radiotherapy differently impacts cell survival and γ-H2AX expression in parental and resistant MDA-MB-468 cells.

MDA-MB-468 and MDA-MB-468 RR cell lines were exposed to 5 fractions of 5.2 Gy over 5 consecutive days (RT) or left without treatment (CTR) and analysed 24 hours and 72 hours after the last irradiation (IR). (**A**) Clonogenic assay performed along increasing doses of IR (0, 2, 4, 6, 8Gy). (**B**) Viability (% viable cells) and (**C**) number of viable cells determined through flow cytometry by live/dead staining. (**D**) Live cells $^{+}$γ-H2AX histone (pS139) and (**E**) Median fluorescence intensity (MFI) of γ-H2AX histone (pS139), determined through flow cytometry. (**F**) Ratio of TS viability (% RT/CTR) and (**G**) ratio of number of cells (RT/CTR) after 24 hours or 72 hours post-IR. Data are representative of at least 3 independent experiments. All comparisons were performed using two-way ANOVA (A, C-H) (*p < 0.05, **p < 0.01, ***p > 0.001, ****p < 0.0001).

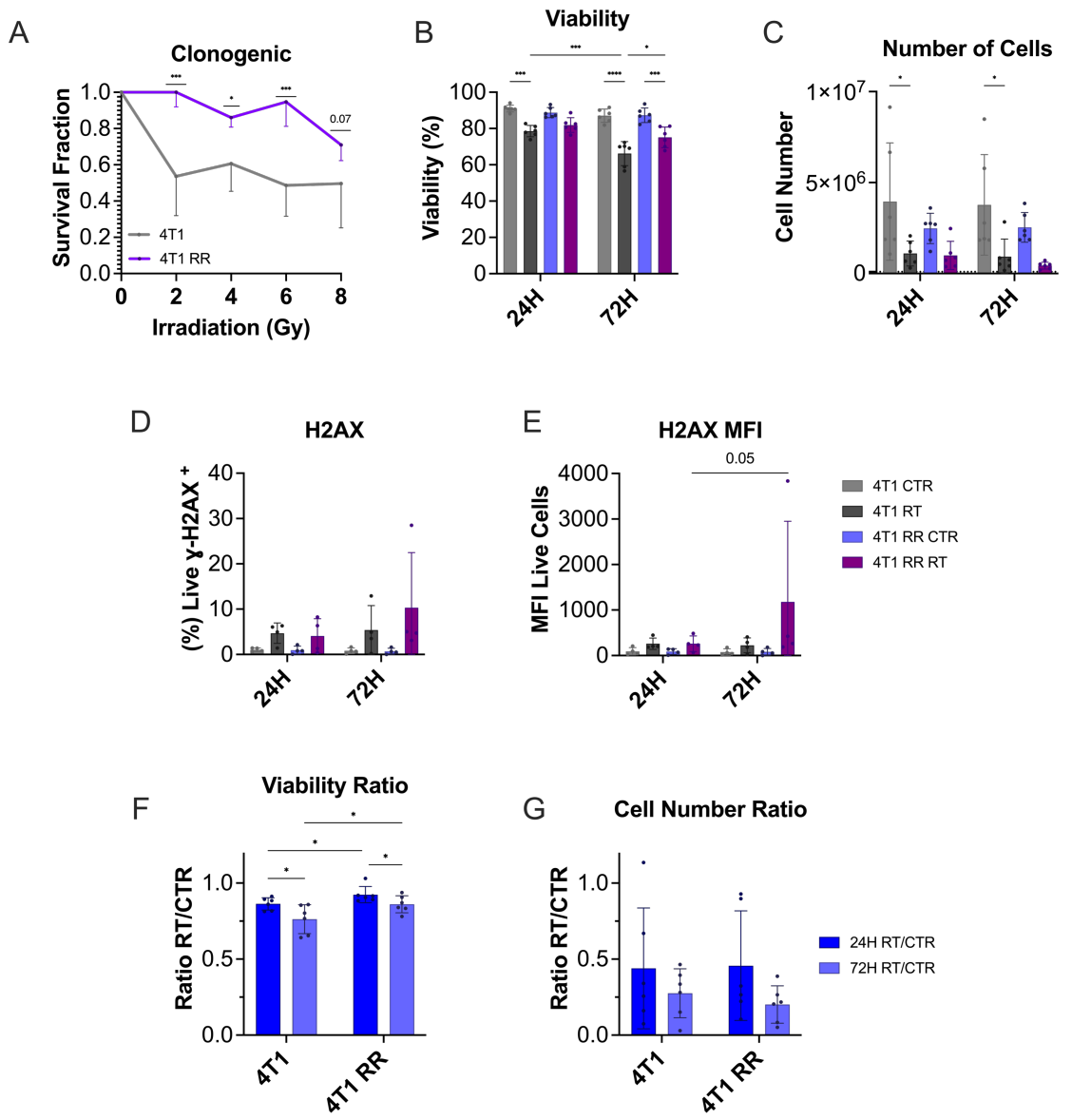


Figure 20 - Hypofractionated radiotherapy induces different survival and DNA damage repair between 4T1 and 4T1 RR cells.

4T1 AND 4T1 RR cell lines were exposed to 5 fractions of 5.2 Gy over 5 consecutive days (RT) or left without treatment (CTR), and analysed 24 h and 72h after the last irradiation (IR). (**A**) Clonogenic assay performed along increasing doses of IR (0, 2, 4, 6, 8Gy). (**B**) Viability (% viable cells) and (**C**) number of viable cells determined through flow cytometry by live/dead staining. (**D**) Live cells $^{+}$γ-H2AX histone (pS139) and (**E**) Median fluorescence intensity (MFI) of γ-H2AX histone (pS139), determined through flow cytometry. (**F**) Ratio of TS viability (% RT/CTR) and (**G**) ratio of number of cells (RT/CTR) after 24h or 72h post-IR. Data are representative of at least 3 independent experiments. All comparisons were performed using two-way ANOVA (A, C-H) (*p < 0.05, **p < 0.01, ***p > 0.001, ****p < 0.0001).

We next evaluated the effects of hypofractionated RT in the corresponding 3D spheroid models. RT had a distinct impact on spheroids morphology and morphometric parameters across the different cell lines. Under non-irradiated conditions (CTR), MDA-MB-468 RR spheroids were smaller spheroids than their parental counterparts, while 4T1 RR spheroids exhibited a larger diameter than the parental 4T1 spheroids. These baseline differences were accompanied by distinct responses to irradiation. Following RT, MDA-MB-468 RR spheroids displayed a reduction

in spheroid diameter together with increased circularity and solidity, in contrast to the parental MDA-MB-468 spheroids. Conversely, 4T1 RR and 4T1 spheroids maintained stable circularity and solidity following irradiation, while exhibiting a reduction in spheroid diameter (**Figure 21A, B and Figure 22 A, B**). At both 24 and 72 hours after RT, MDA-MB-468 RR spheroids exhibited higher viability than parental MDA-MB-468 spheroids. Furthermore, irradiation did not significantly affect the number of viable cells per spheroid in the MDA-MB-468 RR model. Interestingly, despite their higher viability, irradiated MDA-MB-468 RR spheroids presented a higher expression of γ-H2AX and a lower metabolic activity per spheroid compared with the irradiated parental spheroids (**Figure 21C-G**). However, when metabolic activity was normalized to the number of viable cells, no significant differences were observed between parental and RR spheroids under irradiated conditions (**Figure 21H**).

In the 4T1 model, the number of viable cells per 4T1 RR spheroid increased significantly from the 24 hours to 72 hours post-RT, concomitant with a significant decrease of the metabolic activity (**Figure 22C-J**). Further, RT had no significant impact on the overall metabolic activity of either parental or 4T1 RR spheroids at 24 or 72 hours after irradiation. Nevertheless, 4T1 RR spheroids exhibited higher metabolic activity than the parental spheroids under CTR and RT conditions (**Figure 22G, H**). These findings suggest that, after an initial response to irradiation, RR spheroids seem to recover from the damage induced by RT between the evaluated time points.

Overall, the 2D and 3D *in vitro* models revealed distinct radiation responses among the MDA-MB-468 RR, 4T1 RR, MDA-MB-231 RR models and their respective parental counterparts. These findings further demonstrate that radioresistance is highly model-dependent and reinforce the molecular heterogeneity of TNBC. Moreover, the differences observed between 2D and 3D cultures highlight the importance of biomimetic tumor spheroid models, which more faithfully recapitulate the complex TME and uncover irradiation-induced phenotypes that are not fully captured by conventional monolayer cultures.

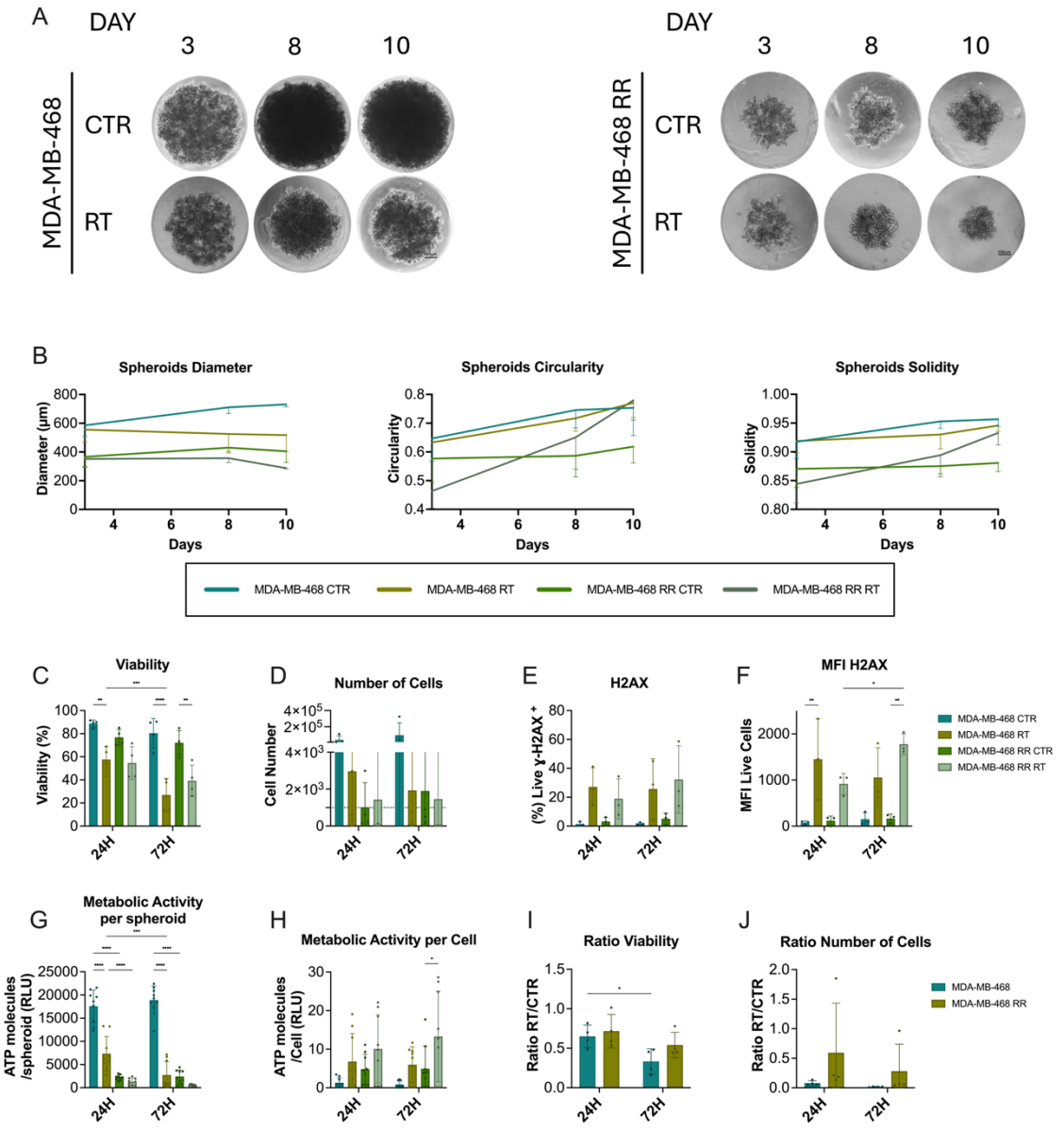


Figure 21 - Hypofractionated radiotherapy induces differently impacts cell survival and γ-H2AX expression in parental and resistant MDA-MB-468 breast tumor spheroids.

Tumor spheroids (TS) were exposed to 5 fractions of 5.2 Gy over 5 consecutive days (RT) or left without treatment (CTR) and analysed 24 hours and 72 hours after the last irradiation (IR). (**A**) Brightfield images of MDA-MB-468 and MDA-MB-468 RR TS (Day 3, 7 and 10) in CTR and RT conditions. Scale represents 100µm. (**B**) Spheroids diameter, circularity and solidity were determined along time (day 1, 3, 5, 7 and 10) in CTR and RT conditions, through the analysis of five brightfield microscopy images per experiment, using the ImageJ software. (**C**) TS viability (% viable cells) and (**D**) number of viable cells per spheroid determined through flow cytometry by live/dead staining. (**E**) Live cells $^{+}$γ-H2AX histone (pS139) and (**F**) Median fluorescence intensity (MFI) of γ-H2AX histone (pS139), determined through flow cytometry. Intracellular ATP molecules analysis (**G**) per spheroid and (**H**) per live cell of TS through CellTiter-Glo assay (relative light unit (RLU)) Data are representative of at least 3 independent experiments. (**I**) Ratio of TS viability (% RT/CTR) and (**J**) ratio of number of cells per spheroid (RT/CTR). All comparisons were performed using two-way ANOVA (B-J) (*p < 0.05, **p < 0.01, ***p > 0.001, ****p < 0.0001).

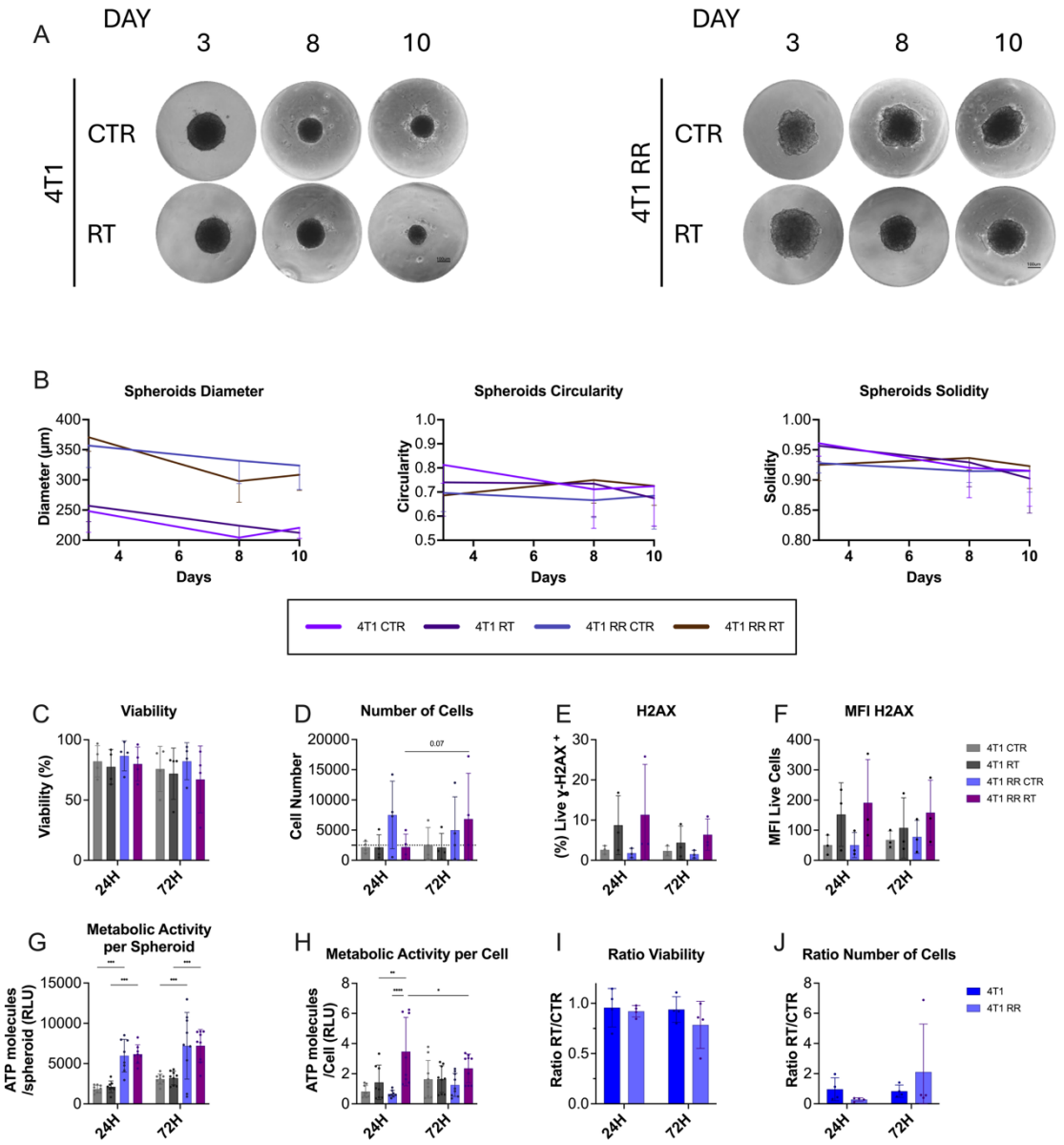


Figure 22 - Hypofractionated radiotherapy induces differently impacts in cell survival and metabolic activity in parental and resistant 4T1 breast tumor spheroids.

Tumor spheroids (TS) were exposed to 5 fractions of 5.2 Gy over 5 consecutive days (RT) or left without treatment (CTR) and analysed 24 hours and 72 hours after the last irradiation (IR). (**A**) Brightfield images of 4T1 and 4T1 RR TS (Day 3, 7 and 10) in CTR and RT conditions. Scale represents 100µm. (**B**) Spheroids diameter, circularity and solidity were determined along time (day 3, 8 and 10) in CTR and RT conditions, through the analysis of five brightfield microscopy images per experiment, using the ImageJ software. (**C**) TS viability (% viable cells) and (**D**) number of viable cells per spheroid determined through flow cytometry by live/dead staining. (**E**) Live cells $^{+}$γ-H2AX histone (pS139) and (**F**) Median fluorescence intensity (MFI) of γ-H2AX histone (pS139), determined through flow cytometry. Intracellular ATP molecules analysis (**G**) per spheroid and (**H**) per live cell of TS through CellTiter-Glo assay (relative light unit (RLU)) Data are representative of at least 3 independent experiments. (**I**) Ratio of TS viability (% RT/CTR) and (**J**) ratio of number of cells per spheroid (RT/CTR). All comparisons were performed using two-way ANOVA (B-J) (*p < 0.05, **p < 0.01, ***p > 0.001, ****p < 0.0001).

4.1.4 – Irradiation differently impacts cell cycle and ROS production in 3D models

Since the therapeutic effects of ionizing radiation are largely mediated through the induction of reactive oxygen species (ROS), which generate DNA damage and activate cell cycle checkpoints, we next investigated ROS production and cell cycle distribution at 24 and 72 hours after irradiation. These analyses aimed to determine whether alterations in oxidative stress and cell cycle regulation contribute to the radioresistant phenotype.

Under CTR conditions, all TNBC spheroids exhibited a higher proportion of cells in the G1 phase than in the S or G2/M phases, except for the MDA-MB-468 RR spheroids, which displayed similar proportions of cells in G1 and G2/M phases (**Figure 23A, B**). Following RT, both parental and RR spheroids derived from the MDA-MB-231, MDA-MB-468, and 4T1 cell lines showed an increased proportion of cells in the G2/M phase at 24 hours post-treatment. By 72 hours after completion of the RT scheme, parental and RR 4T1 spheroids appeared to recover from a possible G2/M arrest, as evidenced by an increase in the G1 population to levels comparable to those observed under non-irradiated conditions (**Figure 23B**). In contrast, both parental and RR MDA-MB-231 and MDA-MB-468 spheroids maintained elevated proportions of cells in the G2/M phase at 72 hours. Nevertheless, the MDA-MB-231 RR and MDA-MB-468 RR TS cells exhibited lower G2/M levels than those observed at 24 hours post-RT, suggesting a partial recovery from the possible radiation-induced cell cycle arrest (**Figure 23A, B**).

Reduced intracellular ROS accumulation following RT has been associated with the acquisition of RR phenotype. To investigate whether this mechanism contributes to RR in our models, we evaluated both the percentage of ROS-positive cells and the mean fluorescence intensity (MFI), which reflects intracellular ROS levels. Parental MDA-MB-231 spheroids exhibited a significant decrease in the percentage of ROS-positive cells 24 hours after RT. However, compared with MDA-MB-231 RR TS cells, they showed an increase in the MFI of ROS, indicating higher intracellular ROS levels despite the lower percentage of ROS-positive cells (**Figure 23C, F**). At 72 hours post-RT, the elevated ROS levels were maintained in MDA-MB-231 TS cells, whereas the percentage of ROS-positive cells decreased in the MDA-MB-231 RR TS (**Figure 23C, F**). In contrast, the 4T1 model displayed a distinct response. Neither the parental nor the RR spheroids exhibited significant changes in the percentage of ROS-positive cells at either 24 or 72 hours after RT. Interestingly the MFI significantly decreases after RT in the 4T1 RR spheroids at 72 hours in comparison with 24 hours post-IR (**Figure 23D, G**). Lastly, non-irradiated MDA-MB-468 RR spheroids exhibited a lower proportion of ROS-positive cells than the corresponding parental spheroids. Following RT, the intracellular ROS levels remained unchanged in MDA-MB-468 RR spheroids; however, similarly to the parental TS cells, they demonstrated a significant decrease in the percentage of ROS-positive cells upon RT (**Figure 23E, H**). Overall, RT induced an accumulation of cells in the G2/M phase at 24 hours in both parental and RR tumor spheroids. By 72 hours, all RR spheroids exhibited a partial recovery of the cell cycle profile, accompanied by reduced ROS accumulation, reflected either by a decrease in the proportion of ROS-positive

cells or in intracellular ROS levels, depending on the TNBC model. These findings suggest that modulation of oxidative stress together with recovery from the radiation-induced G2/M checkpoint may contribute to the acquisition of the radioresistant phenotype.

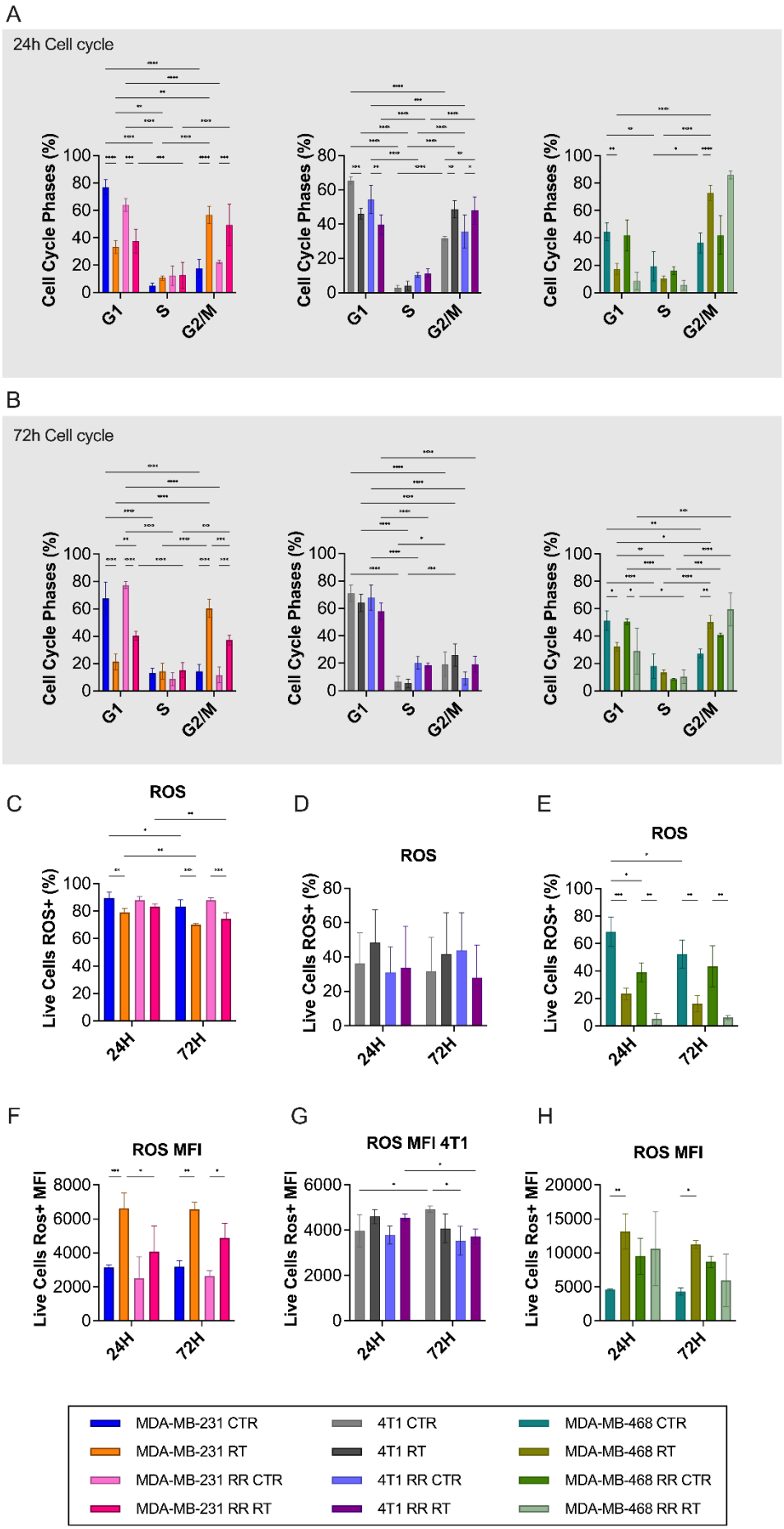

A
24h Cell cycle
Cell Cycle Phases (%)
G1
S
G2/M
B
72h Cell cycle
C
ROS
Live Cells ROS+ (%)
24H
72H
D
ROS
E
ROS
F
ROS MFI
Live Cells Ros+ MFI
G
ROS MFI 4T1
H
ROS MFI
MDA-MB-231 CTR
MDA-MB-231 RT
MDA-MB-231 RR CTR
MDA-MB-231 RR RT
4T1 CTR
4T1 RT
4T1 RR CTR
4T1 RR RT
MDA-MB-468 CTR
MDA-MB-468 RT
MDA-MB-468 RR CTR
MDA-MB-468 RR RT

Figure 23 - Hypofractionated radiotherapy induces distinct cell cycle arrest and reactive oxidative species (ROS) production between parental and radioresistant breast tumor spheroids.

MDA-MB-231, MDA-MB-468 and 4T1 parental and RR Tumor spheroids (TS) were exposed to 5 fractions of 5.2 Gy over 5 consecutive days (RT) or left without treatment (CTR) and analysed 24 h and 72h after the last irradiation (IR). Cell Cycle analysis of live cells of TS at (**A**) 24h and (**B**) 72h through flow cytometry. Reactive oxygen species (ROS)+ cells for (**C**) MDA-MB-231, (**D**) 4T1 and (**E**) MDA-MB-468 parental and RR TS. Mean fluorescence intensity (MFI) of ROS levels for (**F**) MDA-MB-231, (**G**) 4T1 and (**H**) MDA-MB-468 parental and RR TS. All comparisons were performed using two-way ANOVA (A-H) (*$p < 0.05$, **$p < 0.01$, ***$p > 0.001$, ****$p < 0.0001$).

4.2 Model Transition induces significant phenotypical and molecular changes in TNBC cells

Nunes, B. and Canha-Borges, A. et al. (2026). Radiotherapy induces layer-specific molecular and ultrastructural alterations in triple-negative breast cancer spheroids. Radiotherapy and Oncology, 111518.

3D models have recently been widely described as a bridge between *in vitro* and *in vivo* experiments. Although 2D cultures are well established for understanding cell behaviour, 3D culture more faithfully recapitulate the structural and biological complexity of solid tumors by preserving physiologically relevant cell-cell and cell-extracellular matrix interactions, spatial and phenotypic heterogeneity, and gene expression profiles, while reproducing oxygen and nutrient gradients that are absent in conventional 2D cultures. [59]

Given the molecular heterogeneity of TNBC, the highly invasive MDA-MB-231 cell line, representative of the mesenchymal stem-like (MSL) subtype, was selected as the experimental model. MDA-MB-231 spheroids previously established in our laboratory using microwell array technology (**Figure 9**), were characterized through mass spectrometry-based proteomic analysis to investigate the molecular alterations associated with the transition from a conventional 2D monolayer culture to a 3D spheroids.[49] Comparative proteomic profiling was performed to identify the physiological changes induced by 3D culture conditions.

Unfiltered principal component analysis (PCA) showed significant segregation between the two models (**Figure 24A**). These differences were further confirmed by a heatmap analysis performed based on Z-score normalization displaying two distinct models (**Figure 24B**). More than 6800 proteins were identified in 3D and 2D conditions, with >88% overlap of proteins identified between the two *in vitro* models. Among them, 720 were identified as upregulated and 558 as downregulated in the 3D model in comparison with the 2D culture. 558 proteins were exclusive in the 3D model and 247 were exclusive in the 2D model (**Figure 24C**). We next identified the main Gene Ontology (GO) terms characterizing key differences between 2D and 3D conditions (**Supplementary table 1**). The transition from 2D to 3D implied significant alterations on pathways related with lipid metabolism, chromatin organization, cell cycle regulation and nuclear activity (**Figure 24D**). These adaptions, driven by possible lower oxygen and nutrient levels, and spatial architecture, are critical for cell survival under stress conditions like RT, making spheroids a more physiologically relevant and predictive model for studying tumor response to RT than conventional 2D cultures.

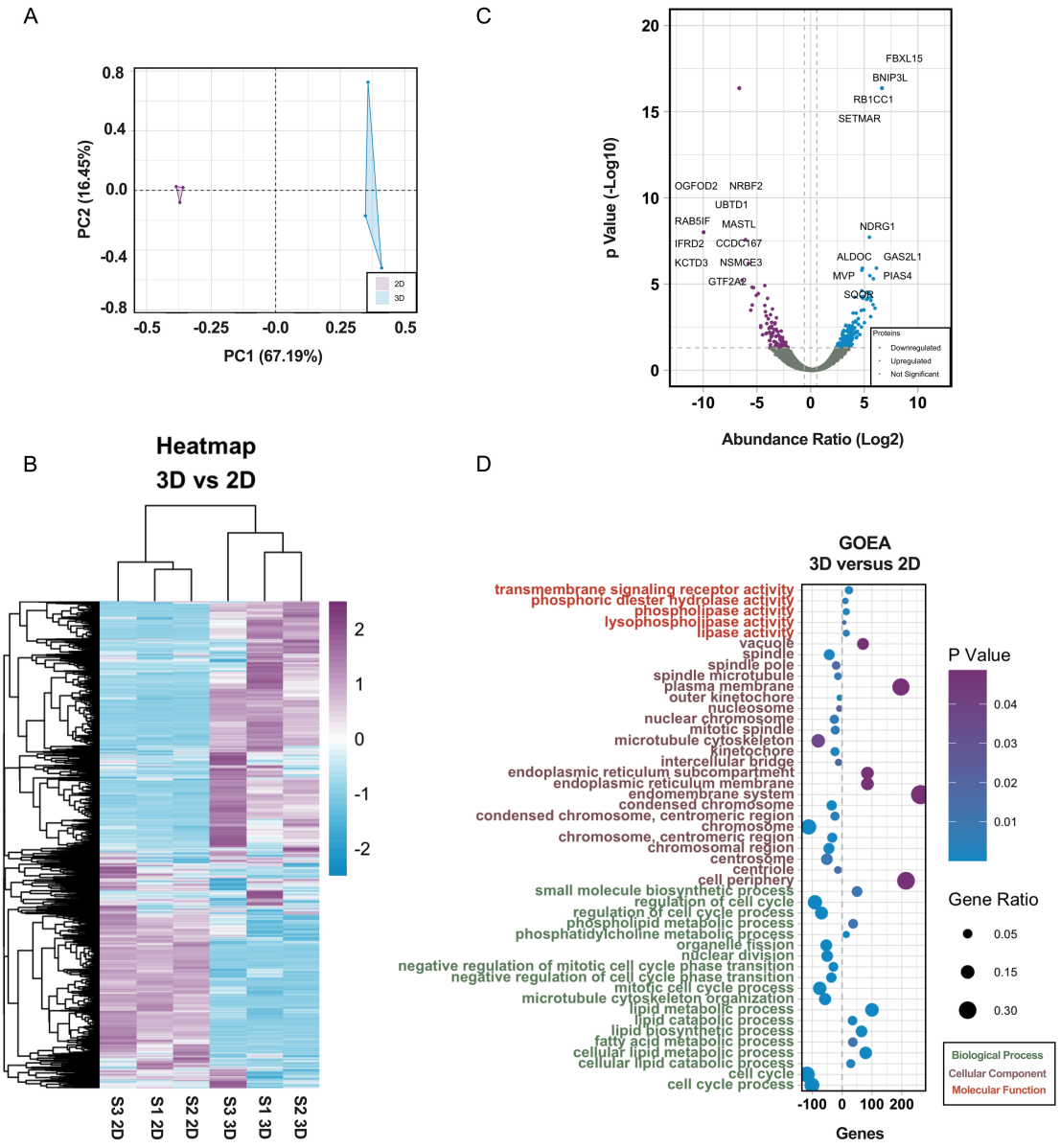


Figure 24 - Proteomic analysis reveals significant cell signature alterations in 3D models.

(A) PCA plot analysis for 2D and 3D models. **(B)** Heatmap analysis of all proteins differently expressed between 3D and 2D models normalized by Z-score. **(C)** Volcano Plot for proteins upregulated, downregulated and not significantly expressed in 3D compared with 2D models. **(D)** Gene ontology enrichment analysis (GEOA) performed for upregulated and downregulated proteins regarding distinct biological processes, cellular components and molecular functions. (Reprinted from Nunes, B. and Canha-Borges, A. et al., Radiotherapy and Oncology, 2026)

4.3 Establishment and Characterization of 3D Tumor Spheroids after Irradiation

Nunes, B. and Canha-Borges, A. et al. (2026). Radiotherapy induces layer-specific molecular and ultrastructural alterations in triple-negative breast cancer spheroids. Radiotherapy and Oncology, 111518.

Following the characterization of the cell molecular profile induced by the 2D to 3D transition, the impact of IR on the RS spheroids was evaluated. To accomplish this, we exposed MDA-MB-231 TNBC spheroids (TS) to a clinically relevant scheme, 5 fractions of 5.2 Gy (total of 26 Gy) followed by a multi-parameter analysis by transmission electron microscopy (TEM), proteomic and flow cytometry (**Figure 25**).

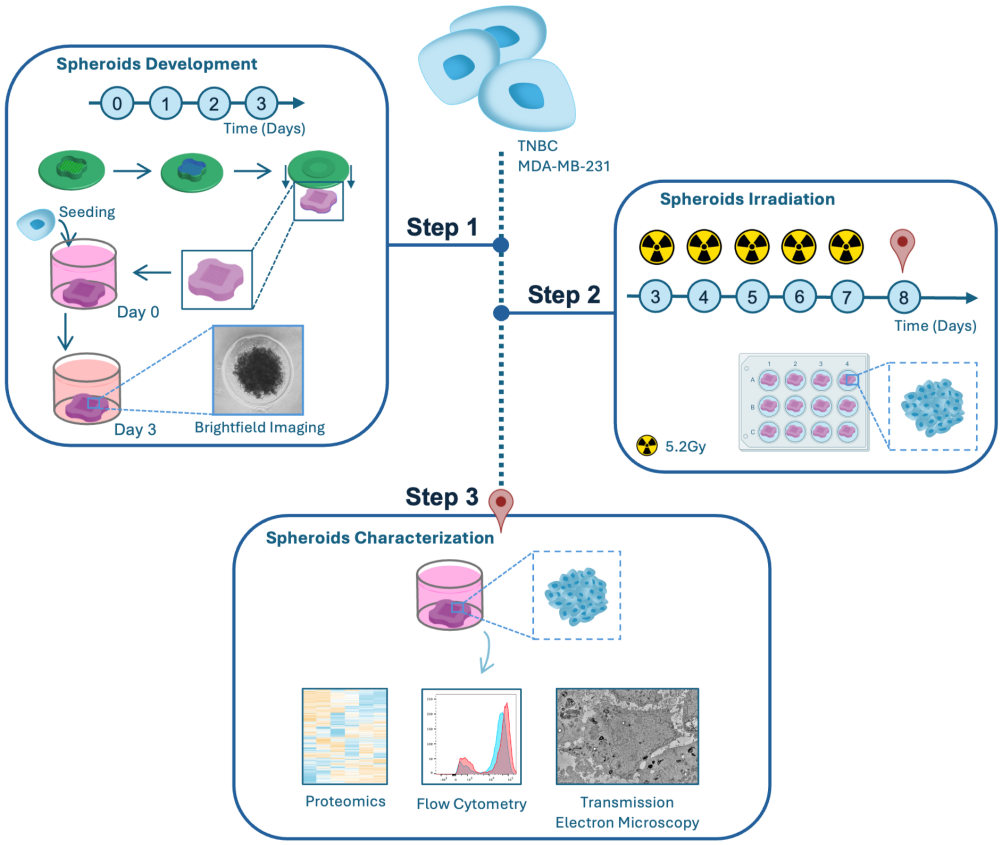


Figure 25 – Radiotherapy impact study on TNBC spheroids.

Overview of study scheme designed to analyse the impact of a clinically relevant scheme (26Gy) on MDA-MB-231 spheroids using techniques as proteomic, transmission electron microscopy and flow cytometry. (Created with BioRender.com)

(Reprinted from Nunes, B. and Canha-Borges, A. *et al*., Radiotherapy and Oncology, 2026)

4.3.1 – Radiosensitive MDA-MB-231 Spheroids suffer significant molecular and phenotypical changes after a clinical relevant radiotherapy scheme

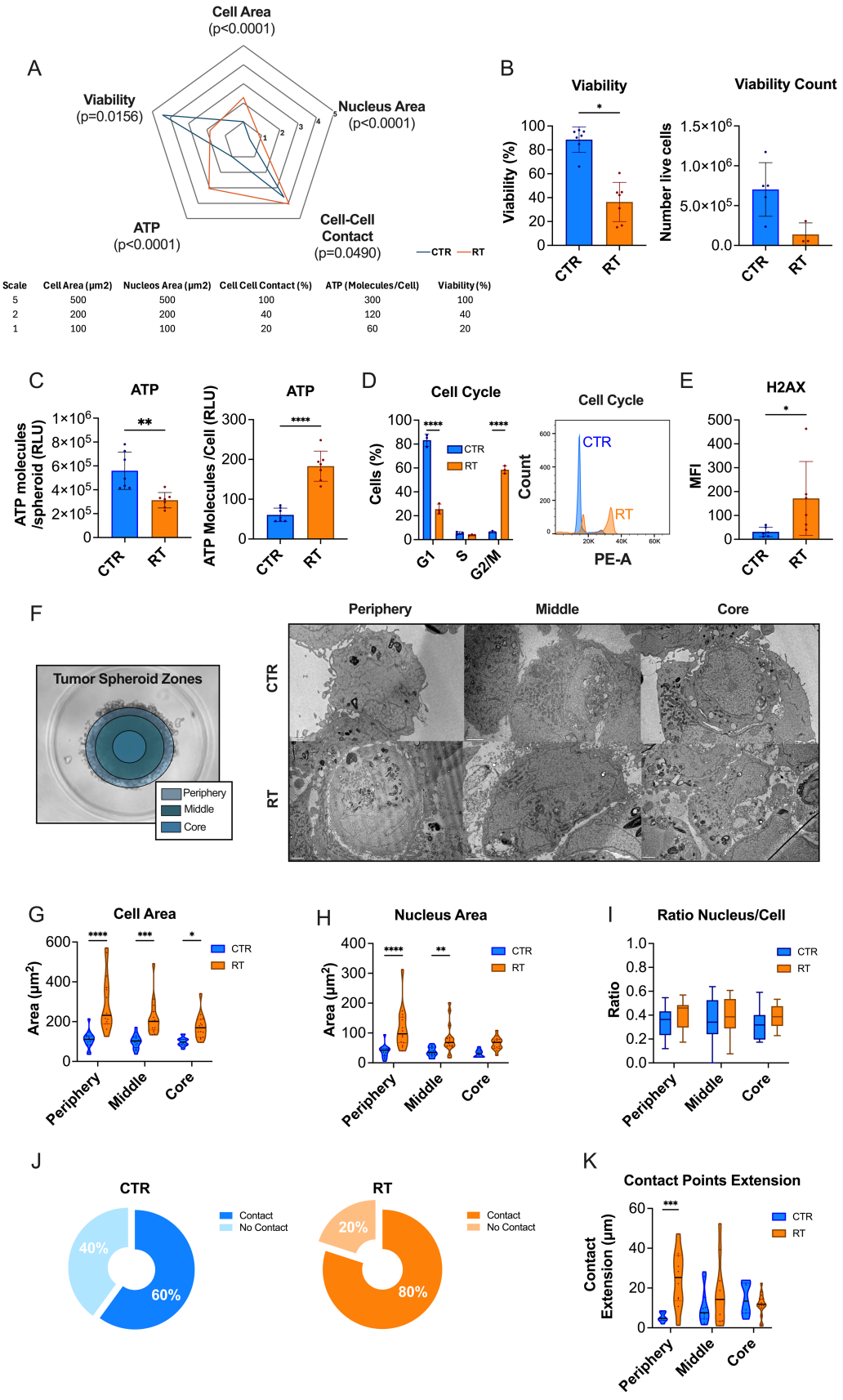
We conducted a multi-parameter analysis to assess the RT biological impact on TS. RT induced a significant decrease in the percentage of live cells, exceeding in 2-fold, compared to non-irradiated cells (CTR), as expected (**Figure 26A and B**). Interestingly, despite the overall decrease in cell viability and ATP molecules per spheroid, metabolic activity was found to be significantly higher in the irradiated viable cells remaining, surpassing a 2-fold increase (**Figure 26A and C**). This observation may reflect an adaptive metabolic response to radiation-induced stress. An accumulation of cells in G2/M phase was also observed (**Figure 26D**). To investigate IR-induced DNA damage, we quantified the levels of phosphorylated y-H2AX (pS139), which are

frequently enhanced as part of DNA damage response (DDR).[60] A marked phosphorylation of H2AX post-IR was observed, exceeding 3-fold 24 h after the last RT fraction, suggesting radiation-induced double-strand breaks (DSBs) (**Figure 26E**). To complement morphological and functional analyses, we employed transmission electron microscopy (TEM) to detail RT-induced ultrastructural alterations at the subcellular level, providing high- resolution visualization of organelles, membranes, and of the intracellular architecture. As 3D spheroids present distinct spatial zones, usually including a proliferative outer layer, a metabolically quiescent zone, and a necrotic or hypoxic core, each of these zones may respond differently to radiation due to variations in oxygen and nutrients availability, cell cycle status and cell–cell interactions. [61] Thus, ultrastructural analysis considered alterations visualized along these 3 regions: periphery, middle and core (**Figure 26F**). Through ultrastructural imaging, we observed that upon RT, cell area was increased in more than 2-fold in comparison to CTR (**Figure 26A and G and Supplementary Figure 1**), which was confirmed by flow cytometry analysis. Although significantly enhanced across all model layers, it was more pronounced at the periphery and gradually decreased towards the core.

Similarly, nucleus area also increased upon RT, being significant at spheroids periphery and middle layers (**Figure 26A and H**). Changes in the ratio of the nucleus to cell size was also assessed, but no significant differences were found (**Figure 26I**). Through quantification of cell physical contacts, a significant increase in the contact points between cells was observed ($p = 0.038$), with approximately 20% more cells establishing contacts in the irradiated than in the non-irradiated condition (**Figure 26A and J and Supplementary Figure 1**). The extent of these contacts was also investigated considering the distinct regions of the spheroid, evidencing a significant increase at the periphery (**Figure 26K**). Overall, these results suggest that RT affects cells differently according to their location within the spheroid, highlighting the relevance of using a 3D model for radiobiology studies.

To assess how RT impacts 3D breast cancer spheroids, we used mass spectrometry-based proteomics and compared irradiated with non-irradiated conditions (**Supplementary Figure 2**). The analysis was performed 72 h after five fractions of 5.2 Gy, a timepoint at which both viability and metabolic activity had stabilized and showed comparable levels to those observed at 24 h. [49] This enabled the characterization of sustained radiobiology effects and longer-term RT adaptations in TNBC spheroids. Generally, principal component analysis demonstrated distinct clustering of control samples and irradiated ones (**Supplementary Figure 2A**), suggesting substantial RT effects on 3D spheroids proteome. This segregation was corroborated by a heatmap-based hierarchical clustering using Z-score normalization, reinforcing a RT signature in 3D breast TS (**Supplementary Figure 2B**). Further, this analysis identified 6493 proteins, where 200 were identified as significantly upregulated and 54 as downregulated in irradiated compared to non-irradiated spheroids (**Supplementary Figure 2C**). From these, 71 proteins were exclusively expressed after RT and 35 were exclusive in the non-irradiated condition (CTR) (**Supplementary Figure 2D and Supplementary Table 2**). We next performed an enrichment

GO analysis for the following categories: biological processes, molecular functions and cellular components (**Supplementary Figure 2E**). On a biological process basis, it was verified that most of the upregulated proteins in RT-treated spheroids are involved in pathways related with cell cycle and organelles fission, highlighting an accumulation of cells in G2/M (CDK1, CCNB1, AURKA, UBE2C, TPX2, CDCA5, FANCD2), while the downregulated proteins are more connected with proteins phosphorylation, including several kinases (NEK3, NEK4, NUAK1, PEAK1, SIK3) (**Supplementary Table 3**). These alterations may suggest a decreased cellular capacity to respond to RT-induced stress, affecting DNA repair, cytoskeleton organization and survival. From a molecular perspective, the most significantly impacted pathways were involved with tubulin, cytoskeleton and microtubule activity. Lastly, cellular component analysis revealed that all enriched pathways were associated with upregulated proteins, primarily related to mitotic structure and chromosome organization. This suggests a cellular response focused on G2/M phase accumulation, as seen previously (**Supplementary Figure 2D**), likely reflecting radiation-induced cell cycle arrest and activation of DNA damage checkpoints.



Scale	Cell Area (µm2)	Nucleos Area (µm2)	Cell Cell Contact (%)	ATP (Molecules/Cell)	Viability (%)
5	500	500	100	300	100
2	200	200	40	120	40
1	100	100	20	60	20

Figure 26 - Hypofractionated radiotherapy induces distinct cellular effects across MDA-MB-231 breast tumor spheroids layers

Tumor spheroids (TS) were exposed to 5 fractions of 5.2 Gy over 5 consecutive days (RT) or left without treatment (CTR), and analyzed 24 h after the last irradiation (IR). (**A**) Radar graph visualization of cell area, nucleus area, cell–cell contacts, intracellular ATP and viability (clockwise) for RT and CTR conditions. Axes represent the median value for each parameter. (**B**) TS viability determined through flow cytometry by live/dead staining (% viable cells) and counted through trypan blue staining. (**C**) Intracellular ATP molecules analysis per spheroid and per live cell of TS through CellTiter-Glo assay (relative light unit (RLU)) (**D**) Cell Cycle analysis of live cells of TS and (**E**) Median fluorescence intensity (MFI) of γ-H2AX histone (pS139), determined through flow cytometry. (**F**) Transmission electron microscopy (TEM) images were obtained for the different TS layers – periphery, middle and core for both CTR and RT conditions. (**G**) Cell Area (μm^2), (**H**) Nucleus Area (μm^2) and (**I**) Ratio nucleus/cell area assessment for live cells in RT and CTR conditions across the different TS layers. (**J**) Cell-cell interaction through the % of cells that are in physical contact with others, and (**K**) extent of cell contacts (μm) in RT and CTR conditions, for the different TS layers. Data are representative of at least 3 independent experiments. All comparisons were performed using paired t-test (A-E,J) and two-way ANOVA (G-I,K) (*p < 0.05, **p < 0.01, ***p > 0.001, ****p < 0.0001). (Reprinted from Nunes, B. and Canha-Borges, A. *et al*., Radiotherapy and Oncology, 2026)

4.3.2 - Hypofractionated radiotherapy increases 3D breast cancer spheroids mitochondrial content

Mitochondria are particularly sensitive to RT due to their critical role in energy metabolism and their own mitochondrial DNA. Radiation-induced mitochondrial damage can disrupt organelle function and trigger reactive oxygen species (ROS) production, activating programmed cell death pathways and metabolic reprogramming.[62] To unveil the impact of hypofractionated RT on mitochondrial number and function across the different layers of TS, the mitochondria content (number per cell), area and width were taken into consideration (**Figure 27A-C**). We observed an approximately 2-fold increase in the mitochondrial content (number per cell) upon IR (**Figure 27A**), particularly visible at the periphery of the spheroid (**Figure27D**). Despite the increase of mitochondria content, no changes were observed in the area and width of these organelles (**Figure 27E and F**). Functionally, we observed a tendency for increased ROS production after IR (p value =0.056) (**Figure 27G**). To better understand the effects of RT within each organelle, an enrichment GO analysis for cellular components was used to extract the proteins related to the organelles studied (**Supplementary Tables 4 and 5**). Upregulated and downregulated proteins were then identified within each organelle. For the organelles that showed a significant cluster of proteins, both up- and down-regulated, an enrichment GO analysis was performed for biological pathways. Interestingly, after RT, upregulated proteins were mainly related with ATP production, organelle fission and organization, while the downregulated proteins were related with cell adherence (**Figure 27H and I and Supplementary Table 5**), suggesting an adaptation of this organelle to IR as an attempt to sustain cell survival under RT-induced damage.

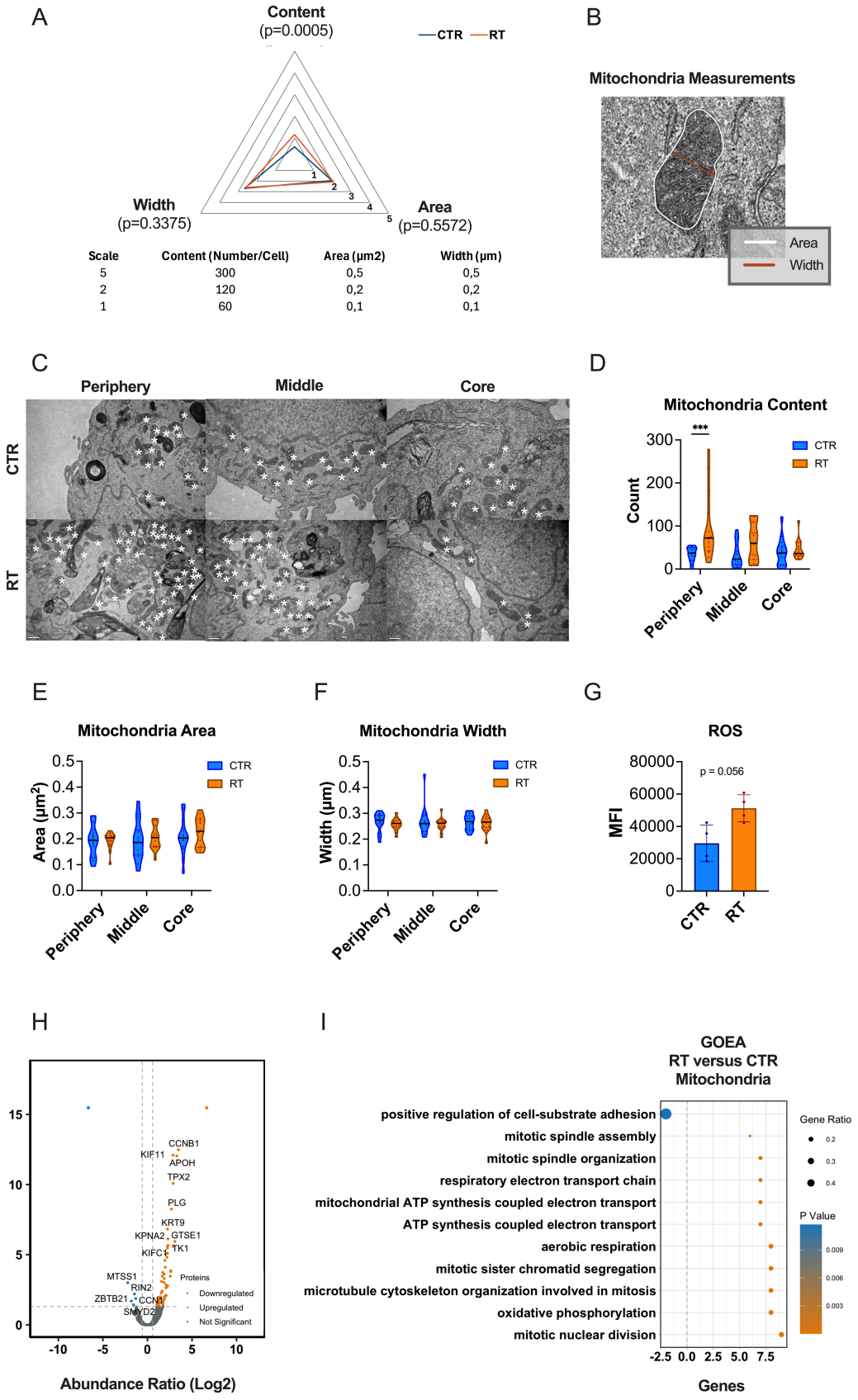


Figure 27 - Hypofractionated radiotherapy impacts mitochondrial content and function in MDA-MB-231 breast tumor spheroids.

Tumor spheroids (TS) were exposed to 5 fractions of 5.2 Gy over 5 consecutive days (RT) or left without treatment (CTR). TS were analyzed 24 h after the last irradiation (IR). (**A**) Radar graph for mitochondrial content, width and area of CTR

and RT conditions. (**B**) Illustration of the different measurements (area and width) analyzed per mitochondria. (**C**) Representative TEM images were obtained for the different spheroids layers within the TS for both CTR and RT conditions with particular focus on the mitochondrial content (indicated with *). (**D**) Mitochondrial content, (**E**) area (μm^2) and (**F**) width (μm) were assessed by manual quantification through ImageJ software in both conditions for the different layers. (**G**) Mean fluorescence intensity (MFI) of reactive oxygen species (ROS) levels. (**H**) Representative volcano plot informing differently expressed proteins related with mitochondria post-IR. (**I**) Gene ontology enrichment analysis (GEOA) performed for upregulated and down regulated proteins within biological processes for mitochondria related proteins. Data are representative of at least 3 independent experiments. All comparisons were performed using two-way ANOVA (D-F) and paired t-test (G) (*p < 0.05, **p < 0.01, ***p > 0.001, ****p < 0.0001). (Reprinted from Nunes, B. and Canha-Borges, A. *et al*., Radiotherapy and Oncology, 2026)

4.3.3 - Hypofractionated radiotherapy increases lipid droplets accumulation in the periphery of 3D breast cancer spheroids

Lipid droplets (LD) were previously observed to be affected after RT, preventing endoplasmic reticulum (ER) stress, lipid peroxidation, ROS increase and affecting other pathways related with cellular stress to prevent cell death.[63] Here, we further assessed how hypofractionated RT may impact these organelles number and size, across the different layers of tumor spheroids (**Figure 28A**). A 3-fold increase of LD counts upon RT was observed (**Figure 28B**) and confirmed by flow cytometry (p value = 0.063) (**Figure 28C**). Interestingly, this increase was particularly evident at the periphery of the TS (**Figure 28D**). Despite the increase in LD numbers, the area of these organelles decreased after RT (**Figure 28E and F**), independently of the region of the model analysed (**Figure 28G**). Moreover, exclusive proteins found in the irradiated TS (**Supplementary Table 2**), such as carnitine O-octanoyltransferase (CROT), major facilitator superfamily domain containing 6 (MFSD6) and apoliprotein L3 (APOL3) might support the lipid alterations here observed as a RT-protective mechanism.

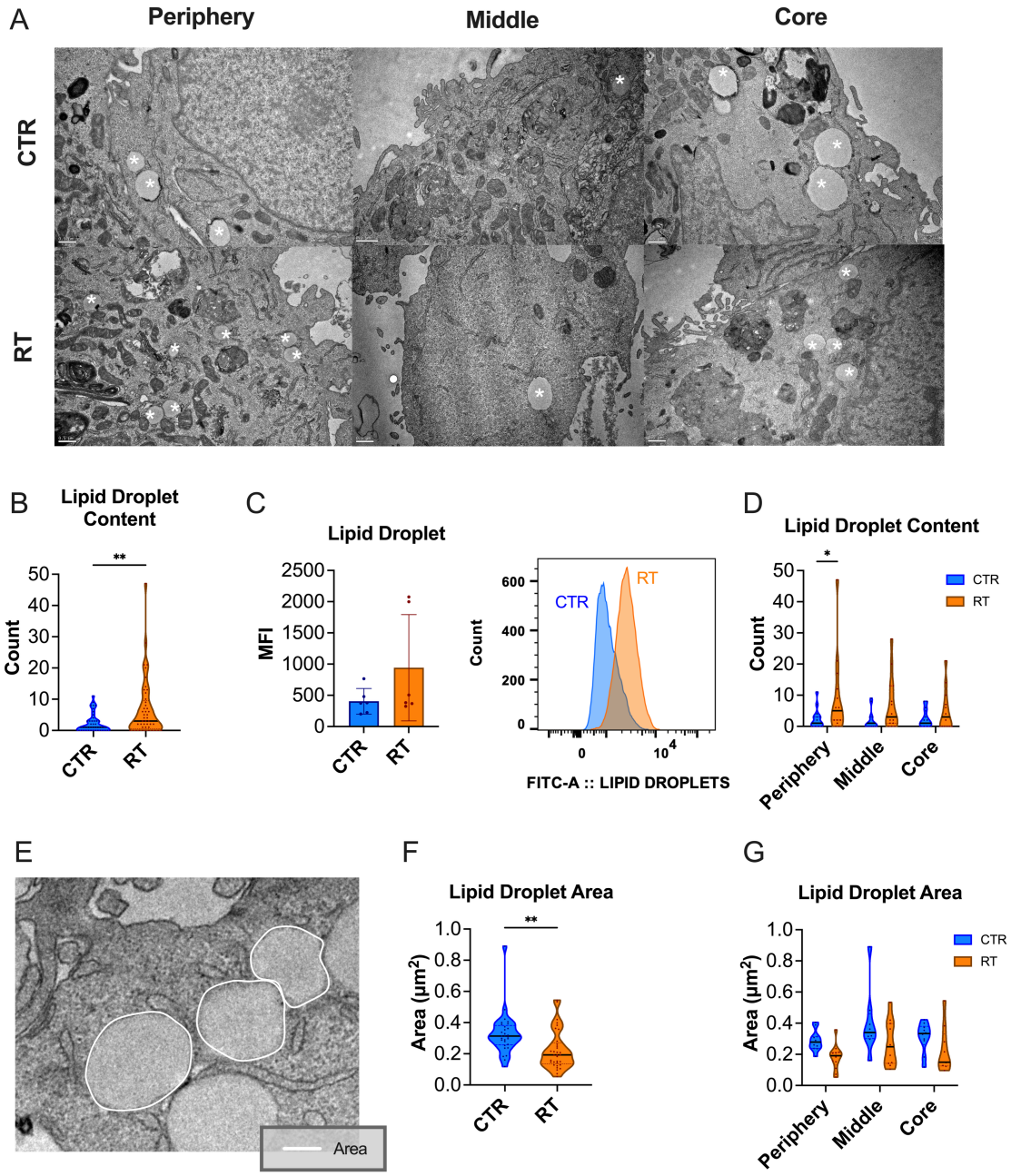


Figure 28 - Hypofractionated radiotherapy increases lipid droplets at the periphery of MDA-MB-231 breast tumor spheroids.

Tumor spheroids (TS) were exposed to 5 fractions of 5.2 Gy over 5 consecutive days (RT) or left without treatment (CTR). TS were analysed 24 h after the last irradiation (IR). (**A**) TEM images obtained for the different layers within the TS for both CTR and RT conditions where lipid droplets (indicated with *) are present. Scale represents 0.5 µm. Overall lipid droplet content in CTR and RT conditions was evaluated by (**B**) TEM and (**C**) flow cytometry. (**D**) Lipid Droplets number in CTR and RT conditions considering the different spheroid layers. (**E**) Illustration of lipid droplets area measurement. (**F**) Overall Lipid Droplets area (μm^2) number in CTR and RT conditions and (**G**) considering the different spheroid layers. Data are representative of at least 3 independent experiments. All comparisons were performed using paired t-tests (B,C,F) and two-way ANOVA (D,G) (*$p < 0.05$, **$p < 0.01$, ***$p > 0.001$, ****$p < 0.0001$). (Reprinted from Nunes, B. and Canha-Borges, A. *et al.*, Radiotherapy and Oncology, 2026)

4.3.4 - Hypofractionated radiotherapy increases rough endoplasmic reticulum and autophagic vesicles content in 3D breast cancer spheroids

In addition to mitochondrial and LD alterations, the endoplasmic reticulum (ER) is also significantly affected by ionizing radiation.[64] As a central hub for protein folding, lipid synthesis and calcium storage, ER plays a crucial role in maintaining cellular homeostasis.[65] To analyze the impact of hypofractionated RT in ER ultrastructure, we quantified the extent of rough (RER) and smooth (SER) membrane branching (number of ramifications) (**Figure 29A**), considering the presence or absence, respectively, of ribosomal structures close to the ramifications.

A pronounced increase of ER was observed upon IR within all layers of the spheroid, although more evident at the periphery of the model (**Figure 29B**). The differences were mainly due to RER (**Figure 29C**), which increased within all spheroid zones, while SER was maintained after RT, independently of the zone (**Figure 29D**). Interestingly, upon IR, these organelles seemed to migrate from their common subcellular location − close to the nucleus − to the cell membrane, throughout almost all the cells analysed on the periphery layer (**Supplementary Figure 3**). Proteomic analysis of the endoplasmic reticulum clusters shows that the downregulated proteins presented a high number of kinase activity terms, while most of the upregulated were related with stress response and organization (**Figure 29E and F and Supplementary Table 5**). These upregulated pathways were also observed in Golgi Complex clusters (**Supplementary Table 5 and Supplementary Figure 4A and B**). Once ER and Golgi Complex stress triggers autophagy [66], the number of autophagic vesicles were quantified (**Figure 29G**), evidencing a prominent increase mainly in the periphery of the spheroid upon RT exposure (**Figure 29H**). Further, an analysis on lysosome content (**Supplementary Table 5 and Supplementary Figure 4C and D**) showed nucleoside and ATP biosynthesis, as well as cell cycle terms enriched in upregulated proteins. Overall, these data support the phenotypic changes observed in irradiated spheroids, as well as the functional differences on ATP, cell cycle arrest and DNA damage in response to IR-induced stress.

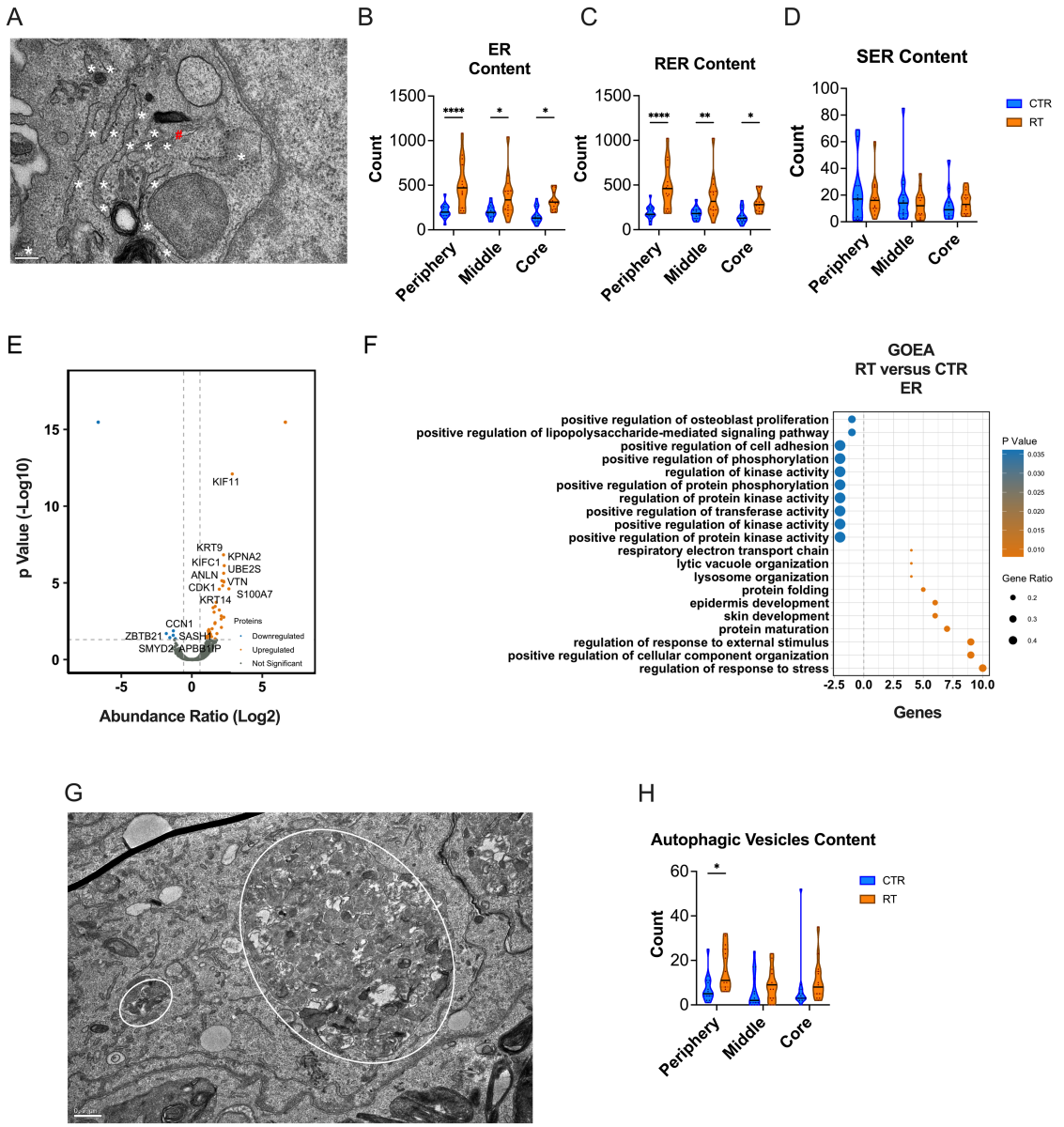


Figure 29 - Hypofractionated radiotherapy increases rough endoplasmic reticulum across all layers of the MDA-MB-231 breast tumor spheroids.

Tumor spheroids (TS) were exposed to 5 fractions of 5.2 Gy over 5 consecutive days (RT) or left without treatment (CTR). TS were analysed 24 h after last irradiation (IR). (**A**) Representative image obtained by TEM showing the presence of smooth endoplasmic reticulum ((SER), indicated with #) and rough endoplasmic reticulum ((RER), indicated with *) in TS. (**B**) Overall endoplasmic reticulum (ER) content in CTR and RT conditions for the different TS layers. (**C**) RER and (**D**) SER content in CTR and RT conditions for the different TS layers. (**E**) Representative volcano plot informing differently expressed proteins related with ER post-IR. (**F**) GO analysis performed for upregulated and downregulated proteins within biological processes for ER related proteins. (**G**) Representative image obtained by TEM showing the presence of autophagic vesicles. (**H**) Autophagic vesicles content assessment in CTR and RT conditions for the different TS layers. Data are representative of at least 3 independent experiments. All comparisons were performed using the two-way ANOVA (*p < 0.05, **p < 0.01, ***p > 0.001, ****p < 0.0001). (Reprinted from Nunes, B. and Canha-Borges, A. *et al.*, Radiotherapy and Oncology, 2026)

4.4 Unveiling the Proteomic Landscape of TNBC Spheroids-Derived Extracellular Vesicles

Irradiated cells, attempting to escape the damage caused by RT, not only modify their own metabolism, as they can also communicate with the non-irradiated tissue through gap junctions, secreted small molecules, or EVs, in a mechanism known as 'radiation-induced bystander effect (RIBE).[67] Through RIBE, soluble mediators and EVs released by irradiated cells can reprogram recipient cells, [68] promoting pro-survival signalling, proliferation, angiogenesis, invasion, metastasis, and the development of radioresistance.[69–71]

Cancer cells are described to exacerbate EVs secretion. In fact, it is estimated that an healthy individual presents around 2000 trillion EVs in circulation, while a cancer patient presents approximately 4000 trillion EVs in the bloodstream.[72] Moreover, ionizing radiation is also described to promote the release of EVs that act as secondary messengers, amplifying RT bystander effects.[73–76] Given their importance in cancer progression and in immune modulation, the role of EVs, either as targets or as vehicles of novel therapeutic approaches, has been explored during the past years.[77–79] Particularly, the role of irradiated cancer cells-derived EVs has attracted the attention of the scientific community, owing to their ability to promote radioresistance and/or tumor progression in a myriad of tumors, including breast cancer (**Figure 8**).

In order to understand the main changes induced by IR on TNBC EVs production, we isolated EVs upon exposure of the TS to a clinically relevant RT scheme. EVs were further characterized using TEM, dynamic light scattering (DLS), WB and LC/MS-MS proteomics to determine a possible EVs radiotherapy-signature. (**Figure 30**).

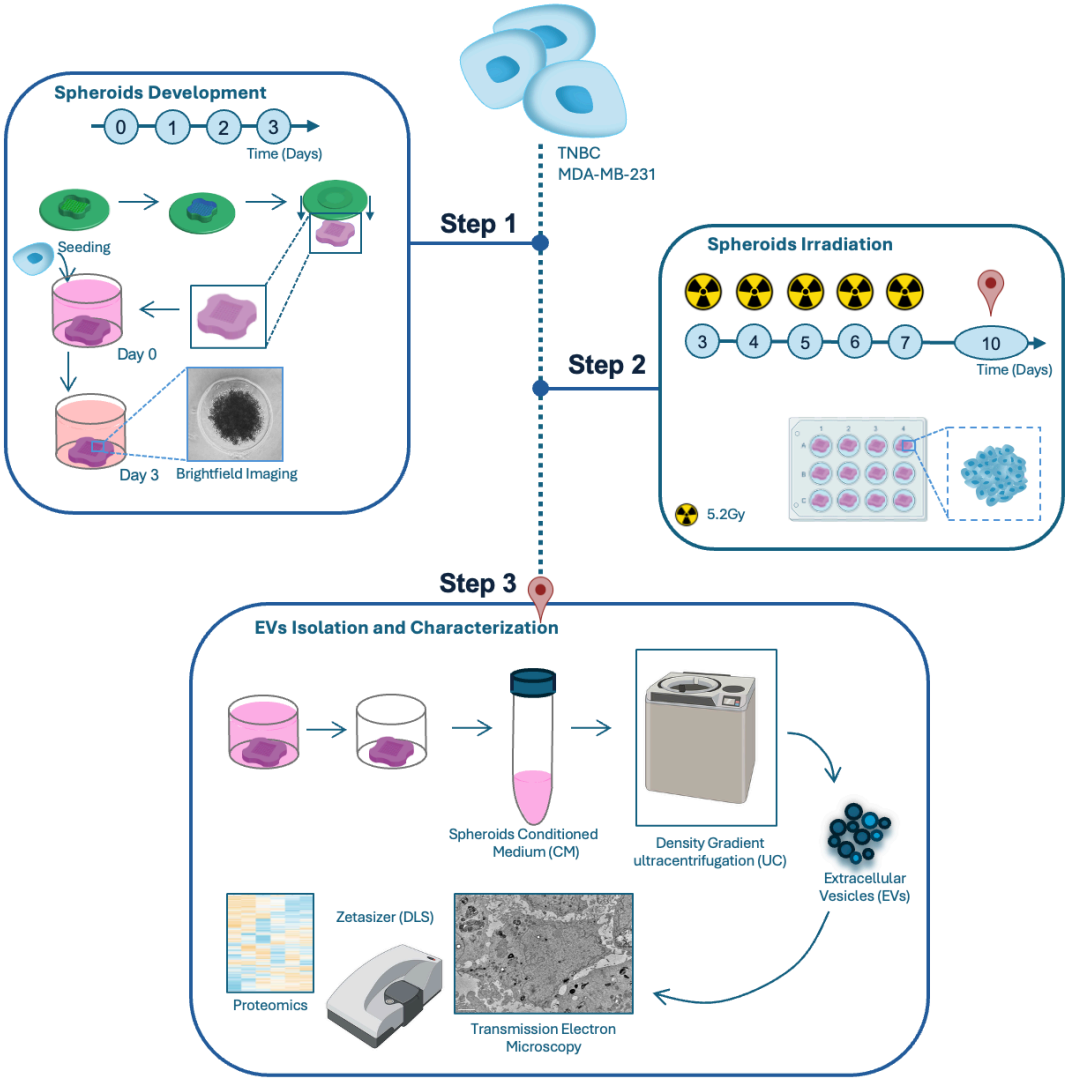


Figure 30 – Extracellular vesicles (EVs) isolated from triple negative breast cancer spheroids exposed to a clinical relevant radiotherapy scheme study.

Overview of study scheme designed to analyse the impact of a clinically relevant scheme (5x5.2 Gy) on MDA-MB-231 spheroids EVs content using techniques as LC/MS-MS proteomics, transmission electron microscopy, flow cytometry and zetasizer (Dynamic light scattering (DLS)). (Created with BioRender.com)

4.4.1 – Extracellular vesicles isolation techniques: ultracentrifugation, size exclusion chromatography and ultrafiltration

EVs isolation history has comprehended a vast number of techniques with different yield and purity levels.[80] Therefore, we started by testing 3 different widely used EV isolation protocols: Size exclusion Chromatography (SEC), differential ultracentrifugation (UC) and UC + ultrafiltration (UF) (10kDa cut off) followed by characterization by TEM, Zetasizer (DLS) and protein quantification. Briefly, TS were exposed to a clinically relevant scheme, 5 fractions of 5.2 Gy (26 Gy in total), and the conditioned medium (CM) was collected after 72 hours and submitted to EVs isolation and characterization.

TEM images confirmed the presence of particles in all isolation methods. The SEC technique seems to co-isolate a higher concentration of contaminants, visible shown as dark aggregates, whereas the UC technique yielded a puree sample (**Figure 31A**). Both SEC and UC + UF techniques showed a high protein yield in both CTR and RT conditions, whilst the UC resulted in a very low protein recovery (**Figure 31B**). To further complement this analysis the number of particles isolated by each method was determined through DLS. SEC and UC + UF showed high values within the conditions reaching ~10^{10} - 10^{14} particles/mL. The lowest number of particles was isolated within the UC method (**Figure 31C**), which agrees with lower protein content.

The UC + UF technique was selected due to its intermediate levels of contaminants and high number of both protein and particles

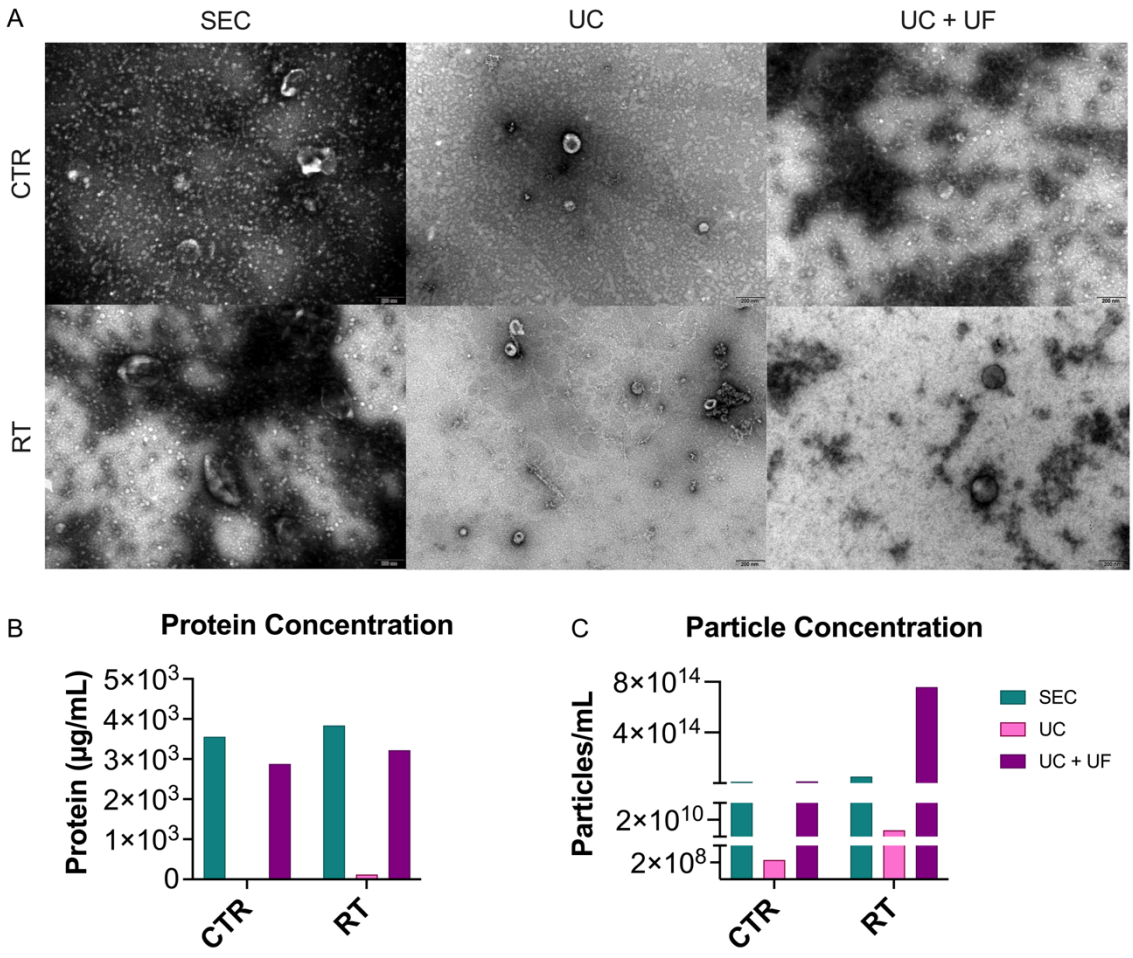


Figure 31 – Ultracentrifugation combined with Ultrafiltration technique results in a high yield of extracellular vesicles from MDA-MB-231 breast tumor spheroids exposed to an hypofractionated radiotherapy.

Tumor spheroids (TS) were exposed to 5 fractions of 5.2 Gy over 5 consecutive days (RT) or left without treatment (CTR). Conditioned medium (CM) was collected 72 hours after RT and extracellular vesicles (EVs) were isolated by size exclusion chromatography (SEC), differential ultracentrifugation (UC) and UC + ultrafiltration (UC+ UF). (**A**) Representative image obtained by TEM showing the presence of particles within the samples. scale represents 200nm. (**B**) Protein Quantification (ug/mL) and (**C**) Particle concentration (Particles/mL) in CTR and RT conditions.

4.4.2 – Radiotherapy significantly increases extracellular vesicle secretion and particle size in MDA-MB-231 breast tumor spheroids

EVs have emerged as promising tools for clinical applications in TNBC, including drug delivery, diagnostic and prognostic biomarkers, as well as novel therapeutic strategies aimed at overcoming treatment resistance.[81] In the context of RT, EVs are also gaining increasing attention, as radiation has been associated with enhanced EV release and alterations in their molecular cargo, both of which have been implicated in mechanisms of RR. [70] To investigate the role of RT on EV secretion and cargo, we isolated EVs released by MDA-MB-231 TS 72 hours after the end of a clinically relevant RT regimen for TNBC (5x5.2 Gy). The isolated EVs were then characterized in terms of size distribution, particle concentration, and the expression of selected EV-associated markers.

Following RT, a multiparametric analysis was performed to radiation-induced changes in EVs release and composition. Through TEM we observed the presence of vesicular particles displaying the characteristic morphology of EVs in both conditions (**Figure 32A**). Interestingly, a trend towards an increased number of EVs released per spheroid was observed in IR conditions (**Figure 32B**). Moreover, when EV production was normalized to the number of cells within each spheroid, a significant increase in EV release per cell was detected after RT (**Figure 32C**).

The size of the isolated EVs ranged from approximately 100 to 200 nm, falling within the reported size ranges of the main EV subtypes. Although particle size alone does not distinguish EV subtypes, this distribution overlaps with the reported size ranges of exosomes (30–120nm), microvesicles (150–1000nm), and apoptotic bodies (100–5000nm).[82,83] Overall, the particle size distribution in both experimental conditions was consistent with the expected size range for EVs (**Figure 32D**). Interestingly, EVs isolated from RT tumor spheroids exhibited a larger mean particle size than those derived from non-IR control spheroids, suggesting that RT influences both EV secretion and their biophysical characteristics. To further validate the presence of EVs in these samples, the expression of EV-enriched markers recommended by the MISEV (Minimal Information for Studies of Extracellular Vesicles) guidelines was assessed via western blotting (WB) [84]: Specifically, the tetraspanins CD63/CD81 together with the cytosolic FLOT1/ALIX were analysed. All four markers were detected in EV preparations obtained from both CTR and irradiated TS, confirming the successful isolation of EVs. As expected, CD63 and FLOT1 were also detected in MDA-MB-231 cellular lysates, reflecting their physiological intracellular expression. In contrast, CD81 and ALIX were predominantly enriched in the EV fractions under the experimental conditions analysed, supporting the enrichment of the isolated vesicles (**Figure 32E**).

As RT significantly reduced TS viability (**Figure 26B**), we next investigated whether IR altered the composition of the isolated EV samples by assessing markers associated with apoptosis. Ionizing radiation induces apoptotic cell death, leading to the release of phosphatidylserine (PS)-positive

vesicles, including apoptotic bodies, into the conditioned medium. Annexin V, which binds to exposed PS, was therefore analysed together with the ER marker GRP78 and the mitochondrial protein cytochrome c by WB. Annexin V-positive apoptotic EVs have low or undetectable levels of the EV-enriched markers present in non-apoptotic EVs, being a good marker for apoptotic bodies.[85] Once these vesicles are cellular fragments, organelles as ER (GRP78) and mitochondria (Cytochrome C) can also be included. [82,85] Annexin V was detected in EV preparations from both CTR and RT spheroids, as well as in the corresponding cellular lysates. Interestingly, cytochrome C was detected exclusively in EVs isolated from IR spheroids and cell lysates, whereas GRP78 was only detected in the cellular lysates (**Figure 32E**). The absence of GRP78 supports minimal contamination of the EV preparations with cellular debris, while the presence of cytochrome c following RT is consistent with IR-induced mitochondrial stress and apoptosis. Together with the increased Annexin V signal, these findings suggest that irradiation alters the composition of the released EV population and may promote the release of apoptosis associated vesicles.

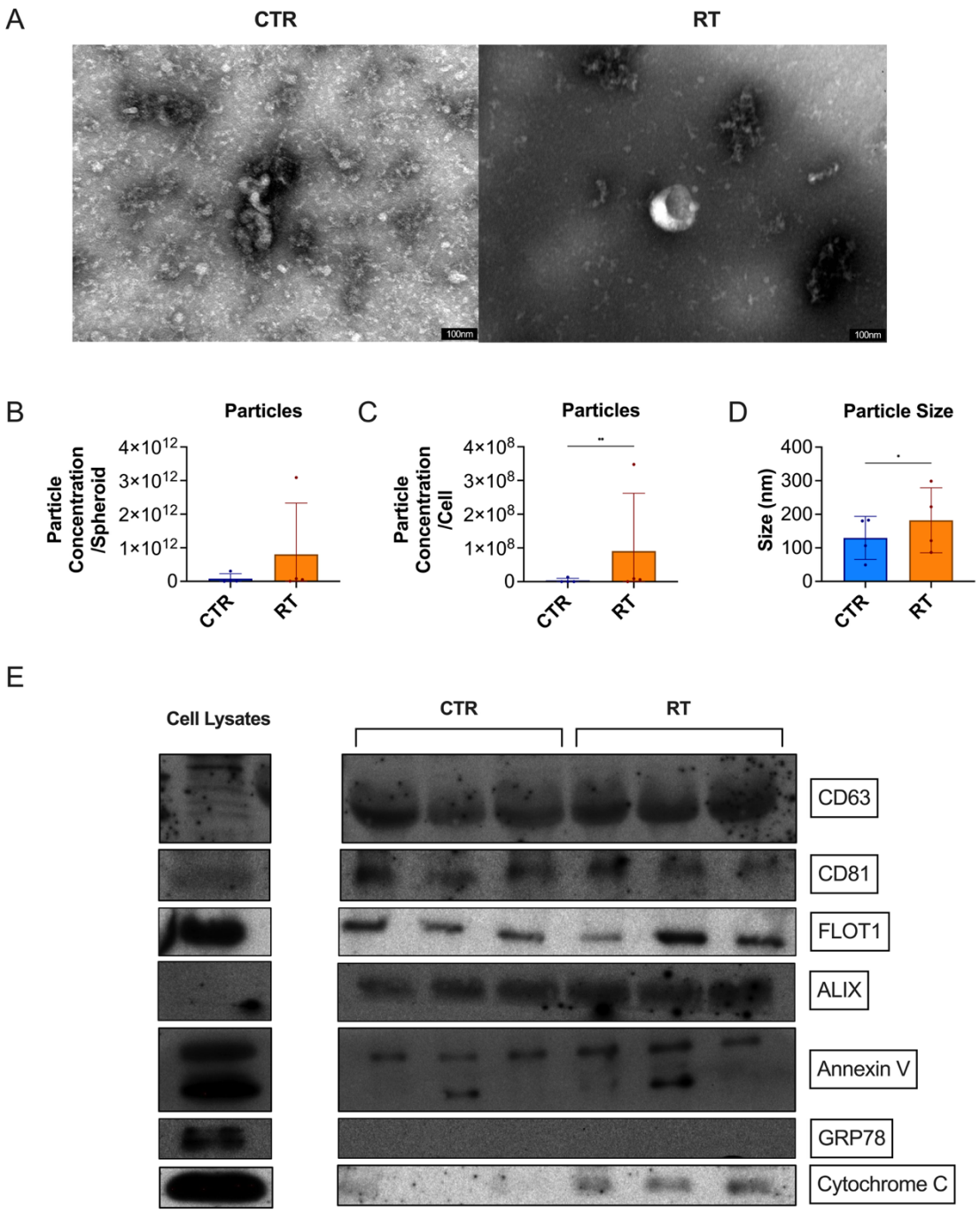


Figure 32 – Hypofractionated radiotherapy increases extracellular vesicles production and size in MDA-MB-231 breast tumor spheroids.

Tumor spheroids (TS) were exposed to 5 fractions of 5.2 Gy over 5 consecutive days (RT) or left without treatment (CTR). Conditioned medium (CM) was collected 72 hours after RT, and extracellular vesicles (EVs) were isolated by ultracentrifugation + ultrafiltration. (**A**) Representative image obtained by TEM showing the presence of particles within the CTR and RT conditions. Scale represents 100nm. Particle concentration (Particles/mL) per spheroid (**B**) and per cell (**C**) in CTR and RT conditions. (**D**) Particles size (nm) in CTR and RT conditions. (**E**) EVs were analysed by western blotting (WB) with anti-CD63 antibody (ab), anti-CD81 ab, anti-flotilin1 (FLOT1) ab, anti-ALIX ab, anti-annexin V ab, anti-GRP78 ab and anti-Cytochrome C ab. Data are representative of at least 3 independent experiments. All comparisons were performed using the t test (*p < 0.05, **p < 0.01, ***p > 0.001, ****p < 0.0001)

4.4.3 – Extracellular vesicles proteomic profile is significantly altered after irradiation

To further characterize the effects of RT on the protein cargo of EVs, a mass spectrometry-based proteomic analysis was performed. MDA-MB-231 spheroids were exposed to a clinical relevant hypofractionated RT regimen (5 × 5.2 Gy), and EVs were isolated 72 hours after the end of the treatment for proteomic profiling.

As an initial quality assessment, proteins recommended by the MISEV guidelines as positive EV markers, together with negative markers used to evaluate sample purity, were examined within the proteomic dataset. At least four proteins from each category were identified (**Figure 33A-D)** further supporting the successful isolation of EVs. Interestingly, FLOT1, which was also detected by WB (**Figure 32E**), was significantly less abundant in EVs derived from irradiated spheroids than in controls. In contrast, the abundance of CD47 and cytochrome c (CYCS) was significantly increased following RT (**Figure 33A, B and D**).

Unfiltered principal component analysis (PCA) revealed a clear separation between EVs isolated from CTR and irradiated spheroids, indicating distinct proteomic profiles (**Figure 33E**). This differential protein signature was further illustrated by hierarchical clustering and heatmap analysis based on Z-score normalization, which demonstrated a clear segregation between the two experimental groups (**Figure 33F**). Overall, more than 1200 proteins were identified in EVs derived from both CTR and RT spheroids, with over 90% of the identified proteins shared between the two conditions. Comparative analysis revealed 73 proteins with significantly increased abundance and 36 proteins with significantly decreased abundance in EVs isolated from irradiated spheroids relative to controls. In addition, 58 proteins were exclusively detected in EV from RT-treated spheroids, whereas 18 proteins were exclusive in EVs from CTR spheroids (**Figure 33G**).

To gain further insight into the biological processes associated with the radiation-induced alterations in the EV proteome, gene set enrichment analysis (GSEA) was performed using the complete proteomic dataset, with proteins ranked according to their fold change between irradiated and CTR conditions. This analysis identified distinct gene ontology (GO) signatures in EVs derived from CTR and RT conditions, with significant enrichment of pathways related to DNA repair, chromatin organization and nucleosome binding in RT group, together with a decrease of proteins associated with ECM and extracellular structure organization (**Figure 33H**). These alterations closely mirrored the proteomic changes previously identified in the corresponding cellular counterparts (**Supplementary Figure 2**), particularly the enrichment of DNA repair-related pathways, suggesting that EVs reflect key molecular adaptations induced by RT.

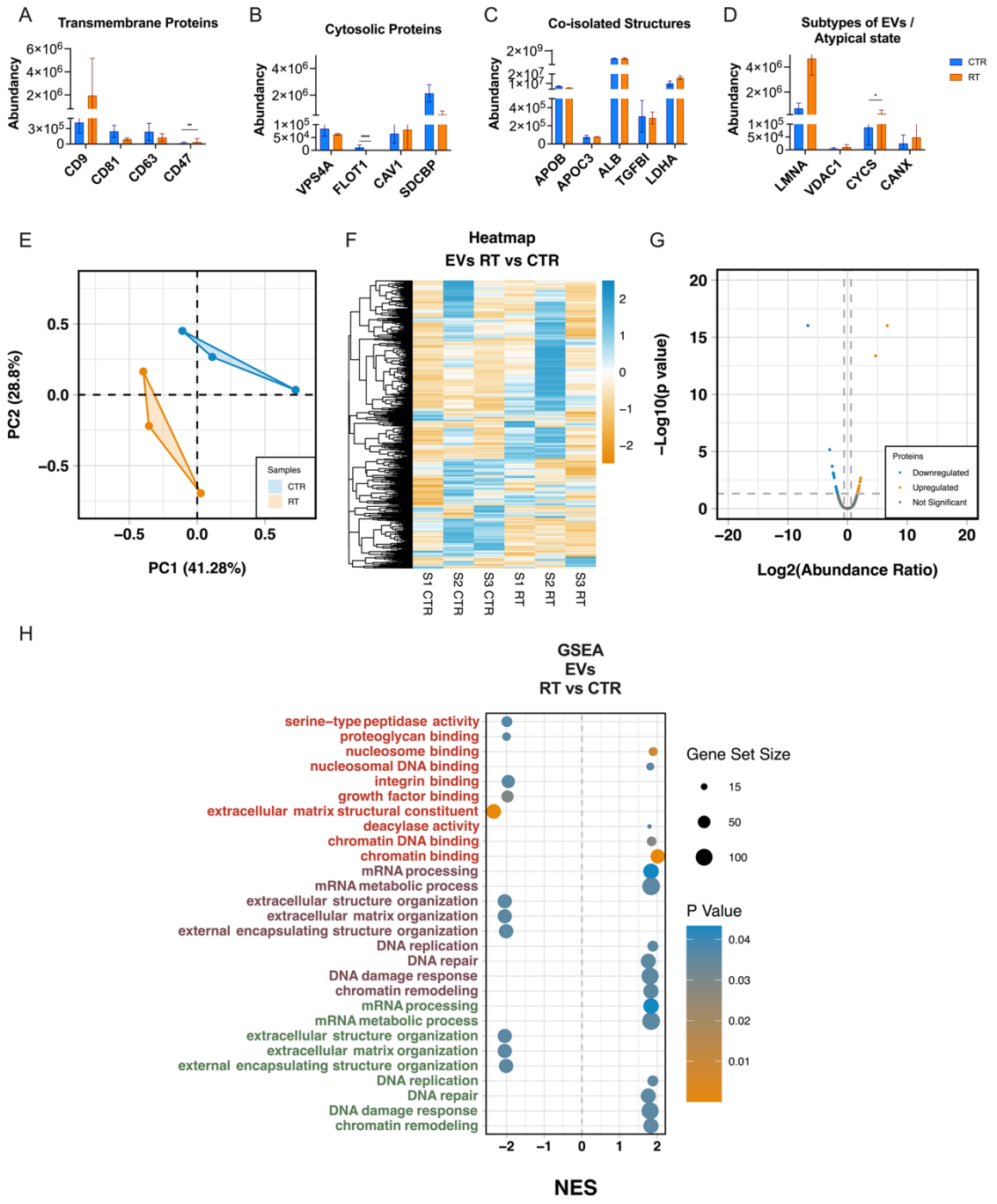


Figure 33 - Ionizing radiation impacts the extracellular vesicles proteomic profile in MDA-MB-231 3D models.

Tumor spheroids (TS) were exposed to 5 fractions of 5.2 Gy over 5 consecutive days (RT) or left without treatment (CTR). Extracellular vesicles (EVs) were isolated from conditioned medium (CM) 72 hours after the last irradiation (IR) and analysed through LC-MS/MS. **(A)**Transmembrane proteins, (**B**) cytosolic proteins (**C**) co-isolated structures and (**D**) subtypes of EVs / atypical states of EVS. **(E)** PCA analysis, **(F)** Heatmap of all proteins differently expressed between EVs normalized by Z-score and **(G)** Volcano plot for proteins upregulated, downregulated and not significantly expressed in CTR and RT conditions. **(H)** Gene set enrichment analysis (GSEA) performed for distinct biological processes, cellular components and molecular functions.

5. Discussion

5.1 Unveiling the RR signature of TNBC through 3D models

RT is a modality normally used in the treatment of TNBC which consists in the usage of high-energy IR. Continuous RT, which is normally applied in a clinical setting, can induce tumor RR ultimately leading to treatment failure. [37] Given the importance of this treatment to lower local recurrence rates in TNBC patients the scientific community has been focusing in the discovery of possible RR-signatures and radiosensitizing strategies to overcome this issue.[86–89] Currently many mechanisms have been associated with RR in TNBC involving both intrinsic and extrinsic mechanisms.[25] To investigate the cellular acquired mechanisms involved in this phenotype, we developed RR cell lines from two TNBC subtypes, MDA-MB-231 and MDA-MB-468, as well as from the murine cell line 4T1. MDA-MB-468 represents the BL1, one of the most common subtypes of TNBC, and MDA-MB-231 represent the MSL TNBC, one of the less common subtypes.[28] To validate the establishment of RR cell lines, clonogenic assays were performed. The increased capacity to develop colonies when exposed to higher doses of IR further confirmed the suitability of these as a promising platform to investigate IR-induced phenotypic adaptations.

Consistent with previous studies, the established RR cell lines developed demonstrated significantly reduced proliferation.[90] Interestingly the morphological alterations were cell line dependent given that MDA-MB-468 presented a more circular shape with an increased area and both MDA-MB-231 and 4T1 were more elongated in comparison with their parental counterparts. These findings suggest that the alterations associated with the RR phenotype may be specific to each TNBC subtype, resulting in distinct morphological characteristics. Actually, RR breast cancer cells have been described to display increased epithelial-to-mesenchymal transition phenotype and our RR cell lines, MDA-MB-231 RR and 4T1 RR, exhibit mesenchymal-like morphology however further confirmation is required.[91–93]

Among *in vitro* platforms, 3D models have gained increasing attention in radiobiology research due to their ability to more accurately recapitulate tumor architecture, cell–cell interactions, and key determinants of the RR phenotype as hypoxia.[25] Although 3D models more closely recapitulate the tumor microenvironment, their application in radiobiology research remains limited, with most studies still performed using conventional 2D cultures or *in vivo* models.[94] Previous studies within the RR field have demonstrated that 3D models exhibit enhanced resistance to RT in comparison with 2D platforms thus more faithfully recapitulating the TME.[95,96] Consistent with these findings, MDA-MB-231 and 4T1 cell lines exhibited greater RR under 3D culture conditions than under conventional 2D conditions, particularly at the acute time point of 24 hours post-IR. In contrast, MDA-MB-468 TS displayed a similar response under both culture conditions. Given the distinct morphological characteristics of these spheroids, it is plausible that the relatively greater compactness of 4T1 TS, together with the intermediate architecture of MDA-MB-231 TS, enhances cell–cell interactions and promotes the development of hypoxic regions, both of which are known contributors to RR. Conversely, the looser morphology of MDA-MB-468

TS may limit the establishment of these protective TME features, resulting in an IR response comparable to that observed in 2D cultures.

During ionizing radiation, multiple cellular signalling pathways are activated, leading to the induction of senescence, activation of cell cycle checkpoints, and DNA repair. Following RT-induced DNA damage, the DNA damage response (DDR) detects DNA lesions and activates cell cycle checkpoints, resulting in transient cell cycle arrest. This provides cells with sufficient time to repair damaged DNA, thereby promoting cell survival and potentially contributing to resistance to RT.[97] Following RT, both parental and RR TS cell lines exhibited a significant accumulation of cells in the G2/M phase at the acute time point, consistent with activation of the G2/M checkpoint in response to radiation-induced DNA damage. This transient cell cycle arrest is a well-established component of the DNA damage response, allowing cells time to repair damaged DNA before entering mitosis. However, by 72 hours post-irradiation, the RR cell lines had completely recovered (4T1 RR) or decreased (MDA-MB-231 RR, MDA-MB-468 RR) from G2/M phase, whereas the parental cells showed a more sustained accumulation. This suggests that RR cells may possess an enhanced ability to resolve DNA damage and re-enter the cell cycle more rapidly, potentially through more efficient DNA repair mechanisms or faster checkpoint recovery. The ability to escape prolonged G2/M arrest may provide a survival advantage following IR, thereby contributing to the RR phenotype. This phenotype is further supported by the γ-H2AX data. Although MDA-MB-231 RR and MDA-MB-468 RR cells exhibited increased γ-H2AX positivity only at 72 hours post-RT, MDA-MB-231 RR cells consistently showed a trend towards lower γ-H2AX levels than the parental cells. Together with the earlier recovery from G2/M arrest, these observations suggest that RR cells exhibit altered DNA damage response dynamics following irradiation. However, further studies are required to determine whether these differences reflect changes in DNA repair efficiency, DNA damage signalling, or other cellular processes. In contrast, neither the parental or 4T1 RR cell lines showed a significant increase in γ-H2AX following irradiation, suggesting a distinct DNA damage response in this model.

Another well-known mechanism of RR is cellular hypoxia. Soluble Factors, as HIF-1a have been seen to have a radioprotective mechanism associated with inhibition of apoptosis, support of cancer cells stemness and reprograming of metabolic pathways.[98] Interestingly, both MDA-MB-231 RR and MDA-MB-468 RR TS exhibited a significant reduction in ROS-positive cells, particularly at 72 hours following irradiation. Similarly, while parental 4T1 TS showed no significant changes in ROS levels after IR, RR 4T1 TS displayed a significant reduction compared with the 24 hours post-IR time point. These findings suggest that RR cells exhibit altered dynamics following IR, with lower intracellular ROS levels at later time points.

Overall, we successfully established RR platforms in both 2D and 3D settings that exhibit several characteristics associated with the RR phenotype. These models provide a valuable platform for investigating the biological mechanisms underlying radioresistance. Future studies should focus

on confirming the acquisition of a mesenchymal phenotype and elucidating the molecular pathways responsible for enhanced recovery from a possible IR-induced cell cycle arrest and hypoxia-associated adaptations that may contribute to radioresistance.

5.2 Establishment and Characterization of 3D Tumor Spheroids after Irradiation

Experimental models for studying breast cancer therapies are evolving rapidly, from traditional 2D cultures to more sophisticated systems that better mimic the tumor microenvironment.[99,100] RT represents one of the essential modalities for TNBC patients, reducing locoregional and distant recurrence. However, reliable 3D models to evaluate RT effects in TNBC remain limited. Therefore, robust *in vitro* platforms that allow the investigation of cellular and molecular RT effects is of utmost importance. Conventional 2D monolayer models have consistently shown uniform radiation exposure and largely homogeneous cellular responses, with well-documented effects such as DNA damage induction, reduced proliferation, apoptosis and immune checkpoint molecules expression.[101,102]

Despite of 2D models have been instrumental in identifying key mechanisms of radiosensitivity and resistance, they fail to capture spatial heterogeneity, oxygen and nutrient gradients, and zone-specific cellular responses (proliferation and stress adaptation) features that are intrinsic to solid tumors but absent in monolayer cultures, and therefore, cannot recapitulate layer-dependent effects induced by RT.[103,104] In this study, we established and characterized a 3D TNBC spheroid model to advance radiobiology research. Compared with conventional 2D cultures, spheroids displayed slower proliferation, altered lipid metabolism, and distinct cell cycle profiles, reflecting the existence of proliferative, quiescent, and necrotic zones. These features mimic *in vivo* tumor heterogeneity and provide a physiologically relevant model for analysing RT responses.[51]

Most radiobiology studies are performed with single doses of RT, which does not replicate clinical therapeutic schemes.[105] To fill this gap, a recent study has shown efforts to better illustrate the impact of fractionated RT on MDA-MB-231 cells immunogenicity.[101] Here, we show that, together with preclinical data, immunogenic cell death induction is attributed to hypofractionated IR [106,107] rather than high single dose RT, which is more clinically applied for RT of breast cancer. Also, immune suppressive checkpoint molecules were significantly more upregulated on radioresistant MDA-MB-231 clones after 5x5.2 Gy. However, these experiments were performed in 2D monolayers. To the best of our knowledge, this is the first study evaluating an hypofractionated IR scheme of 5x5.2 Gy in 3D spheroids, currently used for TNBC patients.[105]

This treatment decreased spheroids viability, increased DNA damage and promoted cell cycle arrest.[108] Notably, surviving cells presented a bigger area, mainly due to the increase of the nucleus, which might be related with G2/M phase arrest as well as chromatin changes inherent

to IR.[109,110] Proteomic analysis confirmed upregulated pathways related to nuclear division, organelle fission and nuclear chromosome segregation, including mitotic kinases (AURKA, AURKB, PLK1, CDK1), kinesins (KIF family), cyclins (CCNB1, CCNB2), cohesion/ condensing complex components (CDCA5, CDCA8, SPC25, NUF2, SKA3), and proliferation markers, as MKI67, consistent with G2/M arrest.[111] Importantly, proteomic profiling was designed to capture not only immediate radiation-induced events, but also the sustained molecular adaptations that emerge once early stress responses have stabilized. The 72 hours timepoint therefore represents a biologically meaningful window in which transient signalling fluctuations have subsided, allowing the detection of more persistent changes in the cellular behaviour (protein abundance, pathway modulation, etc). These stable signatures are more informative for understanding longer-term radiobiological effects in 3D spheroids. For these reasons, the proteomics analysis was intentionally performed at 72 hours post-IR, while earlier assays at 24 hours were used to characterize acute responses.

Then, ultrastructural analysis considering spheroids periphery, middle layer and central core was performed. The increase in cell–cell contacts at the periphery could be related to increased direct communication between cancer cells as an attempt to survive[112] and to maintain the collective spheroid structure. However, it is important to note that this finding was only possible by using 3D techniques, since it better illustrates cell–cell contacts in the tumor. Accordingly, some uniquely expressed proteins were found in irradiated spheroids (**Supplementary Table 2**) related with the cad herein superfamily desmocollin-1 (DSC1), mediating desmosomal adhesion between epithelial cells, and MICAL-like protein 2 (MICALL2), controlling tight junction dynamics.[113,114] Mitochondrial dysfunction is a mechanism leading to a malignant phenotype and therapy resistance.[115,116] Indeed, dysfunctional mitochondria release dangerous signals, helping tumor cells to overcome RT- induced damage.[117] In a previous study, monolayer cultures of HMEC- 1 endothelial cells had a different impact of low dose compared with high dose RT in mitochondrial morphology and function. While high doses increased mitochondrial dysfunction and fragmentation, reducing cell survival, low doses (0.25 Gy to 0.5 Gy) induced mitochondria elongation and cell survival.[118] In this study, hypofractionated RT increased mitochondrial content without changes in their morphology. This increase was accompanied by increased ATP molecules in live cells and was further supported by the upregulation of pathways related to mitotic nuclear division, oxidative phosphorylation, and ATP synthesis in RT-exposed spheroids. Importantly, mitochondria-related proteins, as ATP5F1E, NDUFs, and UQCRB, support energy production and ROS control for cell repair by dysfunctional mitochondria, as part of the RT-induced stress response.[119]

Increase of the LDs in surviving cells, especially at the periphery, suggests lipid metabolism changes that might prevent ferroptosis. Indeed, a previous study using 2D *in vitro* models described that cell cycle arrest suppresses ferroptosis by promoting lipid droplet formation to sequester excessive unsaturated fatty acids.[120] We hypothesize that IR-induced cell cycle arrest

drives de expression of lipid-related proteins, as CROT and APOL3, specifically in irradiated TS. These proteins may sustain fatty acids oxidation in the accumulated mitochondria, thus supporting energy production[121,122], while also promoting mitophagy of damaged mitochondria to maintain cellular homeostasis[123] and prevent ferroptosis.

Previous 2D studies have reported that RT can trigger ER stress, leading to the activation of the unfolded protein response (UPR) signalling pathway. Consequently, UPR can initiate autophagy, a process that clears damaged proteins and organelles and contributes to cell survival during RT.[119,124] The increase of ER and autophagic vesicles support the upregulation of lysosome-related pathways. Indeed, we hypothesize that exclusive proteins altered in the irradiated TS, as glypican-1 (GPC1), FA Complementation Group I (FANCI) and Drosha Ribonuclease III (DROSHA) are indirectly related with ER stress, which might induce UPR and contribute to cell damage repair.[125–127] Also, the subcellular location of the ER close to the plasma membrane in irradiated spheroids is, to the best of our knowledge, the first time reported after IR-induced stress. Previous reports have shown that the contact between ER and the plasma membrane facilitate intracellular Ca 2+ signalling and control lipid trafficking, as a response to ER stress.[128,129]

Intriguingly, RT mainly affected the spheroids periphery, where oxygen availability facilitates ROS generation and DNA damage, while inner layers exhibited limited responses, possibly due to hypoxia and reduced radiation penetration. Indeed, a recent study comparing RT response between 2D and 3D models confirms a lower radiosensitivity in spheroids than in monolayers of prostate and breast cancer cell lines, however the possible reasons for this difference are not explored.[103] The present study further highlights the importance of the architecture of 3D models, that consider the presence of a more resistant hypoxic core and a sensitive outer layer, to identify approaches that enhance RT efficacy throughout the tumor mass. While spheroids mimic the layered architecture typically observed *in vivo*, including proliferative outer layers, intermediate quiescent zones, and inner hypoxic or necrotic regions, and recapitulates key aspects of RT response, they still present some limitations. First, spheroids are generated from a single cell line and therefore cannot reproduce the full genetic and cellular heterogeneity of epithelial tumors. Second, the limited culture duration of the 3D spheroids in the MDA-MB-231 cell line restricted the evaluation of late RT responses and long-term radio resistance mechanisms. It would be of further interest to explore how spheroid age influences the response to RT, considering its known impact on proteomic and metabolic profiles.[130] Third, the model lacks immune and stromal components, which are known to significantly in fluence radiosensitivity. Future studies incorporating immune cells, fibroblasts, or patient-derived cells will be necessary to fully capture the complexity of TNBC response to RT. In addition, expanding this work to include multiple cell lines representing different TNBC subtypes, such as basal-like models, and patient-derived models would improve biological representation and validation. Finally, integration of single-cell proteomics into multicellular spheroid systems may provide deeper insight into intra-spheroid

heterogeneity and zone-specific radioresistance mechanisms, as it was achieved by electron microscopy.

Overall, this 3D TNBC spheroid model provides a physiologically relevant system for investigating the cellular, molecular, and ultrastructural effects of RT. By integrating proteomic and ultrastructural data, this model reveals the interplay between mitochondrial activity, lipid metabolism, ER stress, and cell adhesion in the context of radiation-induced damage and survival. The spatially resolved nature of the analysis underscores how tumor heterogeneity, including peripheral DNA damage, hypoxia and proliferation, influences therapeutic outcomes. Therefore, this work highlights the necessity of advancing radiobiology studies toward more complex and physiologically relevant 3D models, rather than relying on conventional 2D monolayer cultures, which fail to recapitulate the oxygen and nutrient gradients known to critically influence RT response.[103,131] To the best of our knowledge, this is the first study to directly address how 3D tumor architecture and spatial organization modulate cellular responses to clinically relevant RT. In conclusion, this 3D model represents a significant step towards more predictive and translational approaches in cancer radiobiology and therapeutic innovation.

5.3 The Proteomic Landscape of TNBC Spheroids-Derived Extracellular Vesicles

RT is known to profoundly influence intercellular communication within the TME. Radiation-induced signals can be transmitted from irradiated cells to neighbouring or distant non-irradiated cells, eliciting biological responses despite the absence of direct radiation exposure. This phenomenon, known as the RIBE, is increasingly recognized as an important contributor to treatment response. Among the mediators implicated in RIBE, EVs have emerged as key regulators of intercellular communication. Indeed, RT has been shown to increase EV secretion and remodel their molecular cargo across multiple cancer types, thereby influencing the biological behaviour of recipient cells and potentially contributing to the acquisition of radioresistance.[132]

Within EVs, exosomes are highlighted as carriers of multiple types of molecules: nucleic acids (DNA and RNA), proteins, lipids and metabolites. RT induces exosome release in a radiation type, dose, time and cell type-dependent manners, primarily through the activation of stress induced pathways that regulate exosomes secretion. Consequently, these exosomes have been shown to alter epigenetic functions within recipient cells and are enriched in a high number of small noncoding RNAs (mainly miRNAs) thus altering gene expression.[133] Despite these findings, a significant gap of knowledge remains regarding the specific EVs cargo that induces these changes. These findings provide an opportunity to study the molecular alterations induced by RT in EVs and possibly identify a EVs-based signature associated with RT response.

An increasing number of high-quality EV isolation techniques have been described.[134] However, each technique has limitations and the heterogeneity of EVs size together with their relativity low abundance compared with components of other biological fluids make their isolation particularly challenging. These involve reduced solubility approaches, UC, density gradient separation, SEC, microfluids, magnetic bead-based methods and UF. UC is one of the most used techniques due to its adaptability to large volumes helping the increase of EVs yield and low costs. However, this technique has some limitations associated with aggregation, EVs degradation and fission of larger EVs due to the centrifugal force required. SEC is a size-based method referred as gel filtration. EVs are separated based on their ability to pass or not through the pores of different sizes in a chromatography column. While this technique aids in separating small from large EVs a key drawback is co-elution of similar size lipoproteins and large protein aggregates. Lastly UF uses a membrane filter of pore size with specific molecular cutoffs (10, 50 or 100 kDa) that limits the passage or flow of contaminants. Some limitations involve the EVs damage and particles aggregation which might impact EVs yield.[134,135] Taking in consideration the costs and EVs yield provided by all the techniques available, we selected ultracentrifugation and size exclusion chromatography for EVs isolation.

TEM analysis revealed that SEC isolated EVs together with an increased number of contaminants. Contrary, UC isolated particles with low to undetectable levels of proteins. This issue is likely associated with the impact of continued exposure to high centrifugal force on EVs lipid membrane layer. As previously discussed, this process may alter and damage the EVs membrane-associated proteins. Hence, considering the significant differences between these two techniques, we combined steps of both methods by performing differential ultracentrifugation without the washing step, followed by ultrafiltration with a 10kDa cut off. This strategy enables the isolation of high pure EVs with and increased yield in a cost effective and time wise manner. To the best of our knowledge, this was the first time that this strategy was reported. In addition, TEM analysis revealed a lower number of contaminants in comparison with the SEC technique. Furthermore, the number of particles isolated and proteins levels seemed to be preserved in comparison with the UC technique. Taking in consideration the main results obtained the UC + UF method was selected as isolation method for our EVs.

EV isolation by UC+UF method revealed an increased number of EVs released by MDA-MB-231 spheroids following irradiation. These findings are consistent with previous reports demonstrating that irradiation enhances EV release. For example, Lisa Mustschelknaus *et al*. reported a significant increase in EV secretion following RT in 2D Squamous Head and Neck Cancer models.[136] Another study, in prostate cancer, also demonstrated an increased secretion of exosomes after RT.[137] Finally, Lee Y *et al* isolated EVs from MDA-MB-231 and MDA-MB-231 RR cells in a 2D *in vitro* setting and characterized their ability to promote RR mechanisms in the parental cell line upon treatment with EVs derived from the RR MDA-MB-231.[138] Nevertheless,

to the best of our knowledge, this is the first study that used 3D models to characterize the EVs cargo after a clinically relevant RT scheme.

Proteomic analysis revealed a distinct molecular signature of EVs following RT. GSEA identified an upregulation of pathways associated with DNA repair, nucleosomal DNA, and chromatin binding after RT, whereas pathways related to ECM constituents were downregulated. These findings suggest that the small population of surviving cells may be releasing EV-mediated survival signals following RT, attempting the promotion of persistence and adaptation of the surrounding cells. In support of this hypothesis, proteins exclusively detected in EVs after RT, such as DNA topoisomerase II alpha (TOP2A) or kinesin family member 11 (KIF11), may be released by the MDA-MB-231 cells as part of a cellular response to radiation-induced damage (**Supplementary Table 6**). Indeed, several studies have associated TOP2A and KIF11 overexpression with radioresistance and poor therapeutic response across multiple cancer types. Their enrichment in EVs following RT suggests that these proteins may contribute to the transfer of pro-survival signals and adaptive responses associated with radioresistance. [139–143]

6. Conclusions

In this thesis, the relevance of 3D TS was assessed for radiobiology studies, as well as for the identification of novel biomarkers of RT response through EVs.

Our results demonstrated that the RR cell lines exhibit distinct phenotypic profiles compared with their parental counterparts, although these phenotypes are highly heterogeneous. Specifically, MDA-MB-468 RR cells displayed a more rounded morphology, whereas both MDA-MB-231 RR and 4T1 RR cells exhibited a more elongated morphology, suggesting a more mesenchymal phenotype. Interestingly, despite their distinct morphological features, all RR cell lines exhibited a lower proliferation rate than their parental counterparts across all TNBC subtypes. 3D TS derived from both parental and RR cell lines exhibited distinct phenotypes following exposure to a clinically relevant IR scheme of 5 fractions of 5.2 Gy. Following the cumulative IR dose, an acute increase in the G2/M cell population, accompanied by a corresponding decrease in the G1 phase, was observed in both parental and RR spheroids. However, at 72 hours post-RT, RR spheroids exhibited a complete or partial reduction in the G2/M population together with reduced intracellular ROS accumulation, consistent with the recovery of cell cycle progression following irradiation.

Furthermore, the MDA-MB-231 TS demonstrated decreased spheroids viability, while increasing cell size and number of organelles, as mitochondria, lipid droplets, endoplasmic reticulum and autophagic vesicles in surviving cells. The peripheral layer of the spheroids exhibited the most pronounced organelle alterations following RT. Proteomic profiling revealed upregulated pathways linked to cell cycle progression and organelle fission, supporting G2/M cell cycle arrest. Hypothesizing that, to balance the DNA damage and oxidative stress induced by RT, cancer cells undergo cell cycle arrest, leading to increased cell size and organelle content.

Afterward through UC+UF EVs produced by MDA-MB-231 TS were successfully isolated and confirmed via EVs specific markers (e.g., CD81, CD63, ALIX, FLOT1) and observed through TEM. The EV profile was also significantly altered following treatment, with an increase in both EV production and size after RT. Proteomic analysis revealed the upregulation of pathways involved in DNA repair, as well as nucleosome and chromatin binding, suggesting the emergence of a survival-associated signature in EVs released by the small population of cells that survived RT. These findings indicate that EV-mediated signalling may contribute to the development or maintenance of RR mechanisms.

Overall, these TNBC 3D models represent a promising platform for radiobiology research and for the high-throughput screening of combination therapies aimed at overcoming radioresistance. Building on these findings, future studies should focus on increasing the complexity of the tumor spheroids by incorporating stromal cell populations to better recapitulate the tumor microenvironment. Such advanced models could provide valuable insights into the mechanisms underlying RR and facilitate the identification of predictive biomarkers and therapeutic targets.

Accordingly, our hypothesis is that TNBC patients who experience locoregional or distant disease recurrence following RT exhibit a distinct blood exosome transcriptomic and proteomic profile. This unique molecular signature may serve as a biomarker of radioresistance and a predictive indicator of RT response. Furthermore, it may enable the identification of novel therapeutic targets for pharmacological intervention, either as alternative treatment strategies or in combination with RT to enhance treatment efficacy.

7. Referencies

1. Filho, A. M. *et al.* The GLOBOCAN 2022 cancer estimates: Data sources, methods, and a snapshot of the cancer burden worldwide. *Int. J. Cancer* **156**, 1336–1346 (2025).
2. Sha, R., Kong, X. M., Li, X. Y. & Wang, Y. B. Global burden of breast cancer and attributable risk factors in 204 countries and territories, from 1990 to 2021: results from the Global Burden of Disease Study 2021. *Biomark. Res.* **12**, (2024).
3. Zhang, Y. *et al.* Global burden of female breast cancer: new estimates in 2022, temporal trend and future projections up to 2050 based on the latest release from GLOBOCAN. *Journal of the National Cancer Center* **5**, 287–296 (2025).
4. Filho, A. M. *et al.* The GLOBOCAN 2022 cancer estimates: Data sources, methods, and a snapshot of the cancer burden worldwide. *Int. J. Cancer* **156**, 1336–1346 (2025).
5. Smolarz, B., Zadrożna Nowak, A. & Romanowicz, H. Breast Cancer—Epidemiology, Classification, Pathogenesis and Treatment (Review of Literature). *Cancers* vol. 14 Preprint at https://doi.org/10.3390/cancers14102569 (2022).
6. Łukasiewicz, S. *et al.* Breast cancer—epidemiology, risk factors, classification, prognostic markers, and current treatment strategies—An updated review. *Cancers* vol. 13 Preprint at https://doi.org/10.3390/cancers13174287 (2021).
7. McCarthy, A. M. *et al.* Relationship of established risk factors with breast cancer subtypes. *Cancer Med.* **10**, 6456–6467 (2021).
8. Obeagu, E. I. & Obeagu, G. U. Breast cancer: A review of risk factors and diagnosis. *Medicine (United States)* **103**, E36905 (2024).
9. Barba, D. *et al.* Breast cancer, screening and diagnostic tools: All you need to know. *Critical Reviews in Oncology/Hematology* vol. 157 Preprint at https://doi.org/10.1016/j.critrevonc.2020.103174 (2021).
10. Nicosia, L. *et al.* History of Mammography: Analysis of Breast Imaging Diagnostic Achievements over the Last Century. *Healthcare (Switzerland)* vol. 11 Preprint at https://doi.org/10.3390/healthcare11111596 (2023).
11. L Tabár *et al. Reduction in Mortality from Breast Cancer after Mass Screening with Mammography*. (1985).
12. Katsika, L. *et al.* Screening for Breast Cancer: A Comparative Review of Guidelines. *Life* vol. 14 Preprint at https://doi.org/10.3390/life14060777 (2024).
13. Eisemann, N. *et al.* Nationwide real-world implementation of AI for cancer detection in population-based mammography screening. *Nat. Med.* **31**, 917–924 (2025).
14. Waks, A. G. & Winer, E. P. Breast Cancer Treatment: A Review. *JAMA - Journal of the American Medical Association* vol. 321 288–300 Preprint at https://doi.org/10.1001/jama.2018.19323 (2019).
15. Feng, Y. *et al.* Breast cancer development and progression: Risk factors, cancer stem cells, signaling pathways, genomics, and molecular pathogenesis. *Genes and Diseases* vol. 5 77–106 Preprint at https://doi.org/10.1016/j.gendis.2018.05.001 (2018).
16. Mosly, D., Turnbull, A., Sims, A., Ward, C. & Langdon, S. Predictive markers of endocrine response in breast cancer. *World J. Exp. Med.* **8**, 1–7 (2018).

17. Dai, X., Xiang, L., Li, T. & Bai, Z. Cancer hallmarks, biomarkers and breast cancer molecular subtypes. *Journal of Cancer* vol. 7 1281–1294 Preprint at https://doi.org/10.7150/jca.13141 (2016).
18. Vagia, E., Mahalingam, D. & Cristofanilli, M. The landscape of targeted therapies in TNBC. *Cancers* vol. 12 Preprint at https://doi.org/10.3390/cancers12040916 (2020).
19. Dai, X., Xiang, L., Li, T. & Bai, Z. Cancer hallmarks, biomarkers and breast cancer molecular subtypes. *Journal of Cancer* vol. 7 1281–1294 Preprint at https://doi.org/10.7150/jca.13141 (2016).
20. Gao, J. J. & Swain, S. M. Luminal A Breast Cancer and Molecular Assays: A Review. *Oncologist* **23**, 556–565 (2018).
21. Li, Z.-H., Hu, P.-H., Tu, J.-H. & Yu, N.-S. *Luminal B Breast Cancer: Patterns of Recurrence and Clinical Outcome*. vol. 7 www.impactjournals.com/oncotarget (2016).
22. Johnson, K. S., Conant, E. F. & Soo, M. S. Molecular Subtypes of Breast Cancer: A Review for Breast Radiologists. *J. Breast Imaging* **3**, 12–24 (2021).
23. Torres Quintas, S., Canha-Borges, A., Oliveira, M. J., Sarmento, B. & Castro, F. Special Issue: Nanotherapeutics in Women's Health Emerging Nanotechnologies for Triple-Negative Breast Cancer Treatment. *Small* vol. 20 Preprint at https://doi.org/10.1002/smll.202300666 (2024).
24. Karim, A. M. *et al.* Triple-negative breast cancer: epidemiology, molecular mechanisms, and modern vaccine-based treatment strategies. *Biochemical Pharmacology* vol. 212 Preprint at https://doi.org/10.1016/j.bcp.2023.115545 (2023).
25. Canha-Borges, A. *et al.* Emerging mechanisms of triple-negative breast cancer radioresistance: Interplay between cancer cell mechanisms and the tumor immune microenvironment. *Cancer Treatment Reviews* vol. 140 Preprint at https://doi.org/10.1016/j.ctrv.2025.103026 (2025).
26. Yin, L., Duan, J. J., Bian, X. W. & Yu, S. C. Triple-negative breast cancer molecular subtyping and treatment progress. *Breast Cancer Research* vol. 22 Preprint at https://doi.org/10.1186/s13058-020-01296-5 (2020).
27. Hu, Y., Wang, C., Liang, H., Li, J. & Yang, Q. The treatment landscape of triple-negative breast cancer. *Medical Oncology* vol. 41 Preprint at https://doi.org/10.1007/s12032-024-02456-9 (2024).
28. Lehmann, B. D. *et al.* Identification of human triple-negative breast cancer subtypes and preclinical models for selection of targeted therapies. *Journal of Clinical Investigation* **121**, 2750–2767 (2011).
29. Baranova, A. *et al.* Triple-negative breast cancer: current treatment strategies and factors of negative prognosis. *Journal of Medicine and Life* vol. 2022 153–161 Preprint at https://doi.org/10.25122/jml-2021-0108 (2022).
30. Poggio, F. *et al.* Platinum-based neoadjuvant chemotherapy in triple-negative breast cancer: A systematic review and meta-analysis. *Annals of Oncology* vol. 29 1497–1508 Preprint at https://doi.org/10.1093/annonc/mdy127 (2018).

31. Liu, G., Zhang, Y. & Huang, Y. Triple-Negative Breast Cancer Treatment Advancements: A Review of Evolving Strategies. *European Journal of Cancer Care* vol. 2024 Preprint at https://doi.org/10.1155/2024/8299502 (2024).
32. Yao, Y., Chu, Y., Xu, B., Hu, Q. & Song, Q. Radiotherapy after surgery has significant survival benefits for patients with triple-negative breast cancer. *Cancer Med.* **8**, 554–563 (2019).
33. Xing, J. L. & Stea, B. Molecular mechanisms of sensitivity and resistance to radiotherapy. *Clinical and Experimental Metastasis* vol. 41 517–524 Preprint at https://doi.org/10.1007/s10585-023-10260-4 (2024).
34. Alzibdeh, A., Abuhijlih, R. & Abuhijla, F. Breast cancer radiobiology: The renaissance of whole breast radiation fractionation (Review). *Molecular and Clinical Oncology* vol. 21 Preprint at https://doi.org/10.3892/mco.2024.2795 (2024).
35. Tejada Ortigosa, E. M., Ollinger Casin, I., Gaztelu Blanco, I., Muñiz Romero, G. & de Haro Piedra, R. Ultra-hypofractionated 5-fraction radiation therapy for early breast cancer into whole breast and regional nodes: experience in a tertiary hospital. *Clinical and Translational Oncology* **27**, 3135–3143 (2025).
36. Wang, Y. *et al.* Mechanisms of radioresistance and radiosensitization strategies for Triple Negative Breast Cancer. *Translational Oncology* vol. 55 Preprint at https://doi.org/10.1016/j.tranon.2025.102351 (2025).
37. Wang, Y. *et al.* Mechanisms of radioresistance and radiosensitization strategies for Triple Negative Breast Cancer. *Translational Oncology* vol. 55 Preprint at https://doi.org/10.1016/j.tranon.2025.102351 (2025).
38. Huang, R. X. & Zhou, P. K. DNA damage response signaling pathways and targets for radiotherapy sensitization in cancer. *Signal Transduction and Targeted Therapy* vol. 5 Preprint at https://doi.org/10.1038/s41392-020-0150-x (2020).
39. Wu, Y., Song, Y., Wang, R. & Wang, T. Molecular mechanisms of tumor resistance to radiotherapy. *Molecular Cancer* vol. 22 Preprint at https://doi.org/10.1186/s12943-023-01801-2 (2023).
40. Payton, C., Pang, L. Y., Gray, M. & Argyle, D. J. Exosomes derived from radioresistant breast cancer cells promote therapeutic resistance in naïve recipient cells. *J. Pers. Med.* **11**, (2021).
41. Das, K. *et al.* Extracellular Vesicles in Triple–Negative Breast Cancer: Immune Regulation, Biomarkers, and Immunotherapeutic Potential. *Cancers* vol. 15 Preprint at https://doi.org/10.3390/cancers15194879 (2023).
42. Kumar, M. A. *et al.* Extracellular vesicles as tools and targets in therapy for diseases. *Signal Transduction and Targeted Therapy* vol. 9 Preprint at https://doi.org/10.1038/s41392-024-01735-1 (2024).
43. Latifkar, A., Hur, Y. H., Sanchez, J. C., Cerione, R. A. & Antonyak, M. A. New insights into extracellular vesicle biogenesis and function. *Journal of Cell Science* vol. 132 Preprint at https://doi.org/10.1242/JCS.222406 (2019).

44. Yu, L. *et al.* Apoptotic bodies: bioactive treasure left behind by the dying cells with robust diagnostic and therapeutic application potentials. *Journal of Nanobiotechnology* vol. 21 Preprint at https://doi.org/10.1186/s12951-023-01969-1 (2023).
45. Dong, M., Liu, Q., Xu, Y. & Zhang, Q. Extracellular Vesicles: The Landscape in the Progression, Diagnosis, and Treatment of Triple-Negative Breast Cancer. *Frontiers in Cell and Developmental Biology* vol. 10 Preprint at https://doi.org/10.3389/fcell.2022.842898 (2022).
46. Coelho, M. O., Quintas, S. T., Sarmento, B., De Wever, O. & Castro, F. Engineered dendritic cells-derived extracellular vesicles for cancer immunotherapy. *Journal of Controlled Release* vol. 381 Preprint at https://doi.org/10.1016/j.jconrel.2025.113620 (2025).
47. Kalluri, R. & McAndrews, K. M. The role of extracellular vesicles in cancer. *Cell* vol. 186 1610–1626 Preprint at https://doi.org/10.1016/j.cell.2023.03.010 (2023).
48. Ozawa, P. M. M. *et al.* Extracellular vesicles from triple-negative breast cancer cells promote proliferation and drug resistance in non-tumorigenic breast cells. *Breast Cancer Res. Treat.* **172**, 713–723 (2018).
49. Canha-Borges, A. *et al.* Radiotherapy induces layer-specific molecular and ultrastructural alterations in triple-negative breast cancer spheroids. *Radiotherapy and Oncology* **219**, (2026).
50. Hoarau-Véchot, J., Rafii, A., Touboul, C. & Pasquier, J. Halfway between 2D and animal models: Are 3D cultures the ideal tool to study cancer-microenvironment interactions? *International Journal of Molecular Sciences* vol. 19 Preprint at https://doi.org/10.3390/ijms19010181 (2018).
51. Kapałczyńska, M. *et al.* 2D and 3D cell cultures – a comparison of different types of cancer cell cultures. *Archives of Medical Science* **14**, 910–919 (2018).
52. Zanoni, M. *et al.* 3D tumor spheroid models for in vitro therapeutic screening: A systematic approach to enhance the biological relevance of data obtained. *Sci. Rep.* **6**, (2016).
53. Pinto, B., Henriques, A. C., Silva, P. M. A. & Bousbaa, H. Three-dimensional spheroids as in vitro preclinical models for cancer research. *Pharmaceutics* vol. 12 1–38 Preprint at https://doi.org/10.3390/pharmaceutics12121186 (2020).
54. Liverani, C. *et al.* A biomimetic 3D model of hypoxia-driven cancer progression. *Sci. Rep.* **9**, (2019).
55. Wishart, G., Gupta, P., Schettino, G., Nisbet, A. & Velliou, E. *3d Tissue Models as Tools for Radiotherapy Screening for Pancreatic Cancer 1,2*. *Radiol* vol. 94 https://academic.oup.com/bjr/article/94/1120/20201397/7452392 (2021).
56. Zhou, Z.-R. *et al.* Building radiation-resistant model in triple-negative breast cancer to screen radioresistance-related molecular markers. *Ann. Transl. Med.* **8**, 108–108 (2020).
57. Yu, G. Thirteen years of clusterProfiler. *Innovation* vol. 5 Preprint at https://doi.org/10.1016/j.xinn.2024.100722 (2024).

58. Yin, L., Duan, J. J., Bian, X. W. & Yu, S. C. Triple-negative breast cancer molecular subtyping and treatment progress. *Breast Cancer Research* vol. 22 Preprint at https://doi.org/10.1186/s13058-020-01296-5 (2020).
59. Hoarau-Véchot, J., Rafii, A., Touboul, C. & Pasquier, J. Halfway between 2D and animal models: Are 3D cultures the ideal tool to study cancer-microenvironment interactions? *International Journal of Molecular Sciences* vol. 19 Preprint at https://doi.org/10.3390/ijms19010181 (2018).
60. Dickey, J. S. *et al.* H2AX: Functional roles and potential applications. *Chromosoma* vol. 118 683–692 Preprint at https://doi.org/10.1007/s00412-009-0234-4 (2009).
61. Białkowska, K., Komorowski, P., Bryszewska, M. & Miłowska, K. Spheroids as a type of three-dimensional cell cultures—examples of methods of preparation and the most important application. *International Journal of Molecular Sciences* vol. 21 1–17 Preprint at https://doi.org/10.3390/ijms21176225 (2020).
62. Shimura, T. Mitochondrial Signaling Pathways Associated with DNA Damage Responses. *International Journal of Molecular Sciences* vol. 24 Preprint at https://doi.org/10.3390/ijms24076128 (2023).
63. De Martino, M. *et al.* Radiation therapy promotes unsaturated fatty acids to maintain survival of glioblastoma. Preprint at https://doi.org/10.1101/2022.06.01.494338 (2022).
64. Yang, P. *et al.* Ionizing radiation downregulates estradiol synthesis via endoplasmic reticulum stress and inhibits the proliferation of estrogen receptor-positive breast cancer cells. *Cell Death Dis.* **12**, (2021).
65. Almanza, A. *et al.* Endoplasmic reticulum stress signalling – from basic mechanisms to clinical applications. *FEBS Journal* vol. 286 241–278 Preprint at https://doi.org/10.1111/febs.14608 (2019).
66. Yorimitsu, T., Nair, U., Yang, Z. & Klionsky, D. J. Endoplasmic reticulum stress triggers autophagy. *Journal of Biological Chemistry* **281**, 30299–30304 (2006).
67. Wang, R. *et al.* LncRNA WEE2-AS1 promotes proliferation and inhibits apoptosis in triple negative breast cancer cells via regulating miR-32-5p/TOB1 axis. *Biochem. Biophys. Res. Commun.* **526**, 1005–1012 (2020).
68. Chen, S. *et al.* Rescue effects in radiobiology: Unirradiated bystander cells assist irradiated cells through intercellular signal feedback. *Mutation Research - Fundamental and Molecular Mechanisms of Mutagenesis* **706**, 59–64 (2011).
69. Ariyoshi, K. *et al.* Radiation-Induced Bystander Effect is Mediated by Mitochondrial DNA in Exosome-Like Vesicles. *Sci. Rep.* **9**, (2019).
70. Yang, Z. *et al.* The emerging role of exosomes in radiotherapy. *Cell Communication and Signaling* vol. 20 Preprint at https://doi.org/10.1186/s12964-022-00986-1 (2022).
71. Heeran, A. B., Berrigan, H. P. & O'Sullivan, J. The Radiation-Induced Bystander Effect (RIBE) and its Connections with the Hallmarks of Cancer. *Radiation Research* vol. 192 668–679 Preprint at https://doi.org/10.1667/RR15489.1 (2019).

72. Kalluri, R. The biology and function of exosomes in cancer. *Journal of Clinical Investigation* vol. 126 1208–1215 Preprint at https://doi.org/10.1172/JCI81135 (2016).
73. Al-Mayah, A. *et al.* The non-targeted effects of radiation are perpetuated by exosomes. *Mutation Research - Fundamental and Molecular Mechanisms of Mutagenesis* **772**, 38–45 (2015).
74. Cagatay, S. T. *et al.* Phenotypic and functional characteristics of exosomes derived from irradiated mouse organs and their role in the mechanisms driving non-targeted effects. *Int. J. Mol. Sci.* **21**, 1–25 (2020).
75. Bagheri, H. S. *et al.* Low-level laser irradiation at a high power intensity increased human endothelial cell exosome secretion via Wnt signaling. *Lasers Med. Sci.* **33**, 1131–1145 (2018).
76. Jabbari, N., Nawaz, M. & Rezaie, J. Ionizing radiation increases the activity of exosomal secretory pathway in MCF-7 human breast cancer cells: A possible way to communicate resistance against radiotherapy. *Int. J. Mol. Sci.* **20**, (2019).
77. Zhang, X. *et al.* Exosomes in cancer: Small particle, big player. *Journal of Hematology and Oncology* vol. 8 Preprint at https://doi.org/10.1186/s13045-015-0181-x (2015).
78. Kalluri, R. & LeBleu, V. S. The biology, function, and biomedical applications of exosomes. *Science* vol. 367 Preprint at https://doi.org/10.1126/science.aau6977 (2020).
79. Batista, I. A., Quintas, S. T. & Melo, S. A. The interplay of exosomes and NK cells in cancer biology. *Cancers* vol. 13 1–24 Preprint at https://doi.org/10.3390/cancers13030473 (2021).
80. De Sousa, K. P. *et al.* Isolation and characterization of extracellular vesicles and future directions in diagnosis and therapy. *Wiley Interdisciplinary Reviews: Nanomedicine and Nanobiotechnology* vol. 15 Preprint at https://doi.org/10.1002/wnan.1835 (2023).
81. Muttiah, B., Ng, S. L., Lokanathan, Y., Ng, M. H. & Law, J. X. Extracellular Vesicles in Breast Cancer: From Intercellular Communication to Therapeutic Opportunities. *Pharmaceutics* vol. 16 Preprint at https://doi.org/10.3390/pharmaceutics16050654 (2024).
82. Jeppesen, D. K., Zhang, Q., Franklin, J. L. & Coffey, R. J. Extracellular vesicles and nanoparticles: emerging complexities. *Trends in Cell Biology* vol. 33 667–681 Preprint at https://doi.org/10.1016/j.tcb.2023.01.002 (2023).
83. Zaborowski, M. P., Balaj, L., Breakefield, X. O. & Lai, C. P. Extracellular Vesicles: Composition, Biological Relevance, and Methods of Study. *BioScience* vol. 65 783–797 Preprint at https://doi.org/10.1093/biosci/biv084 (2015).
84. Welsh, J. A. *et al.* Minimal information for studies of extracellular vesicles (MISEV2023): From basic to advanced approaches. *J. Extracell. Vesicles* **13**, (2024).
85. Das, K. *et al.* Extracellular Vesicles in Triple–Negative Breast Cancer: Immune Regulation, Biomarkers, and Immunotherapeutic Potential. *Cancers* vol. 15 Preprint at https://doi.org/10.3390/cancers15194879 (2023).

86. Niture, S., Ghosh, S., Jaboin, J. & Seneviratne, D. Tumor Microenvironment Dynamics of Triple-Negative Breast Cancer Under Radiation Therapy. *International Journal of Molecular Sciences* vol. 26 Preprint at https://doi.org/10.3390/IJMS26062795 (2025).
87. Lee, Y. C. *et al.* Radioresistant triple-negative breast cancer cells release β-catenin containing extracellular vesicles to promote cancer stem cell activity of bystanders. *J. Cancer* **16**, 2890–2902 (2025).
88. Zhou, Z.-R. *et al.* Building radiation-resistant model in triple-negative breast cancer to screen radioresistance-related molecular markers. *Ann. Transl. Med.* **8**, 108–108 (2020).
89. To, N. H. *et al.* Radiation therapy for triple-negative breast cancer: emerging role of microRNAs as biomarkers and radiosensitivity modifiers. A systematic review. *Breast Cancer Research and Treatment* vol. 193 265–279 Preprint at https://doi.org/10.1007/s10549-022-06533-3 (2022).
90. Gray, M. *et al.* Development and characterisation of acquired radioresistant breast cancer cell lines. *Radiation Oncology* **14**, (2019).
91. Acloque, H., Adams, M. S., Fishwick, K., Bronner-Fraser, M. & Nieto, M. A. Epithelial-mesenchymal transitions: The importance of changing cell state in development and disease. *Journal of Clinical Investigation* vol. 119 1438–1449 Preprint at https://doi.org/10.1172/JCI38019 (2009).
92. Thiery, J. P., Acloque, H., Huang, R. Y. J. & Nieto, M. A. Epithelial-Mesenchymal Transitions in Development and Disease. *Cell* vol. 139 871–890 Preprint at https://doi.org/10.1016/j.cell.2009.11.007 (2009).
93. Leggett, S. E. *et al.* Morphological single cell profiling of the epithelial–mesenchymal transition. *Integrative Biology* **8**, 1133–1144 (2016).
94. Ravichandran, A. *et al.* 3d breast tumor models for radiobiology applications. *Cancers* vol. 13 Preprint at https://doi.org/10.3390/cancers13225714 (2021).
95. Liu, D. *et al.* Radiotherapy Resistance of 3D Bioprinted Glioma via ITGA2/p-AKT Signaling Pathway. *Adv. Healthc. Mater.* **13**, (2024).
96. Parra, M. R. *et al.* Comparative analysis of molecular targeted radiosensitizers in 2D and 3D cancer cell line models. *Acta Oncol. (Madr).* **64**, 1631–1639 (2025).
97. Wu, Y., Song, Y., Wang, R. & Wang, T. Molecular mechanisms of tumor resistance to radiotherapy. *Molecular Cancer* vol. 22 Preprint at https://doi.org/10.1186/s12943-023-01801-2 (2023).
98. Ouellette, M. M., Zhou, S. & Yan, Y. Cell Signaling Pathways That Promote Radioresistance of Cancer Cells. *Diagnostics* vol. 12 Preprint at https://doi.org/10.3390/diagnostics12030656 (2022).
99. Xu, J. *et al.* Application and progress of 3D tumor models in breast cancer. *Biotechnology and Bioengineering* vol. 122 30–43 Preprint at https://doi.org/10.1002/bit.28860 (2025).
100. Huerta-Reyes, M. & Aguilar-Rojas, A. Three-dimensional models to study breast cancer (Review). *International Journal of Oncology* vol. 58 331–343 Preprint at https://doi.org/10.3892/ijo.2021.5176 (2021).

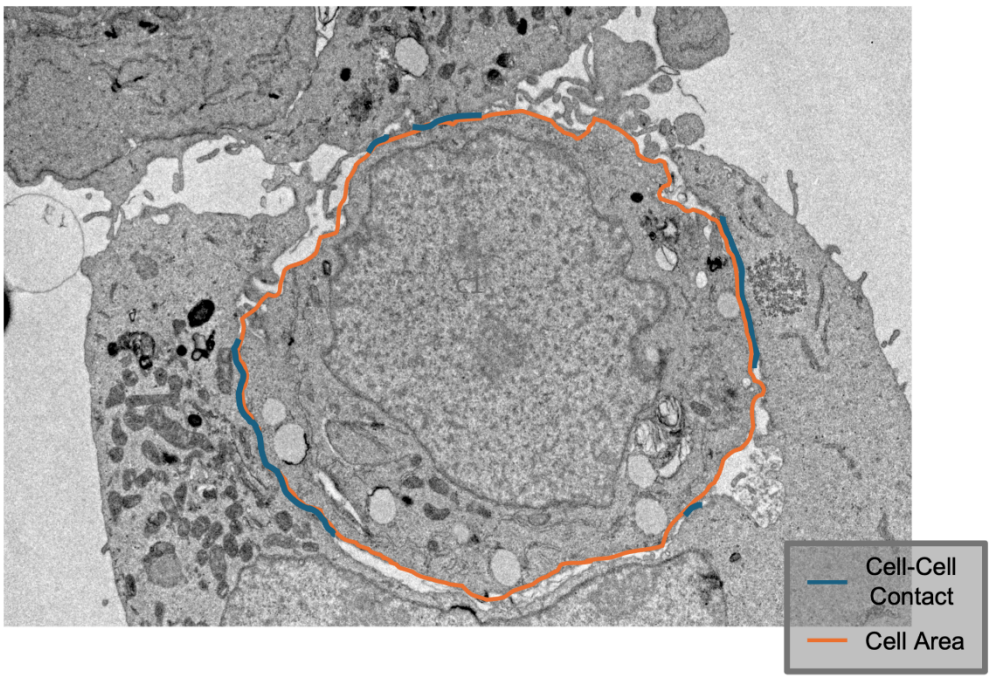
101. Gehre, S. *et al.* Clonogenicity-based radioresistance determines the expression of immune suppressive immune checkpoint molecules after hypofractionated irradiation of MDA-MB-231 triple-negative breast cancer cells. *Front. Oncol.* **13**, (2023).
102. Bian, L. *et al.* ATM expression is elevated in established radiation-resistant breast cancer cells and improves DNA repair efficiency. *Int. J. Biol. Sci.* **16**, 1096–1106 (2020).
103. Raitanen, J. *et al.* Comparison of Radiation Response between 2D and 3D Cell Culture Models of Different Human Cancer Cell Lines. *Cells* **12**, (2023).
104. Pires, I. M. *et al.* Targeting radiation-resistant hypoxic tumor cells through ATR inhibition. *Br. J. Cancer* **107**, 291–299 (2012).
105. Ratosa, I. *et al.* Ultra-hypofractionated one-week locoregional radiotherapy for patients with early breast cancer: Acute toxicity results. *Clin. Transl. Radiat. Oncol.* **46**, (2024).
106. Vanpouille-Box, C. *et al.* DNA exonuclease Trex1 regulates radiotherapy-induced tumor immunogenicity. *Nat. Commun.* **8**, 15618 (2017).
107. Deng, L. *et al.* STING-dependent cytosolic DNA sensing promotes radiation-induced type I interferon-dependent antitumor immunity in immunogenic tumors. *Immunity* **41**, 843–852 (2014).
108. Ko, Y. S. *et al.* Radioresistant breast cancer cells exhibit increased resistance to chemotherapy and enhanced invasive properties due to cancer stem cells. *Oncol. Rep.* **40**, 3752–3762 (2018).
109. *CURRENTS (N MODERN BIOLOGY Z (1968) 207.214. NORTH-HOLLAND PUBLISHING COMPANY, AMSTERDAM THE EFFECT OF GAMMA RADIATION ON CELL ENLARGEMENT AND SIZE DISTRIBUTION OF STRAIN L *.*
110. Liu, C., Nie, J., Wang, R. & Mao, W. The Cell Cycle G2/M Block Is an Indicator of Cellular Radiosensitivity. *Dose-Response* **17**, (2019).
111. Nickoloff, J. A. *et al.* Cellular Responses to Widespread DNA Replication Stress. *International Journal of Molecular Sciences* vol. 24 Preprint at https://doi.org/10.3390/ijms242316903 (2023).
112. Moussa, H., Mitchell, S. A., Gré Nman, R. & Joiner, M. C. *Cell-Cell Contact Increases Radioresistance in Head and Neck Carcinoma Cell Lines*. *int. j. radiat. biol* vol. 76 http://www.tandf.co.uk/journals (2000).
113. Janiszewska, M., Primi, M. C. & Izard, T. Cell adhesion in cancer: Beyond the migration of single cells. *Journal of Biological Chemistry* **295**, 2495–2505 (2020).
114. Frantz, C., Stewart, K. M. & Weaver, V. M. The extracellular matrix at a glance. *Journal of Cell Science* vol. 123 4195–4200 Preprint at https://doi.org/10.1242/jcs.023820 (2010).
115. Zhu, Y. *et al.* Emerging evidence for targeting mitochondrial metabolic dysfunction in cancer therapy. *Journal of Clinical Investigation* vol. 128 3682–3691 Preprint at https://doi.org/10.1172/JCI120844 (2018).
116. Pelicano, H. *et al.* Mitochondrial dysfunction in some triple-negative breast cancer cell lines: Role of mTOR pathway and therapeutic potential. *Breast Cancer Research* **16**, (2014).

117. Wei, Y. *et al.* Radiation resistance of cancer cells caused by mitochondrial dysfunction depends on SIRT3-mediated mitophagy. *FEBS Journal* **290**, 3629–3645 (2023).
118. Wang, L. *et al.* Dose-Dependent Effects of Radiation on Mitochondrial Morphology and Clonogenic Cell Survival in Human Microvascular Endothelial Cells. *Cells* **13**, (2024).
119. Kim, W. *et al.* Cellular stress responses in radiotherapy. *Cells* vol. 8 Preprint at https://doi.org/10.3390/cells8091105 (2019).
120. Lee, H. *et al.* Cell cycle arrest induces lipid droplet formation and confers ferroptosis resistance. *Nat. Commun.* **15**, (2024).
121. Okui, T. *et al.* CROT (Carnitine O-Octanoyltransferase) Is a Novel Contributing Factor in Vascular Calcification via Promoting Fatty Acid Metabolism and Mitochondrial Dysfunction. *Arterioscler. Thromb. Vasc. Biol.* **41**, 755–768 (2021).
122. Sanford, J. D., Franklin, D., Grois, G. A., Jin, A. & Zhang, Y. Carnitine o-octanoyltransferase is a p53 target that promotes oxidative metabolism and cell survival following nutrient starvation. *Journal of Biological Chemistry* **299**, (2023).
123. Lecordier, L. *et al.* Apolipoproteins L1 and L3 control mitochondrial membrane dynamics. *Cell Rep.* **42**, (2023).
124. Kim, K. W., Moretti, L., Mitchell, L. R., Jung, D. K. & Lu, B. Endoplasmic reticulum stress mediates radiation-induced autophagy by perk-eIF2α in caspase-3/7-deficient cells. *Oncogene* **29**, 3241–3251 (2010).
125. Li, J. F. *et al.* Persistent ER stress causes GPI anchor deficit to convert a GPI-anchored prion protein into pro-PrP via the ATF6–miR449c-5p–PIGV axis. *Journal of Biological Chemistry* **299**, (2023).
126. Cawley, K. *et al.* Disruption of microRNA biogenesis confers resistance to ER stress-induced cell death upstream of the mitochondrion. *PLoS One* **8**, (2013).
127. Hucl, T. & Gallmeier, E. DNA repair: Exploiting the fanconi anemia pathway as a potential therapeutic target. *Physiological Research* vol. 60 453–465 Preprint at https://doi.org/10.33549/physiolres.932115 (2011).
128. Saheki, Y. & De Camilli, P. Endoplasmic Reticulum-Plasma Membrane Contact Sites. **35**, 4 (2026).
129. Nascimbeni, A. C. *et al.* ER –plasma membrane contact sites contribute to autophagosome biogenesis by regulation of local PI 3P synthesis . *EMBO J.* **36**, 2018–2033 (2017).
130. Blondeel, E. *et al.* Sequential orthogonal assays for longitudinal and endpoint characterization of three-dimensional spheroids. *Nat. Protoc.* **20**, 2899–2941 (2025).
131. Pires, I. M. *et al.* Targeting radiation-resistant hypoxic tumor cells through ATR inhibition. *Br. J. Cancer* **107**, 291–299 (2012).
132. Jelonek, K., Widlak, P. & Pietrowska, M. The Influence of Ionizing Radiation on Exosome Composition, Secretion and Intercellular Communication. *Protein Pept. Lett.* 656–663 (2016) doi:10.2174/0929866523666160427105138.

133. Kadhim, M., Tuncay Cagatay, S. & Elbakrawy, E. M. Non-targeted effects of radiation: a personal perspective on the role of exosomes in an evolving paradigm. *International Journal of Radiation Biology* vol. 98 410–420 Preprint at https://doi.org/10.1080/09553002.2021.1980630 (2022).
134. Shami-Shah, A., Travis, B. G. & Walt, D. R. Advances in extracellular vesicle isolation methods: a path towards cell-type specific EV isolation. *Extracellular Vesicles and Circulating Nucleic Acids* vol. 4 447–460 Preprint at https://doi.org/10.20517/evcna.2023.14 (2023).
135. Ljungström, M. & Oltra, E. Methods for Extracellular Vesicle Isolation: Relevance for Encapsulated miRNAs in Disease Diagnosis and Treatment. *Genes* vol. 16 Preprint at https://doi.org/10.3390/genes16030330 (2025).
136. Mutschelknaus, L. *et al.* Exosomes derived from squamous head and neck cancer promote cell survival after ionizing radiation. *PLoS One* **11**, (2016).
137. Pszczółkowska, B. *et al.* Exosome secretion and cellular response of DU145 and PC3 after exposure to alpha radiation. *Radiat. Environ. Biophys.* **61**, 639–650 (2022).
138. Lee, Y. C. *et al.* Radioresistant triple-negative breast cancer cells release β-catenin containing extracellular vesicles to promote cancer stem cell activity of bystanders. *J. Cancer* **16**, 2890–2902 (2025).
139. Sato, Y. *et al.* Prediction of hub genes and key pathways associated with the radiation response of human hematopoietic stem/progenitor cells using integrated bioinformatics methods. *Sci. Rep.* **13**, (2023).
140. Liu, Y. *et al.* Research on radiotherapy related genes and prognostic target identification of rectal cancer based on multi-omics. *J. Transl. Med.* **21**, (2023).
141. Zhang, Y. *et al.* TOP2A correlates with poor prognosis and affects radioresistance of medulloblastoma. *Front. Oncol.* **12**, (2022).
142. Zalenski, A. *et al. Ii201 NEURO-ONCOLOGY • NOVEMBER 2020 STEM-22. TARGETING KIF11 TO RADIOSENSITIZE GLIOBLASTOMA STEM-23. INHIBITING PROTEIN PHOSPHATASE 2A INCREASES THE ANTITUMOR EFFECT OF PROTEIN ARGININE METHYLTRANSFERASE 5 INHIBITION IN MODELS OF GLIOBLASTOMA*.
143. Tallman, M. M. *et al.* Improving Localized Radiotherapy for Glioblastoma via Small Molecule Inhibition of KIF11. *Cancers (Basel).* **15**, (2023).

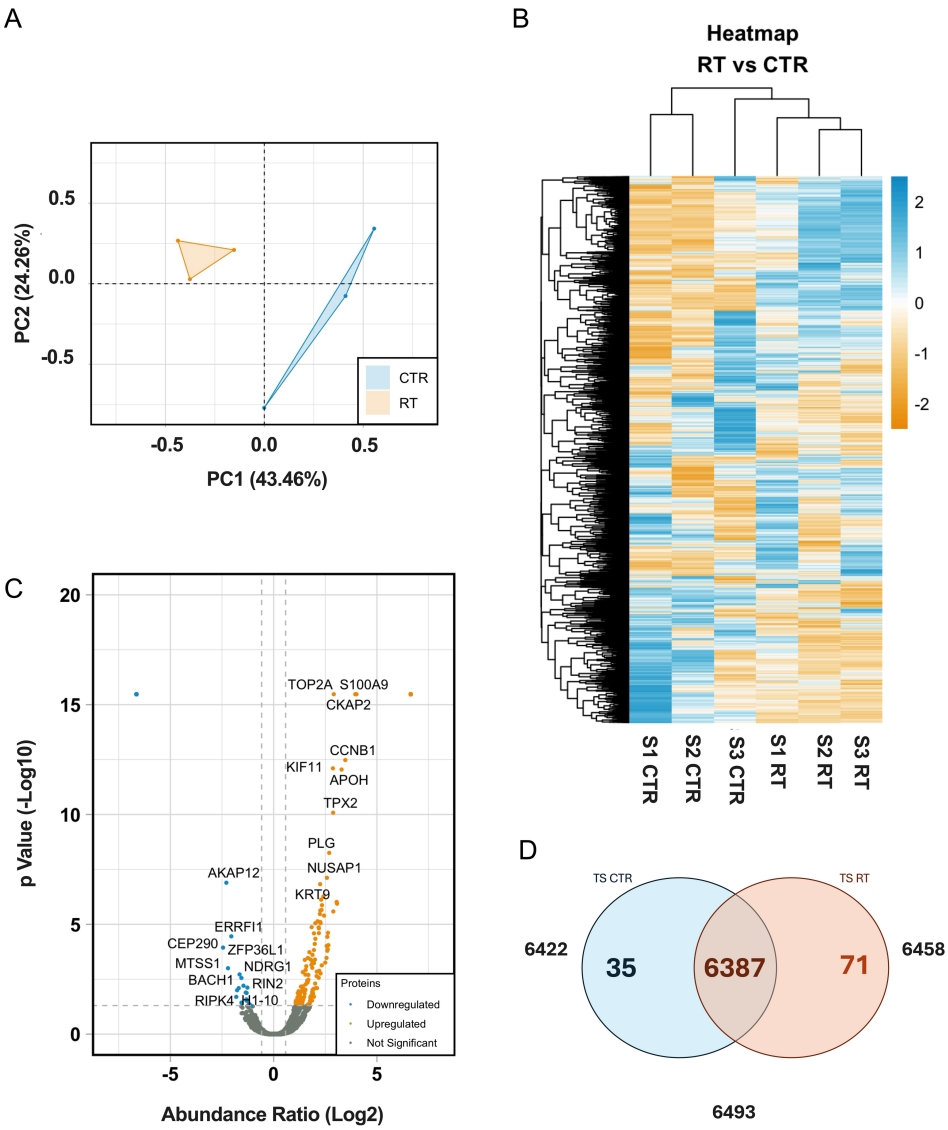
8. Supplementary Data

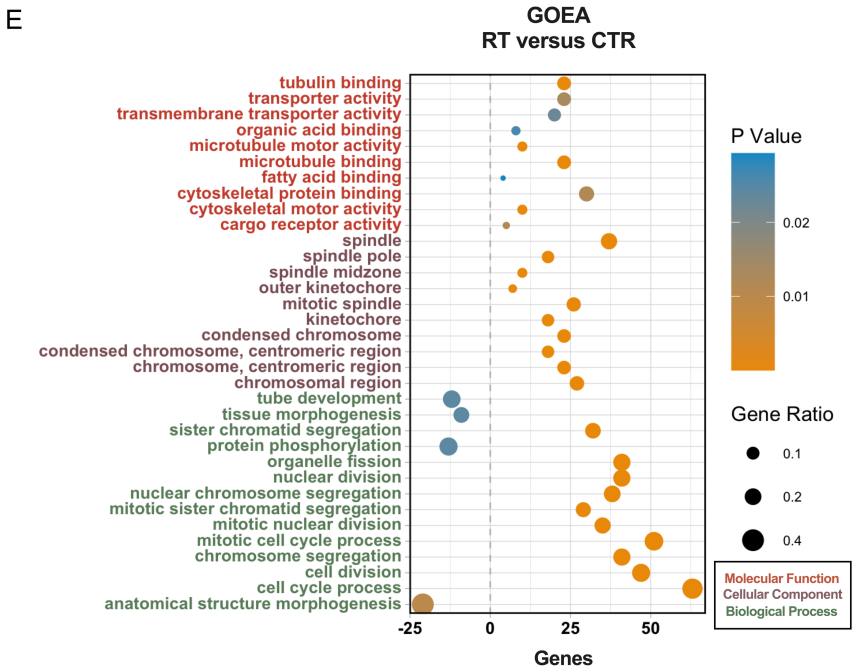
8.1 Figures



Supplementary Figure 1 – Tumor spheroid Cell area and Cell-cell contact delimitation

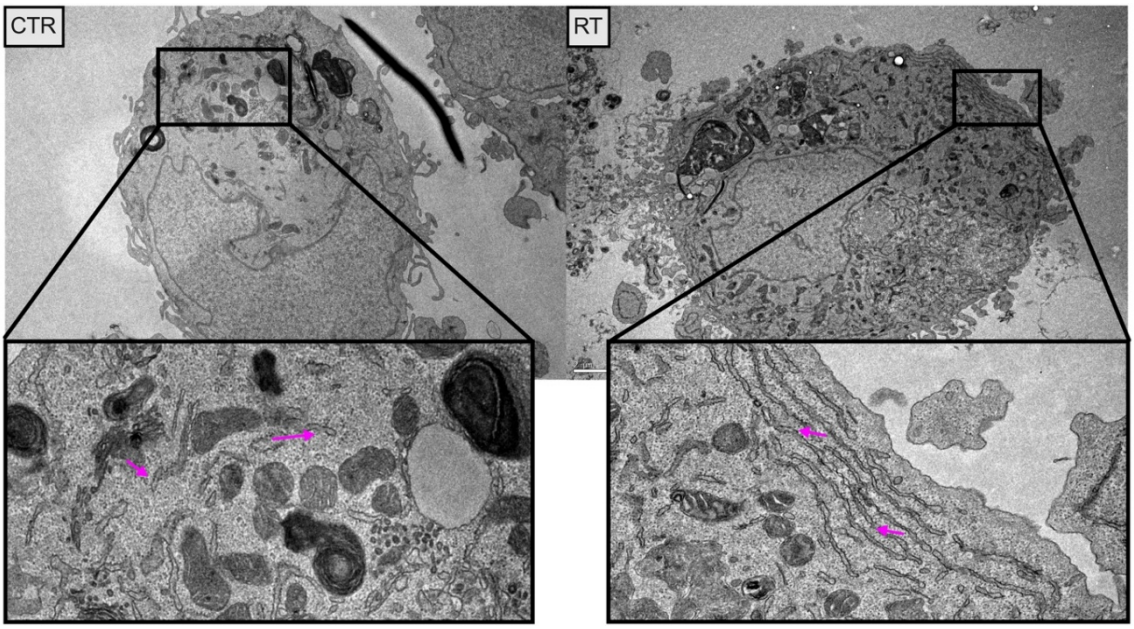
Tumor spheroids (TS) were exposed to 5 fractions of 5.2 Gy over 5 consecutive days (RT) or left without treatment (CTR) and analysed 24 hours after the last irradiation (IR). Alteration on cell area and cell-cell contact were analysed for TS CTR and TS RT.


A
PC2 (24.26%)
PC1 (43.46%)
CTR
RT
B
Heatmap
RT vs CTR
S1 CTR
S2 CTR
S3 CTR
S1 RT
S2 RT
S3 RT
C
p Value (-Log10)
Abundance Ratio (Log2)
TOP2A
S100A9
CKAP2
CCNB1
KIF11
APOH
TPX2
PLG
NUSAP1
AKAP12
KRT9
ERRFI1
CEP290
ZFP36L1
MTSS1
NDRG1
BACH1
RIN2
RIPK4
H1-10
Proteins
Downregulated
Upregulated
Not Significant
D
TS CTR
TS RT
6422
35
6387
71
6458
6493


E
GOEA
RT versus CTR
tubulin binding
transporter activity
transmembrane transporter activity
organic acid binding
microtubule motor activity
microtubule binding
fatty acid binding
cytoskeletal protein binding
cytoskeletal motor activity
cargo receptor activity
spindle
spindle pole
spindle midzone
outer kinetochore
mitotic spindle
kinetochore
condensed chromosome
condensed chromosome, centromeric region
chromosome, centromeric region
chromosomal region
tube development
tissue morphogenesis
sister chromatid segregation
protein phosphorylation
organelle fission
nuclear division
nuclear chromosome segregation
mitotic sister chromatid segregation
mitotic nuclear division
mitotic cell cycle process
chromosome segregation
cell division
cell cycle process
anatomical structure morphogenesis
Genes
P Value
Gene Ratio
Molecular Function
Cellular Component
Biological Process

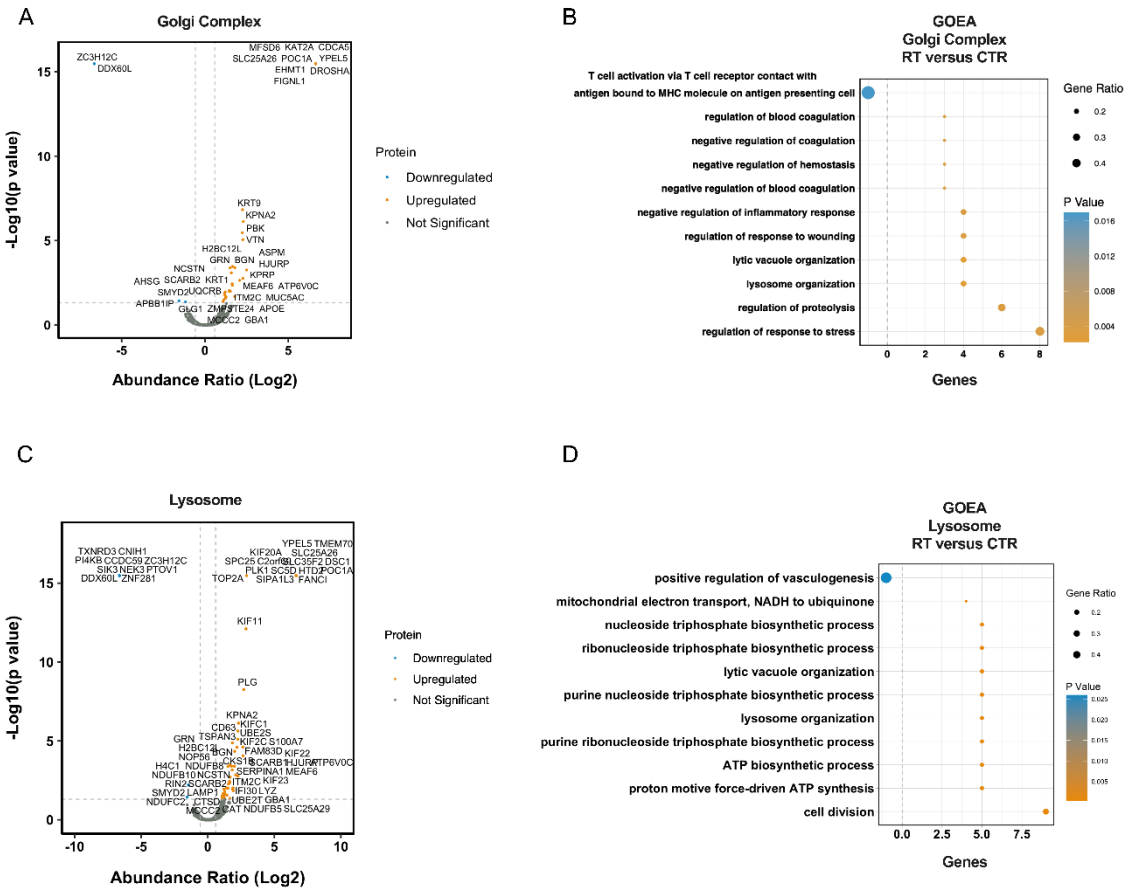
Supplementary Figure 2 - Hypofractionated radiotherapy alters the proteomic signature of MDA-MB-231 breast tumor spheroids.

Tumor spheroids (TS) were exposed to 5 fractions of 5.2 Gy over 5 consecutive days (RT) or left without treatment (CTR). Tumor cell lysates were prepared 72 h after the last irradiation (IR) and analysed through LC-MS/MS. (**A**) PCA analysis, (**B**) Volcano plot, (**C**) Heatmap after Z score normalization and (**D**) Illustrative Venn Diagram representation of all proteins identified in the proteomic analysis for CTR and RT conditions. (**E**) Gene ontology enrichment analysis (GEOA) for molecular functions, cellular components and biological processes of the upregulated and downregulated proteins for CTR and RT conditions.



Supplementary Figure 3 - Tumor spheroid cells' endoplasmic reticulum location changes after irradiation.

Tumor spheroids (TS) were exposed to 5 fractions of 5.2 Gy over 5 consecutive days (RT) or left without treatment (CTR), and analyzed 24 hours after the last irradiation (IR). Alteration on ER positioning is represented by pink arrows.



Supplementary Figure 4 - Proteomic analysis of radiotherapy on tumor spheroids' organelle content.

Tumor spheroids (TS) were exposed to 5 fractions of 5.2 Gy over 5 consecutive days (RT) or left without treatment (CTR). TS lysates were prepared 72 hours after last irradiation (IR). Lysosome assessment by (**A**) volcano plot and (**B**) GO analysis for biological processes of the upregulated and downregulated proteins for CTR and RT conditions. Golgi complex assessment by (**C**) volcano plot and (**D**) GO analysis for biological processes of upregulated and downregulated proteins, for CTR and RT conditions.

8.2 Tables

Supplementary Table 1 – Top 3 ontology terms for biological process, molecular functions and cellular components for differentially expressed proteins between 2D and 3D model.

The two models were accessed for differences by a proteomic analysis and further analysed by gene ontology enrichment analyses (GOEA) for different ontology terms using the cluster profiler in R software.

Proteins expression	Ontology	Pathway	Adjust *p* Value	Proteins
Upregulated	Biological Process	lipid metabolic process	7,74139 E-06	ABCA2, ABHD4, ACAD10, ACADS, ACADVL, ACSF2, ACSS1, AGPAT4, AKR1C3, ALDH3B1, ASAH1, ATG14, B3GALNT1, BCKDHB, BCKDK, BDH2, BLOC1S6, BTN2A1, CEPT1, CHKB, CLN3, CROT, CYP2S1, DGKH, DOLPP1, DPAGT1, ECHDC3, EHHADH, ERG28, FDX1, FGFR1, FUCA1, GBA2, GDE1, GDPD1, GGT5, GM2A, GPAT4, GPX4, GSTM2, H6PD, HACD1, HINT2, HSD17B8, HSD3B7, IL1B, ITPKC, LPGAT1, LPIN2, LRP5, MBOAT2, MBTPS1, MCEE, MGLL, MGST3, MIF, MLYCD, MTM1, NAGLU, NDUFAB1, NR1H2, OMA1, OSBPL1A, PAM, PC, PDSS1, PDSS2, PGS1, PHYH, PIAS4, PIGH, PIGN, PLA2G15, PLA2G6, PLCD1, PLCG2, PLCH1, PLD1, PNPLA4, PNPLA8, RAB38, SAMD8, SDR16C5, SEC14L2, SLC27A1, SLC44A1, SLC44A2, SMPD1, SMPD2, SPHK2, SREBF1, STARD3, STS, SUMF1, TBXAS1, TM7SF2, TMEM68, TNFRSF1A, TPP1, VLDLR
		lipid biosynthetic process	3,34435 E-05	ABCA2, ABHD4, ACADVL, ACSS1, AGPAT4, AKR1C3, ASAH1, ATG14, B3GALNT1, BCKDK, CEPT1, CHKB, CLN3, DGKH, DOLPP1, ERG28, FDX1, GBA2, GGT5, GPAT4, GPX4, GSTM2, H6PD, HACD1, HINT2, HSD17B8, HSD3B7, IL1B, ITPKC, LPGAT1, LPIN2, MBOAT2, MBTPS1, MGLL, MIF, MLYCD, MTM1, NDUFAB1, NR1H2, OSBPL1A, PAM, PDSS1, PDSS2, PGS1, PIGH, PIGN, PLA2G15, PLA2G6, PLCG2, PLD1, PNPLA8, RAB38, SAMD8, SEC14L2, SLC27A1, SLC44A1, SLC44A2, SMPD1, SMPD2, SPHK2, SREBF1, STARD3, TBXAS1, TM7SF2, TMEM68
		cellular lipid metabolic process	3,88991 E-05	ABCA2, ABHD4, ACAD10, ACADS, ACADVL, ACSF2, ACSS1, AGPAT4, AKR1C3, ALDH3B1, ASAH1, ATG14, B3GALNT1, BCKDK, BDH2, BLOC1S6, CEPT1, CHKB, CLN3, CROT, CYP2S1, DGKH, DOLPP1, DPAGT1, ECHDC3, EHHADH, FUCA1, GBA2, GDE1, GDPD1, GGT5, GM2A, GPAT4, GPX4, GSTM2, HACD1, HSD17B8, IL1B, ITPKC, LPGAT1, LPIN2, MBOAT2, MCEE, MGLL, MGST3, MIF, MLYCD, MTM1, NAGLU, NDUFAB1, NR1H2, PDSS1, PDSS2, PGS1, PHYH, PIGH, PIGN, PLA2G15, PLA2G6, PLCD1, PLCG2, PLCH1, PLD1, PNPLA4, PNPLA8, RAB38, SAMD8, SDR16C5, SLC27A1, SLC44A1, SLC44A2, SMPD1, SMPD2, SPHK2, SREBF1, SUMF1, TBXAS1, TMEM68, TNFRSF1A

	Molecular Function	**phospholipase activity**	3,61668E-06	ABHD4, GDE1, GDPD1, MGLL, PLA2G15, PLA2G6, PLCD1, PLCG2, PLCH1, PLD1, PNPLA4, PNPLA8, SMPD1, SMPD2
		transmembrane signaling receptor activity	6,99366E-06	EPHB3, FGFR1, FZD7, FZD8, GPR39, ICAM1, IL6ST, ITGA2, L1CAM, LGR4, LRP5, LRP6, LTBP1, NOTCH1, PTPRE, PTPRM, ROR1, SPHK2, TGFBR1, TLR3, TNFRSF10D, TNFRSF1A, VLDLR
		phosphoric diester hydrolase activity	2,17259E-05	GDE1, GDPD1, PDE10A, PDE2A, PDE7A, PLCD1, PLCG2, PLCH1, PLD1, SMPD1, SMPD2
	Cellular Components	**cell periphery**	0,0486203	ABCA2, ABCB8, ABHD17C, ABTB1, ADAMTS1, ALDH3B1, AMOTL1, ARID1B, ASAP2, ATP11A, ATRN, ATXN3, B2M, BBS2, BLTP1, BORCS5, BTBD8, BTN2A1, BTN3A3, CBLB, CD276, CD58, CD68, CDH11, CDK16, CLIC6, CLN3, CNST, COL13A1, COL4A2, COL6A1, CRELD1, CRIP2, CYTH4, DENND1A, DGKH, DOCK2, DRAM2, EDIL3, EHD3, ENO2, ENPP4, EPB41, EPB41L5, EPHB3, ESYT2, FAM171A1, FCGRT, FCHSD1, FGFR1, FMN1, FN1, FURIN, FZD7, FZD8, GAA, GBA2, GCA, GDE1, GGT5, GM2A, GNA15, GPR39, GSN, HFE, HLA-B, HSD17B8, ICAM1, IFITM3, IGSF8, IL6ST, IRAK4, ITGA10, ITGA2, ITPR3, KRT19, L1CAM, LAMA4, LAMB2, LAMTOR2, LGR4, LLGL2, LRIG1, LRP5, LRP6, LTBP1, LTBR, LZTS2, MAGT1, MAP3K5, MDK, MELTF, MFSD6, MGLL, MGRN1, MICAL1, MICALL2, MIF, MMP1, MTM1, MTSS1, MUC5B, MYO1F, NDFIP1, NDRG1, NFX1, NOTCH1, NTN4, NUBPL, OAS3, OSBPL1A, PARD3B, PDE2A, PDGFC, PGM5, PIEZO1, PIGN, PKD2, PKP3, PLA2G6, PLCD1, PLCG2, PLCH1, PLD1, PPIP5K1, PPL, PROS1, PSD3, PTPN13, PTPRE, PTPRM, RAB31, RAB37, RAB38, RAB3A, RAB4B, RASA1, RASSF3, REPS2, RGS14, RHBDF2, RHOB, RHOF, RILPL1, RND3, RNF10, RNF5, RNH1, ROR1, RTN2, S100A4, SAMD8, SDR16C5, SEMA3A, SEMA4C, SEPTIN6, SERPINB1, SERPINE2, SEZ6L2, SHC3, SIDT2, SIGIRR, SLC12A6, SLC12A9, SLC17A5, SLC22A5, SLC27A1, SLC39A3, SLC44A1, SLC44A2, SLC4A7, SLC67A1, SLC9A7, SLITRK6, SMPD1, SMPD2, SOS1, SPG11, SPRED2, SPRY1, SPTB, STC1, STK16, STS, STX2, STXBP2, STXBP5, SYTL2, SYTL4, TACSTD2, TCAF2, TEC ,TGFBR1, TIMP3, TJAP1, TLR3, TM7SF2, TM7SF3, TMEM120A, TMEM132A, TMEM161B, TMEM231, TNC, TNFRSF10D, TNFRSF1A, TNIK, TOM1, TRIM4, TSC22D1, UBQLN2, UNC13B, VLDLR, WDR19, ZDHHC20

		endomembrane system	0,0486203	ABCA2, ABHD17C, ABHD4, ACTR1B, AGAP1, AGPAT4, AGR2, ALDH3B1, ALDOC, ALG10, ALG11, ALG12, AP5B1, AP5M1, ARSK, ASAH1, ASAP2, ATAT1, ATG14, ATL1, ATP11A, ATP13A2, ATRN, ATXN3, B2M, B3GALNT1, B4GALT7, B4GAT1, BLOC1S6, BLTP1, BNIP3, BNIP3L, BOK, BORCS5, BTBD8 C6orf120, C9orf72, CAMLG, CCDC91, CCND1, CD58, CD68, CDK16, CDK5RAP2, CEPT1, CHEK2, CHPF, CHST14, CLEC16A, CLN3, CNPY2, CNST, COL13A1, COL4A2, COL6A1, COLGALT2, COQ6, CREG1, CYB5A, CYBC1, CYP2S1, CYTH4, DENND6A, DGKH, DOCK2, DOLPP1, DPAGT1, DPY19L3, DRAM2, DYM, EHD3, EMC4, EMC6, ENPP4, ENTPD5, ERG28, ESYT2, FAM20B, FCGRT, FCHSD1, FGD1, FMN1, FN1, FUCA1, FURIN, FZD7, FZD8, GAA, GALNS, GALNT12, GBA2, GBP2, GCA, GCC1, GDPD1, GKAP1, GM2A, GPAT4, GPX4, GSN, GSTM2, H6PD, HACD1, HFE, HLA-B, HSD3B7, IFITM3, IFT57, IL1B, IRAK4, ITPR3, JMY, LAMB2, LAMTOR2, LPGAT1, LPIN2, LRP5, LRP6, LTBP1, LTBR, MAGT1, MANEA, MAP3K5, MBOAT2, MBTPS1, MCFD2, MELTF, MGLL, MGRN1, MGST3, MICAL1, MICALL2, MIF, MIF4GD, MTM1, MUC5B, MVP, NBR1, NDFIP1, NDRG1, NHLRC3, NOTCH1, NUP42, OAS1, OSBPL1A, PACS2, PAM, PARD3B, PDE2A, PDGFC, PGS1, PHAF1, PIEZO1, PIGH, PIGN, PKD2, PLAT, PLD1, PLEKHA8, PNPLA8, POLR2M, POMGNT1, PRAF2, PRICKLE2, PROS1, PTGFRN, PYGB, RAB20, RAB31, RAB37, RAB38, RAB3A, RAB4B, RABL2A, RB1CC1, RCSD1, REEP6, RHBDF1, RHBDF2, RHOB, RHOF, RND3, RNF13, RNF175, RNF5, RTN2, SAMD8, SBF2, SCAPER, SDR16C5, SELENOF, SELENOT, SEMA4C, SEPTIN6, SERPINB1, SERPINE2, SEZ6L2, SHISA2, SIK2, SLC17A5, SLC22A5, SLC27A1, SLC35D1, SLC37A2, SLC38A10, SLC44A2, SLC67A1, SLC9A7, SMPD1, SMPD2, SNX21, SPG11, SPHK2, SPRED2, SPRY1, SREBF1, SSH2, STARD3, STK11IP, STK16, STS, STX2, STXBP2, STXBP5, SUMF1, SUN1, SYTL2, SYTL4, TBC1D1, TBC1D14, TBCK, TBXAS1, TGFBR1, TIMP3, TJAP1, TLR3, TM7SF2, TMEM120A, TMEM132A, TMEM168, TMEM208, TMEM39B, TMEM68, TMTC2, TNC, TNFRSF1A, TNIK, TOM1, TOR1AIP2, TPP1, TPRG1L, TRIM5, UBE2G2, UBQLN4, UNC13B, USP25, VLDLR, VPS13C, VPS37A, VPS8, YIPF5, ZDHHC13, ZDHHC20
		vacuole	0,0486203	ABCA2, AP5B1, AP5M1, ARSK, ASAH1, ATG12, ATG14, ATP11A, ATP13A2, ATXN3, B2M, BORCS5, BORCS6, C6orf120, C9orf72, CD68, CLN3, COL6A1, CREG1, CTBS, DEPDC5, DRAM2, FUCA1, GAA, GALNS, GCA, GDAP2, GM2A, GPR155, IDUA, IFITM3, IL1B, JMY, LAMTOR2, MAGT1, NAGLU, NBR1, NHLRC3, OSTM1, PLA2G15,

				PLD1, PYGB, RAB37, RAB38, RAB3A, RB1CC1, RNF13, SBF2, SERPINB1, SIDT2, SLC17A5, SLC44A2, SMPD1, SPG11, SPHK2, STARD3, STK11IP, STS, STXBP2, TBC1D14, TLR3, TMEM208, TOM1, TPP1, UBQLN2, UBQLN4, VLDLR, VPS13C, WDR24, WDR59
Downregulated	**Biological Process**	**nuclear division**	0,00224 1469	APC, ASPM, BRCA2, BRIP1, BUB1B, CAV2, CCDC8, CCNB1, CDC20, CDCA2, CDCA5, CDCA8, CDK1, CENPE, CEP192, CEP85, CKS2, FANCD2, FIGNL1, HASPIN, HSPA2, INCENP, KIF11, KIF18B, KIF23, KIF2C, KNSTRN, MAD2L1, MASTL, MISP, MKI67, NUF2, PINX1, PKMYT1, PLK1, PPP1R9B, PRC1, PSMC3IP, PSRC1, PTTG1, RAD51, SKA1, SKA2, SKA3, TPX2, UBE2S, WNT5A, XRCC3, ZWILCH, ZWINT
		regulation of cell cycle	0,00224 1469	ALMS1, APC, ARID2, ASNS, ASPM, ATF2, AVEN, BRCA2, BRD7, BRIP1, BUB1B, CAV2, CCDC8, CCNB1, CCNY, CCP110, CCPG1, CDC20, CDCA2, CDCA5, CDCA8, CDK1, CDK5RAP1, CENPE, CEP76, CEP85, CKS1B, CKS2, CLSPN, DONSON, DPF3, ECT2, EP400, EPC2, ERCC6, FANCD2, FEM1B, FIGNL1, FOXN3, GMNN, HASPIN, HMGA2, HSPA2, HUS1, INCENP, INO80C, JUN, KAT7, KIF11, KIF20A, KIF23, KIF2C, KNSTRN, MAD2L1, MASTL, MEAF6, MEN1, MKI67, NF2, NUF2, ORC1, PABIR1, PCLAF, PINX1, PKMYT1, PLK1, PPP1R9B, PRC1, PRR11, PSRC1, RAD51, RARA, RFWD3, RRM1, RRM2, RRP8, SASS6, SETD2, SKA1, SKA3, TOPBP1, TPX2, TSC22D2, UBE2E2, UVRAG, WDR62, WNT5A, XRCC3, ZFP36L2, ZWILCH, ZWINT
		organelle fission	0,00464 2106	APC, ASPM, BRCA2, BRIP1, BUB1B, CAV2, CCDC8, CCNB1, CDC20, CDCA2, CDCA5, CDCA8, CDK1, CENPE, CEP192, CEP85, CKS2, FANCD2, FIGNL1, FIS1, HASPIN, HSPA2, INCENP, KIF11, KIF18B, KIF23, KIF2C, KNSTRN, MAD2L1, MAPT, MASTL, MIEF1, MISP, MKI67, NUF2, PINX1, PKMYT1, PLK1, PPP1R9B, PRC1, PSMC3IP, PSRC1, PTTG1, RAD51, SKA1, SKA2, SKA3, TPX2, UBE2S, WNT5A, XRCC3, ZWILCH, ZWINT
	Cellular Components	**chromosome**	0,00010 029	AEBP2, APC, ARID2, ARID4A, ATF2, ATF6, BRCA2, BRD7, BRIP1, BRPF1, BUB1B, CCNB1, CDC20, CDCA2, CDCA5, CDCA8, CDK1, CDK2AP1, CENPE, CENPP, CENPQ, CHAF1B, DNMT3A, DONSON, DPF3, DVL3, ENC1, EP400, EPC2, ERCC6, ETV3, FANCD2, FANCI, FIGNL1, FOXN3, GINS1, GMEB1, H1-2, H2AC21, HASPIN, HELLS, HMGA2, HMGXB4, HNRNPA2B1, HSF2, HSPA2, HUS1, INCENP, ING1, INO80C, JUN, KANSL1, KAT6A, KAT7, KDM1B, KIF2C, KNSTRN, MAD2L1, MBD1, MBD2, MCM10, MCM3AP, MCM8, MEAF6, MEN1, MIS18A, MKI67, MMS22L, NLRP2, NSMCE1, NSMCE3, NSMCE4A, NUF2, OIP5, ORC1, ORC6, PBX2, PINX1, PLK1, POLE2, POLE4, PPHLN1, PRC1, PRDM10, PRIM1, PSEN1, PSMC3IP, RAD51, RARA, RFWD3, RNF138, RNF169, RRP8, SAP30, SETD1A, SETD2, SKA1, SKA2, SKA3, SMAD3, SRCAP,

				TAF5, TGM2, THOC5, TOPBP1, TWNK, UBAP2, USF1, UVRAG, XRCC3, ZWILCH, ZWINT
		condensed chromosome	0,00020 4437	APC, ARID2, BRCA2, BRD7, BUB1B, CCNB1, CDC20, CENPE, CENPP, CENPQ, FANCD2, HSPA2, HUS1, INCENP, KANSL1, KIF2C, KNSTRN, MAD2L1, MEAF6, MKI67, NSMCE1, NSMCE3, NSMCE4A, NUF2, PINX1, PLK1, PSEN1, PSMC3IP, RAD51, SKA1, SKA2, SKA3, TOPBP1, ZWILCH, ZWINT
		chromosome, centromeric region	0,00039 155	APC, ARID2, BRD7, BUB1B, CCNB1, CDC20, CDCA5, CDCA8, CENPE, CENPP, CENPQ, DNMT3A, HELLS, INCENP, KANSL1, KAT7, KIF2C, KNSTRN, MAD2L1, MEAF6, MIS18A, NSMCE1, NUF2, OIP5, PINX1, PLK1, PSEN1, SKA1, SKA2, SKA3, UVRAG, ZWILCH, ZWINT

Supplementary Table 2 – Exclusive proteins identified for control or irradiated spheroids exposed to 5 fractions of 5.2 Gy (RT).

TS were analysed 72 hours after last irradiation (IR) through proteomic analysis.

Tumor Spheroids Conditions	Exclusive Proteins
CTR	DDX60L, ZC3H7B, NAB1, PDE4DIP, RALGPS2, CCDC59, SYAP1, TXNRD3, KIDINS220, ZKSCAN8, SIK3, ADARB1, PEAK1, NEK4, EPB41L5, ZNF281, JMY, PTOV1, CNIH1, PI4KB, N4BP2, SCAPER, ZC3H12C, MICU3, INPP4B, TIFA, NEK3, NRP2, ZNF608, LZTS2, NUAK1, DKK1, C9orf72, WDR4, MMP9
RT	KRT6B, CAMK2B, KIF20A, POMGNT1 , PLK1, PBRM1, SLC4A2, NRDE2, SIPA1L3, NUF2, EP400, CSPG4, CROT, CDCA3, SHCBP1, KNSTRN, EMSY, MFSD6, GPC1, TMEM70, SLC1A4, FANCI, GALNT5, CDCA8, S100A8, ESPL1, CDCA5, BARD1, DSC1, HELLS, EHMT1, TECPR2, KIF18B, KAT2A, SPC25, PRR11, THOC7, SHISA2, ARHGAP31, TF, FIGNL1, SC5D, TIMM17A, CHAF1B, YPEL5, DROSHA, MICALL2, HVCN1, BRIP1, POC1A, HDAC10, ADGRG1, USP20, FANCD2, FAM3A, B3GNT2, C2orf69, SLC35F2, SLC25A26, SGO2, KLHDC2, HTD2, CYP4V2, APOL3, NCBP2AS2, KCTD6, LDLRAP1, CD99L2, DCTPP1, SLC25A35, FBXO42

Supplementary Table 3 – Top 3 ontology terms for biological processes, molecular functions and cellular components for differentially expressed proteins after Irradiation.

TS were analysed 72 hours after last irradiation (IR) by a proteomic and further gene ontology enrichment analyses (GOEA), using the cluster profiler in R software.

Proteins	Ontology	Pathway	Adjust p Value	Proteins
	Biological Process	nuclear division	9,51685 E-19	ANLN, ASPM, AURKA, AURKB, BRIP1, BUB1B, CCNB1, CCNB2, CDCA5, CDCA8, CDK1, CENPE, CENPF, DLGAP5, ESPL1, FANCD2, FIGNL1, KIF11, KIF18B, KIF20B, KIF22, KIF23, KIF2C, KIF4A, KIFC1, KNSTRN, MKI67, NUF2, NUSAP1, PLK1, PPP1R9B, PRC1, RACGAP1,

Upregulated				SKA3, SPC25, TOP2A, TPX2, TTK, UBE2C, UBE2S, UHRF1
		nuclear chromosome segregation	2,31164 E-18	ASPM, AURKA, AURKB, BRIP1, BUB1B, CCNB1, CCNB2, CDC6, CDCA5, CDCA8, CDK1, CENPE, CENPF, DLGAP5, ESPL1, FAM83D, FANCD2, KIF11, KIF18B, KIF22, KIF23, KIF2C, KIF4A, KIFC1, KNSTRN, NUF2, NUSAP1, PBRM1, PLK1, PRC1, RACGAP1, SKA3, SPC25, TOP2A, TPX2, TTK, UBE2C, UHRF1
		organelle fission	5,31279 E-17	ANLN, ASPM, AURKA, AURKB, BRIP1, BUB1B, CCNB1, CCNB2, CDCA5, CDCA8, CDK1, CENPE, CENPF, DLGAP5, ESPL1, FANCD2, FIGNL1, KIF11, KIF18B, KIF20B, KIF22, KIF23, KIF2C, KIF4A, KIFC1, KNSTRN, MKI67, NUF2, NUSAP1, PLK1, PPP1R9B, PRC1, RACGAP1, SKA3, SPC25, TOP2A, TPX2, TTK, UBE2C, UBE2S, UHRF1
	Molecular Function	microtubule binding	5,11E -09	CENPE, CENPF, DLGAP5, FAM83D, GTSE1, KIF11, KIF18B, KIF20A, KIF20B, KIF22, KIF23, KIF2C, KIF4A, KIFC1, KNSTRN, NUF2, NUSAP1, PLK1, PRC1, RACGAP1, S100A8, S100A9, SKA3
		microtubule motor activity	7,69E-07	CENPE, KIF11, KIF18B, KIF20A, KIF20B, KIF22, KIF23, KIF2C, KIF4A, KIFC1
		tubulin binding	7,69E-07	CENPE, CENPF, DLGAP5, FAM83D, GTSE1, KIF11, KIF18B, KIF20A, KIF20B, KIF22, KIF23, KIF2C, KIF4A, KIFC1, KNSTRN, NUF2, NUSAP1, PLK1, PRC1, RACGAP1, S100A8, S100A9, SKA3
	Cellular Components	mitotic spindle	1,53E-13	ASPM, AURKA, AURKB, CDC6, CDK1, CENPE, CKAP2, CKAP2L, DLGAP5, ESPL1, FAM83D, KAT2A, KIF11, KIF18B, KIF20B, KIF22, KIF23, KIFC1, KNSTRN, NUSAP1, PLK1, PRC1, RACGAP1, SKA3, TPX2, YPEL5
		spindle	1,53E -13	ASPM, AURKA, AURKB, BUB1B, CCNB1, CDC6, CDCA8, CDK1, CENPE, CENPF, CKAP2, CKAP2L, DLGAP5, ESPL1, FAM83D, KAT2A, KIF11, KIF18B, KIF20A, KIF20B, KIF22, KIF23, KIF2C, KIF4A, KIFC1, KNSTRN, NUSAP1, PLK1, POC1A, PRC1, RACGAP1, SHCBP1, SKA3, TPX2, TTK, UHRF1, YPEL5

		chromosome, centromeric region	6,08E-08	AURKA, AURKB, BUB1B, CCNB1, CDCA5, CDCA8, CENPE, CENPF, HELLS, HJURP, KIF22, KIF2C, KNSTRN, MACROH2A1, MEAF6, NUF2, PBRM1, PLK1, SGO2, SKA3, SPC25, TOP2A, TTK
Downregulated	**Biological Process**	anatomical structure morphogenesis	0,009783	ADARB1, C9orf72, CA9, CCN1, CEP290, DKK1, EPB41L5, ERRFI1, KIDINS220, LZTS2, MMP9, MTSS1, NAB1, NEK3, NRP2, RASA1, RIN2, SASH1, ZFP36L1, ZNF22, ZNF281
		tissue morphogenesis	0,024278	ADARB1, CA9, CCN1, CEP290, DKK1, EPB41L5, LZTS2, MTSS1, NRP2
		protein phosphorylation	0,024278	ADARB1, C9orf72, CCN1, DKK1, ERRFI1, MMP9, NEK3, NEK4, NUAK1, PEAK1, SASH1, SIK3, SYAP1

Supplementary Table 4 – Exclusive proteins related with different organelles identified in control or irradiated spheroids, exposed to 5 fractions of 5.2 Gy.

TS were analysed 72 hours after last irradiation (IR) by a proteomic analysis and further gene ontology enrichment analyses (GOEA) using the cluster profiler in R software. The proteins were after extracted and further explored for each organelle identified.

Organelle	**Exclusive Proteins**	
	Condition	**Proteins**
Mitochondria	**CTR**	DDX60L, NAB1, CCDC59, KIDINS220, SIK3, PEAK1, ZNF281, JMY, PTOV1, N4BP2, SCAPER, INPP4B, ZNF608, LZTS2, NUAK1, DKK1, C9orf72, MMP9
	RT	TMEM70, SLC1A4, SHISA2, ARHGAP31, HVCN1, KLHDC2, HTD2, SPC25, KRT6B, CD99L2, FAM3A, SLC4A2, YPEL5, SHCBP1, CDCA8, NUF2, GALNT5, PLK1, SLC25A26, EP400, CDCA3, FANCI, DROSHA, FANCD2, SLC25A35, FBXO42, C2orf69, NRDE2
Endoplasmic Reticulum	**CTR**	DDX60L, NAB1, TXNRD3, SIK3, PEAK1, MICU3, INPP4B, LZTS2
	RT	MFSD6, GPC1, SHISA2, ARHGAP31, KAT2A, PRR11, HTD2, SPC25, KRT6B, EHMT1, SLC25A26, KIF18B, FANCI, DROSHA, SLC25A35, NRDE2
Golgi Complex	**CTR**	DDX60L, ZC3H12C
	RT	MFSD6, KAT2A, CDCA5, EHMT1, YPEL5, SLC25A26, POC1A, DROSHA, zxFIGNL1
Lysosome	**CTR**	

		DDX60L, CCDC59, TXNRD3, SIK3, ZNF281, PTOV1, CNIH1, PI4KB, ZC3H12C, NEK3
	RT	TMEM70, DSC1, HTD2, SPC25, YPEL5, KIF20A, PLK1, SLC25A26, SLC35F2, FANCI, POC1A, SIPA1L3, SC5D, C2orf69

Supplementary Table 5 - Top 3 ontology terms for biological process for differentially expressed proteins organelle identified in control or irradiated spheroids, exposed to 5 fractions of 5.2 Gy.

TS were analysed 72 hours after last irradiation (IR) by a proteomic analysis and further analysed by gene ontology enrichment analyses (GOEA) for cellular component terms, using the cluster profiler in R software. Proteins were after extracted and further explored for each organelle identified by GOEA for biological pathways.

Organelle	**Biological Pathways**			
	Proteins Expression	**Terms**	**Adjust p value**	**Proteins**
Mitochondria	**Upregulated**	oxidative phosphorylation	9,14033E-10	ATP5F1E, CCNB1 CDK1, NDUFB10, NDUFB5, NDUFB8, NDUFC2, UQCRB
		ATP synthesis coupled electron transport	1,89288E-09	CCNB1, CDK1, NDUFB10, NDUFB5, NDUFB8, NDUFC2, UQCRB
		mitochondrial ATP synthesis coupled electron transport		
	Downregulated	positive regulation of cell-substrate adhesion	4,36955E-05	CCN1, RIN2
Endoplasmic Reticulum	**Upregulated**	skin development	0,008062809	GBA1, KRT1, KRT14, KRT9, S100A7, ZMPSTE24
		lysosome organization	0,008062809	GBA1, GRN, LAMP1, SCARB2
		lytic vacuole organization	0,008062809	GBA1, GRN, LAMP1, SCARB2
	Downregulated	positive regulation of protein kinase activity	0,036123822	CCN1, SASH1
		positive regulation of kinase activity		
		positive regulation of transferase activity		
Golgi Complex	**Upregulated**	lysosome organization	0,00221547	ATP6V0C, GBA1, GRN, SCARB2
		lytic vacuole organization	0,00221547	ATP6V0C, GBA1, GRN, SCARB2
		negative regulation of blood coagulation	0,003414846	APOE, KRT1, VTN
	Downregulated	T cell activation via T cell receptor contact with antigen bound to MHC molecule on antigen presenting cell	0,016959865	APBB1IP

Lysosome	**Upregulated**	proton motive force-driven ATP synthesis	0,000340272	ATP6V0C, NDUFB10, NDUFB5, NDUFB8, NDUFC2
		ATP biosynthetic process	0,000340272	ATP6V0C, NDUFB10, NDUFB5, NDUFB8, NDUFC2
		purine ribonucleoside triphosphate biosynthetic process	0,000340272	ATP6V0C, NDUFB10, NDUFB5, NDUFB8, NDUFC2
	Downregulated	positive regulation of vasculogenesis	0,025966502	RIN2

Supplementary Table 6 – Exclusive proteins related with EVs identified in control (CTR) or irradiated spheroids (RT), exposed to 5 fractions of 5.2 Gy (RT).

Conditioned media (CM) from TS was collected 72 hours after last irradiation (IR) and extracellular vesicles (EVs) were isolated. Exclusive proteins were after detected by a proteomic analysis using the cluster profiler in R software.

Isolated EVs Condition	Exclusive Proteins
CTR	COL13A1, DCBLD2, DKK1, FLOT1, GPN1, GSDMA, HNRNPDL, MANBA, MSRA, OSMR, PDGFRB, PLS1, PTN, SERPINB7, SLIT2, SPIN4, ST3GAL1, TUBAL3
RT	ACOT13, AP2A2, ATL3, ATP5F1E, C1QBP, CARS1, CAVIN2, CCL14, CKAP4, CKAP5, CUL2, DENR, DIAPH1, DIS3, DUT, EFTUD2, ELAC2, EWSR1, FN3KRP, GLO1, GOLPH3, GSPT1, GSTK1, H3C1, H3C13, HACD3, HDAC2, HIBADH, IARS2, IDH2, KIF11, LXN, MIF, MSH2, MTA2, MYDGF, NAA10, NHERF1, NHERF2, OGDH, POLE3, PPME1, PSMD9, RAP1GDS1, SEC24C, SLC7A6, SRP9, STRN, SWAP70, TBCE, TOMM70, TOP2A, TRMT6, TTC38, UBE2V1, UBLCP1, UBXN1, UFL1